Chair of Reservoir Engineering

Master's Thesis

Quantifying the Upscaling Footprint from Pore to Darcy Scale via Pore Network Modelling: An Analysis of Microscopic Structure and Its Macroscopic Implications

Rusmir Helja, BSc

November 2024

MONTANUNIVERSITÄT LEOBEN
www.unileoben.ac.at

AFFIDAVIT

I declare on oath that I wrote this thesis independently, did not use any sources and aids other than those specified, have fully and truthfully reported the use of generative methods and models of artificial intelligence, and did not otherwise use any other unauthorized aids.

I declare that I have read, understood and complied with the "Good Scientific Practice" of the Montanuniversität Leoben.

Furthermore, I declare that the electronic and printed versions of the submitted thesis are identical in form and content.

Date 22.11.2024

Signature Author
Rusmir Helja

Rusmir Helja

Master Thesis 2024

Petroleum Engineering

Quantifying the Upscaling Footprint from Pore to Darcy Scale via Pore Network Modelling: An Analysis of Microscopic Structure and Its Macroscopic Implications

Supervisor: Dr. Siroos Azizmohammadi
Co-Supervisor: Prof. Holger Ott

Chair of Reservoir Engineering

dge

MONTAN UNIVERSITÄT LEOBEN

Acknowledgments

I would like to thank my family; without them, this wouldn't have been possible.

I would like to thank Dr. Siroos Azizmohammadi for his invaluable supervision, and Prof. Holger Ott for his guidance.

Abstract

This thesis addresses the challenge of upscaling in porous media, a critical issue where the accurate prediction of continuum behavior depends on pore-scale characteristics. By employing statistical modelling, the study thoroughly investigates the upscaling footprint from pore to Darcy scale for homogeneous pore network models. Through detailed property scaling, comprehensive REV relationships that quantify the impact of microscale size and connectivity heterogeneities on continuum behavior are developed. Model-agnostic analysis concurrently reveals complex non-linear dependencies between pore-scale features and emergent flow behavior. These insights highlight the intricate nature of upscaling and underscore the necessity for precise microscale characterization to inform effective macroscopic predictions.

Zusammenfassung

Diese Dissertation befasst sich mit der Herausforderung der Upskalierung in porösen Medien, einem entscheidenden Problem, bei dem die genaue Vorhersage des Kontinuumverhaltens von pore-scale-Eigenschaften abhängt. Durch den Einsatz statistischer Modellierung wird der Upskalierungseinfluss vom Poren- bis zum Darcy-Maßstab für homogene Porennetzwerkmodelle umfassend untersucht. Mittels detaillierter Eigenschaftsskalierung werden umfassende REV-Beziehungen entwickelt, die den Einfluss mikroskaliger Heterogenitäten auf das Kontinuumverhalten quantifizieren. Gleichzeitig zeigt eine modellunabhängige Analyse komplexe nichtlineare Abhängigkeiten zwischen pore-scale-Merkmalen und dem resultierenden Strömungsverhalten auf. Diese Erkenntnisse verdeutlichen die komplexe Natur der Upskalierung und unterstreichen die Notwendigkeit einer präzisen mikroskaligen Charakterisierung, um effektive makroskopische Vorhersagen zu ermöglichen.

Table of Contents

Chapter 1

Introduction

Understanding flow and transport in porous media is key to the realization of many industrial initiatives aimed at sustainability issues, such as eco-responsible hydrocarbon recovery, enduring nutrient cycling and carbon sequestration, and waste and contaminant management. While such applications are necessarily designed for basin-spanning formations, they are fundamentally driven by pore-scale dynamics that place leading order controls on continuum behavior. Furthermore, properties that parametrize large-scale models, particularly multi-phasic ones, are typically measured at much smaller laboratory scales. This multi-scale nature poses a significant challenge in harmonizing data and processes across disparate scales to enhance the predictive accuracy of field applications.

Figure 1 provides an overview of the multi-scale modelling framework employed in the study of porous media. The diagram follows the measurement of a hypothetical property evaluated across 12 orders of magnitude, ranging from the nano to the kilometer scale. This vast range showcases the significant differences in investigation scales utilized in both academic research and industrial applications. Included in the framework are key features of pore architecture and continuum domains relevant for flow in porous media as a function of the investigation length. While physical observations are typically associated with three primary scales – the pore, core (or laboratory), and field scales – the governing mechanisms of flow and their corresponding equations of motion may vary. For instance, the nano scale might be described by molecular dynamics or models accounting for geometric constraints and high Knudsen number phenomena, the micron scale by first-principal balances such as the Navier-Stokes equations at the pore level, and larger scales by constitutive continuum models. Though the diminishing resolution of detail with increasing scale of investigation leads to an increased practical significance of flow models, it's essential to note that the behavior at any given scale fundamentally remains influenced by the physics operating at finer scales.

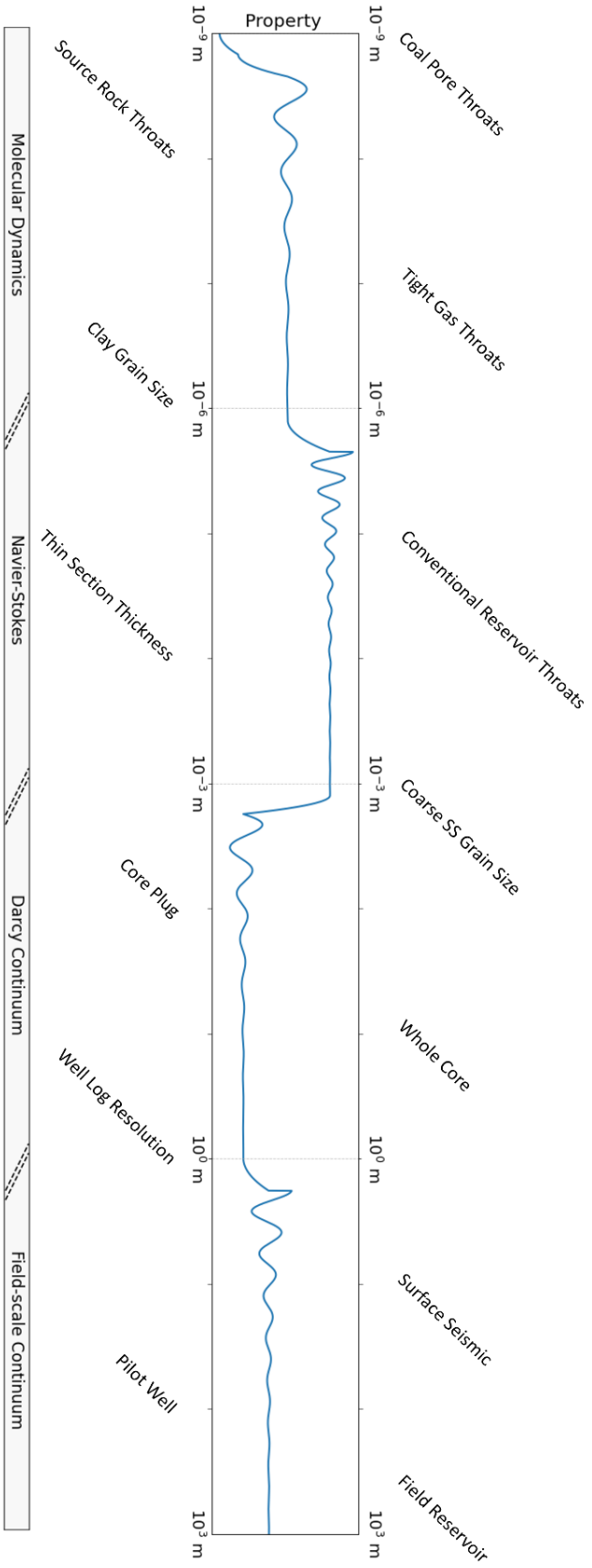

Figure 1: Theoretical fluctuation of property across orders of magnitude relevant to transport in porous media. After Nelson (2009) and Xiong (2015).

These nested hierarchies of heterogeneities make the supplantation of pore-scale variations with continuum process descriptions a non-trivial challenge. Moving to the macroscopic scale involves reducing the complexity of the domain by transforming heterogeneous fields into properties that characterize transport processes. For instance, velocity fields can be replaced by a single-valued permeability and diffusion coefficient once the scale reaches a point where the influence of microstructure on advective transport and species mixing, respectively, averages out within the field. However, to accurately model media characteristics, it is essential to capture enough pore-scale variations in the continuum models. It is crucial, therefore, to acknowledge that heterogeneities may be prevalent on all length scales extending up to the field domain, which renders upscaling a categorically localized procedure.

As an example of upscaling without necessarily considering all heterogeneity scales, measurements of multi-phase continuum properties are typically conducted on samples at a centimeter scale, raising concerns regarding the legitimacy of extrapolating core-scale results to horizons that often span kilometers. That is not to say, however, that considerable efforts are not dedicated to the examination of field-scale heterogeneities across various stages of the upstream workflow. Such efforts usually consist of process-driven sedimentological interpretations, structural inferences based on regional geology, and various models derived from geophysical and borehole data. Collectively, these endeavors contribute significantly to enhancing our understanding of preferential flow paths and predicting the performance of infiltration fronts. Nevertheless, the scientific community grapples yet with the unresolved issue of validating the upscaling process from the microscopic pore level to the broader field scale. The critical obstacle to this unresolved challenge is the difficulty of accurately delineating scales in a manner that comprehensively addresses the complete hierarchy of heterogeneities.

High-resolution imaging technologies such as X-ray computed tomography (micro-CT) have unlocked the direct visualization of pore-scale microstructure and the distribution of dynamic flow-field variables. These advancements have permitted researchers to construct intricate 3D models that facilitate the exploration of complex fluid flow phenomena, including multi-phase displacement and hysteresis. Additionally, these 3D models serve as simulation domains for advanced numerical methods that leverage high-performance computing to gain valuable insights into the upscaling process.

Tomographic imaging offers a powerful non-invasive means of characterizing the microstructure and contrast between fluid phases in porous media through detailed 3D visualizations. This method stands apart from traditional techniques like porosimetry and microscopy as it provides a quantitative insight into volume topology. Analyses typically depend on post-processed images of grayscale captures, which might introduce artifacts into the analysis. The biggest limitation of high-resolution tomography, though, is the requisite use

of smaller specimen sizes, which constraints the overall scope of the sample under study. Micro-computed tomography (mCT) for instance, can achieve spatial resolutions down to 1 micron. This field of view allows for the direct observation of flow and transport dynamics through time-resolved images. However, sub-micron features might elude identification, potentially leaving portions of the structure unresolved in the digital models. Such omissions can lead to discrepancies between properties inferred from tomographic data and those derived from experimental results (Rozenbaum, 2011). For investigations at the nanoscale, especially when analyzing complex morphologies, Focused Ion Beam (FIB) nanotomography presents an alternative, for example when investigating clay rocks as part of an unconventional study (Keller et al., 2013).

In recent years, Digital Rock Physics (DRP) has emerged as a burgeoning methodology that utilizes digital models in conjunction with high-performance computing to simulate petrophysical properties. DRP represents a cost-effective and time-efficient alternative to conventional laboratory methods, particularly for complex multi-phase phenomena. By employing numerical methods to solve flow fields of percolating fluids, valuable insights on various pore-scale processes can be obtained, complex models such as on reactive transport calibrated, and continuum descriptions validated (Jiang et al., 2016). Naturally, this includes the possibility to investigate the impact of pore structure on continuum behavior. Because DRP schemes incur significant computational cost, the domain size ought to be optimized for performance while maintaining the representativity of results. Continuum modelling however will likely remain the principal approach in the foreseeable future for practicable characterization on broader scales where continuum mechanics operate.

It is crucial therefore to be able to systematically transition between the pore and continuum scale by honoring the underlying dynamics. This transition is called upscaling and attempts to relate the statistical distributions on the pore scale to effective properties on the continuum scale. The continuum framework is established by upscaling pore-scale conservation laws over an appropriately large dimension such that a porous medium can be treated as a continuum described by single-valued properties that emerge from explicit realizations of pore fields. Therefore, continuum-scale modelling imposes strict assumptions about porous media in order to implement closed-form equations parametrized by aggregate properties.

Historically, continuum descriptions of flow in porous media have been primarily empirical or semi-empirical. Their empirical nature originated from large-scale experiments without a precise understanding of how pore properties translated to bulk behavior. The most common constitutive law in porous media is Darcy's Law, which models the potential loss of non-inertial flow. Other common laws include Fick's Law and Fourier's Law for modelling mass and heat

fluxes. The effective coefficients parametrizing constitutive laws are usually measured experimentally at the core scale, and while such equations provide some qualitative insights, there was an absence of a rigorous mathematical framework delineating the conditions under which continuum modelling was valid or how it might be extended to more complex scenarios. It is in this context that upscaling theories emerged in the latter half of the 20th century as a systematic way to bridge the conceptual gap between pore-level physics and the larger-scale continuum descriptions. The aim of upscaling is thus to explain effective properties based on pore-scale features. Some of the most popular theories include the volume averaging theory (VAT) and the homogenization theory.

The volume averaging theory (VAT) has been used extensively to derive macroscopic equations from conservation equations by averaging pore-scale heterogeneities over a domain of investigation. Each microstructural quantity is cast as a decomposition of its space-dependent volume average and a local fluctuation term. Substituting the decomposition into the governing equations and then applying the spatial averaging theorem provides a set of continuum equations in terms of the volume-averaged quantities. Homogenization theory originates from the study of differential equations with rapidly oscillating coefficients and finds purposeful application in porous media where the oscillations arise from microstructural heterogeneities. Central to this theory is the assumption of spatial periodicity in the heterogeneities, represented by the condition

$$\frac{\varepsilon}{L} \ll 1 \tag{1}$$

where ε is a pore-scale characteristic length and L denotes the domain length. By imposing this separation of scales, pore-scale field quantities undergo double-scale asymptotic expansions, which are subsequently integrated into the appropriate equations of motion to derive macroscopic continuum models. In both approaches, the volume-averaged equations may contain terms involving higher-order correlations of the fluctuations quantities whose resolution may require additional assumptions, which is referred to as the closure problem. The closure problem may also be required to set proper boundary conditions on the macroscopic scale.

The result of these complexities is that in all but the simplest problems these pore-to-continuum upscaling methods are not practically applicable. Their primary value, however, lies in the conceptual foundation behind the origins of continuum-scale equations and the understanding thereby established. Although the result is a predetermined outcome, these theories are key to explaining how and why continuum models work as averaged manifestations of underlying pore-scale physics and under what conditions they might fail or require corrections, such as larger Reynolds numbers for non-inertial flow and multi-phase flow effects.

The crux of these upscaling theories is ensuring a separation between the pore and continuum scales. The requisite degree of this separation depends on the microstructural heterogeneities; specifically, the region of interest (ROI) must be sufficiently small relative to the entire domain yet expansive enough to encapsulate a statistically representative set of property values. Consequently, averaged quantities should converge towards consistent values within a Representative Elementary Volume (REV). In such an ergodic system, the ensemble and spatial averages become identical.

Upscaling is not exclusively confined to the transition from pore-to-continuum scales but often involves moving from one continuum scale to a coarser one. The rationale behind continuum-to-continuum upscaling is twofold: to bridge the gap between scales at which detailed property measurements are made and those at which field-flow simulations are performed, and to replace intricate models with more tractable versions. In reservoir engineering, continuum-to-continuum upscaling plays a crucial role. By reducing the grid cell count in simulation models, computational efficiency is enhanced – both in terms of runtime and resource utilization. Upscaled models thus offer faster turn-around times that expedite simulation studies across multiple development scenarios, uncertainty assessment in reservoir and operational parameters, and history-matching procedures.

However, the utility of upscaling is contingent upon its accurate application. In the current state-of-the-art upscaling, there is a lack of a standardized theoretical framework to evaluate the quality and robustness of upscaled models, without referencing the results of finer-scale counterparts or resorting to post-hoc history matching. In the context of flow in porous media, the upscaled grid ought to mirror fluxes obtained on finer models under consistent boundary conditions. This presents a complex challenge, as heterogeneities often impact flow considerations and patterns on larger scales. Thus, preserving the heterogeneity fingerprint becomes paramount for the coarse-scale model's accuracy. A loss in the intricate details of the original heterogeneity can compromise the fidelity of upscaled models.

There are numerous methods in the upscaling toolkit that can be classified broadly as analytical and numerical. Analytically, methods often employ some combination of power averages – such as arithmetic, geometric, and harmonic means – or mathematical techniques such as iterative renormalization groups, to transition models to coarser representations by aggregating properties systematically. Simulation methods, on the other hand, leverage computational solutions to underlying continuum equations and can be subdivided into diagonal methods, which simplify anisotropy representation, and full tensor methods, which capture anisotropy in its entirety. Furthermore, there have been several studies that explored the potential of deep learning applications. Ultimately, the choice of upscaling method depends on the properties in

question, the grid structure, and the prevailing boundary conditions, with an engineering trade-off between accuracy and computational cost.

This thesis addresses the complexities of upscaling in porous media, where accurate prediction of continuum behavior critically depends on detailed pore-scale characteristics through the use of pore network modelling. It specifically targets a gap in the literature concerning the thorough investigation of the upscaling footprint from pore to Darcy scale. The aim is to establish a robust link between microscopic structural details and their macroscopic implications through detailed, property-specific characterization of pore-scale structure and a statistical modeling approach. This approach is used to determine the extent to which microscopic descriptors control continuum behavior across different scales and includes a comprehensive Representative Elementary Volume (REV) analysis.

Chapter 2

Literature Review

2.1 Methods to Characterize Microstructure

There are numerous methods to characterize pore structure. One of the most fundamental and important sets of metrics stems from integral geometry and assigns measures to geometrical space that are invariant under the natural symmetries of that space. The Minkowski functionals are universally utilized to characterize pore-scale structures and multiphasic distributions of bulk in porous media (Armstrong et al., 2018). A cornerstone result that underscores the practical implications of the Minkowski functionals is Hadwiger's theorem, which states that for any additive and continuous d-dimensional valuation v that is motion-invariant, there exist coefficients c_i such that in the space of convex bodies S

$$v(S) = \sum_{i=0}^{n} c_i W_i(S) \tag{2}$$

Where W_i are the intrinsic volumes, which in three dimensions amount to

Volume $W_3(S)$ represents the total space occupied by the object, which is crucial for determining the storage capacity and mass of a medium.

Surface area $W_2(S)$ is an important scaling parameter for processes involving surface phenomena, directly influencing the object's ability to interact with its environment.

Integral mean curvature $W_1(S)$ is related to the mechanical properties of an object, including the phase distributions due to capillary phenomena.

Euler characteristic $W_0(S)$ as a topological invariant that provides information about the connectivity of a structure, which is relevant for flow and transport considerations.

By expressing any continuous, translation and rotation invariant valuation as a linear combination of these intrinsic volumes, Hadwiger's theorem reveals the $d+1$ Minkowski functionals as the sole building block required for a complete classification of a vast group of measures, which enables researchers to develop models that can predict the behavior of complex systems based on their geometric and topological characteristics. Although the Minkowski functionals offer a direct and symmetric characterization of pore structure, they fall short in describing properties that do not meet the criteria established by Hadwiger's theorem. One significant limitation involves non-additive properties that depend on the detailed interactions between components rather than simply being the sum of individual contributions. Another one is with non-motion-invariant properties that depend on the specific alignment of the material's internal structure relative to an external reference frame. Furthermore, Minkowski functionals are restricted to providing global measures and do not offer local information about the spatial distribution of these properties within the structure. This insensitivity to fine details means that while they can describe overall shape and connectivity, they may overlook small-scale features that are crucial for understanding medium properties. These limitations necessitate the use of additional characterization methods that can address these aspects more effectively.

Fractal theory offers a distinctive approach to quantifying structural complexities across scales. A fractal is a shape with non-integer dimensions that exhibits properties of self-similarity. Natural porous media only approximate a fractal character in terms of self-affinity. The fractal dimension is a characteristic measure that captures the scale invariance of a domain and provides insight into the complexity of pore space. Despite the challenges in estimating the fractal dimension of porous media, analytical methods such as the Rieu-Sposito (RS) model have been developed to relate it to measures such as the pore size distribution (Xia et al., 2018).

Furthermore, the Minkowski functionals are not capable of reproducing the spatial correlation of pore space. The study of random heterogeneous media provides a rigorous and oriented method to quantify the spatial dissimilarity of pore-scale features and their effects on continuum properties (Torquato, 2005). Canonical correlation functions capture the probability of some spatial occurrence as a function of distance between points. Since such functions describe the fingerprint of structural disorder, each value is an agglomeration of multiple conditional realizations for a prescribed error bound. In particular, n-point correlation functions represent the probability that each of n randomly positioned points separated by a correlation length r falls into a specific phase. Correlation functions deliver information on how randomly distributed point ensembles are correlated in space, thereby reflecting the structure of the pore space itself. Differences in the correlation function with direction have been used to quantify

the anisotropy of porous media (Rozenbaum & du Roscoat, 2014). There are various other statistical measures of a medium's microstructure depending on the application; two of the most common ones are the lineal path function, which describes a medium's capacity to accommodate linear flow paths, and the chord distribution function and density function, which measure the distance between interfaces (Levitz, 1998).

Minkowski functionals do not explicitly address the emergence of long-range connectivity patterns in a porous medium. Percolation theory, on the other hand, has been applied extensively in understanding how coordinated bulk behavior arises from the interaction of individual pore-scale elements. The interaction of individual pore-scale elements gives rise to coordinated bulk behavior in porous media (Hunt and Ewing, 2009). At the core of percolation theory lies the concept of a phase transition that occurs at a critical point where connectivity is established in the form of a percolating cluster. In most cases, there emerges a single percolating cluster which accounts for most of the effective porosity (Jarvis, 2016; Keller et al., 2013; Renard & Allard, 2013). Cluster properties are characterized by power-law relationships that provide insight into the scale-dependence of the underlying pore structure. The percolation threshold and the associated critical phenomena provide a foundation for generalizing the application of percolation theory to any porous network.

Numerous studies have applied percolation theory to various aspects of porous media. Ewing et al. (2010) investigated the influence nonuniform porosity distributions on diffusion phenomena near the percolation threshold using scaling relationships, while Jarvis et al. (2017) explored the connectivity of pore spaces using cluster statistics. Keller et al. (2013) and Pringle et al. (2009) studied anisotropy in the percolation threshold, the latter also characterizing the temperature-dependence of length scales governing transport. Various descriptors have been developed to characterize connectivity in terms of cluster statistics. Connection probability represents the probability that pores within an investigation volume are part of the same cluster; it is biased towards larger clusters and is less sensitive than the Euler Characteristic to local perturbations. Koestel et al. (2020) observed that the connection probability decreases with investigation scale due to the greater likelihood of capturing unconnected clusters.

Beyond connection probability, parameters such as the fraction of pore space in the largest cluster and the probability that two random pores belong to the largest cluster provide additional information on cluster statistics (Jarvis, 2016). Another powerful tool to analyze connectivity is Local Probability Theory (LPT). This sampling method constructs distributions that account for connectivity heterogeneity as a function of porosity (Biswal, Manwart, & Hilfer, 1998; Hilfer & Lemmer, 2015). In LPT, percolation probability $\lambda(\phi, L)$ represents the probability to find a percolating pathway across a window of size L and porosity ϕ. LPT permits a scaling

and anisotropy assessment of connectivity structures (Regenauer-Lieb et al., 2017; Keller et al., 2013).

2.2 Microstructural Impact on Single-Phase Flow

The size distributions of pore-scale features exert a significant impact on continuum behavior. Pore throats, in particular, act as conductive constraints that control flow and capillary displacement, taking up most of the pressure drop in a pore-throat conduit and thus affecting permeability strongly. Pore throat distributions are intimately tied to the pore size and seem predisposed to lognormal forms in natural media (Xiong et al., 2021).

The broadness of pore and throat size distributions is a well-observed source of heterogeneity in literature. More heterogeneous size distributions lead to a greater space-filling effect due to a more efficient accommodation of different sizes, resulting in a reduced porosity and poorer connectivity; broader distributions likewise create a greater variety in the shape of generally shorter and narrower throats (Peng-Fei et al., 2022). With increasing grain size, the peaks of size distributions shift rightwards due to the larger pore space. Furthermore, the number of pores and throats has been observed to become smaller as diameter increases in natural media. Xiong et al. (2021) reported lower permeabilities for both fine-grained media and media with wider particle size distributions. This is in line with the general power-law trend of permeability being affected disproportionately by larger pores and thus having a positive correlation with pore diameter and a negative correlation with pore variance (Hamamoto et al., 2016). Furthermore, there is a well-established trend in most porous media where permeability decreases with porosity. Besides the implication of decreasing pore diameter, this relationship may be explained by the conceptual model that the reduction in available pore space results in a lower density of conducting pathways (Ewing et al., 2010; Hamamoto et al., 2009).

Though permeability has been investigated extensively in the scientific community and is the cornerstone for nearly all Darcian advective models, the exact relationship to pore-scale heterogeneities remains an unresolved technical challenge, particularly in complex porous media. Despite significant efforts to develop accurate models, there is still much to be learned about the underlying mechanisms that govern permeability in these systems.

The biggest challenge is to find a representative way to quantify permeability through structural observables. Analytical models include the capillary bundle model that assumes a bundle of stream tubes, permeability bounds that depend on statistical correlation functions (Rubinstein and Torquato, 1989), and the Kozeny-Carman equation which refines the permeability estimation through empirical constants based on tortuosity and specific surface area. However, the applicability of such models outside the idealized conditions for which they are valid is

limited, and they often overestimate permeability for strongly heterogeneous or poorly connected media (Mostaghimi et al., 2012).

Thus, a multitude of empirical models have been proposed to estimate permeability from properties like grain size (Berg, 1970), critical percolation diameter (Skaggs, 2011), autocorrelation length (Ioannidis et al., 1996), and NMR relaxation time (Banavar and Schwartz, 1987). The issue is that these relations differ greatly, which highlights the non-unique relationship between permeability and the heterogeneities of different pore-scale aspects that cannot be condensed into a single correlation.

Nonetheless, based on the extensive work done in the field of permeability modelling, important qualitative conclusions have been reached regarding the nature of the relationships between permeability and pore-scale heterogeneities. For example, Xiong et al., (2022) simulated the permeability of media with different grain sizes and angularities and found that the permeability was lower for more angular sands in the same sieving size range due to lower pore coordination numbers. In general, higher pore coordination numbers seem to enhance the permeability. But pore and throat size distributions alone offer no information on the spatial arrangement of individual elements (Tao et al., 2019). It has been observed for example that smaller pore-scale features contribute disproportionately to the connectivity between larger pore clusters (Koestel et al., 2020), such that increasing the dimensions of well-connected pores does not lead to an appreciable increase in the permeability (Kai Xu et al., 2022). Permeability, however, has been observed to decrease exponentially with a reduction in the overall throat to pore ratio (An et al., 2015; Kai Xu 2020).

More complex pore spaces arise from irregular grain shapes, which leads to a wider distribution of shape factors and pore coordination numbers (Peng-Fei et al., 2022). Pore shape and angularity also have a strong impact on continuum properties. Pore elements manifest in a wide variety of geometric profiles depending on the burial and diagenetic conditions, with the particular shape of an element typically described in terms of its sphericity and angularity, and often expressed as a deviation from the proportions of a sphere. Xiong et al., (2022) for instance performed a Fourier analysis of SEM images to find that the throat radius and coordination number of more angular sandstones are larger than those of rounder beads with the same sieving size.

Generally, more complex pore spaces seem to arise from irregular grain shapes, which leads to a wider distribution of shape factors and pore coordination numbers (Peng-Fei et al., 2022). For a fixed volume, non-spheroidal elements offer greater specific surface area to interfacial phenomena, which is why diffusion-based models ought to consider the shape factor to predict sorption more accurately (Ewing et al., 2010). Additionally, pore aspect ratio affects the

porosity profile (Katagiri et al., 2014). The specific surface area is therefore an indicator of shape irregularity. In a similar vein, greater surface roughness increases specific surface area and, consequently, adsorption capacity (Vanson et al., 2017). Moreover, Vanson et al., (2017) found that roughness can alter boundary conditions and lead to low-pressure velocity profiles, manifesting on the continuum scale as an inverse relationship to permeability. Whereas the permeability does not seem to change appreciably with the shape for otherwise identical structures, the shape factor assumes a central role in certain empirical relations such as the Kozeny-Carman equation as a curve-fitting parameter, implying that the relationship between pore shape and permeability is implicitly mediated through the porosity and packing structure (An et al., 2016; Katagiri et al., 2014). However, the shape factor has a strong influence on the relative permeability curves of a medium, such that sharper pore corners generate phase distributions with higher wetting phase relative permeabilities at the cost of larger non-wetting residual saturations (An et al., 2016).

The presence of directional bias in the orientations of pore elements is a key component of the spatial organization of microstructure. Anisotropy strongly influences the hydraulic continuum behavior of porous medium. Tao et al., (2020) quantified the pore-scale anisotropy of tight sandstone models and assessed the impact of microstructural controls on continuum properties. Though most static parameters showcased no meaningful correlation with anisotropy, the tortuosity displayed a negative correlation, representing the mechanism that controls the directional dependence of permeability. In most sedimentary rocks, the horizontal permeability is larger than the vertical one, in what is well-accepted as due to the biased grain direction during deposition.

The comprehensive characterization of topology in porous media is crucial for understanding flow and transport processes at various scales, as the connectivity of microstructure directly influences dynamic properties and their sensitivity to heterogeneous flow paths (Renard Allard, 2011). The effective transmission of fluid through a network is not only important for permeability characterization but also for interfacial phenomena (Ewing et al., 2010, Vanson et al., 2017). Furthermore, studies have shown that connectivity has a strong impact on multi-phase phenomena, shaping immiscible invasion patterns and saturation-dependent functions such as relative permeability curves (Ju et at., 2022; Renard Allard., 2011). As such, knowledge of connectivity is essential for performance forecasts and upscaling analysis.

Despite its central role, quantifying connectivity and understanding its relationship with Darcian properties remains a challenge. The porous media community has yet to agree on a universal mathematical definition, as connectivity is a broad, application-specific concept encompassing both static and dynamic metrics. Static metrics depend solely on pore structure,

whereas dynamic metrics are more diverse as they are obtained by considering physical processes that incorporate not only the structure but also boundary conditions and state variables. In DRP, dynamic metrics such as hydraulic and diffusive tortuosity are implicit properties calculated by specific simulation methods.

The coordination number is a common static metric that describes the number of throats linking a pore to its neighbors and serves as a fundamental characteristic of topology, typically taking on average values between 3 and 9 across various media types (Jiang et al., 2020, Xiong et al., 2022, An et al., 2015). While Xiong et al. (2022) reported smaller mean coordination numbers with large pore sizes, Hamamoto et al., (2016) found this effect insignificant, and Peng-Fei et al., (2022) observed no discernible relationship between pore size and connectivity. These conflicting results may stem from the varied media types studied. Hamamoto et al., (2016) however concurrently observed a significant reduction in sample tortuosity with pore size. This implies that tortuosity should be considered as a potentially superior indicator of connectivity because the coordination number delivers no meaningful information on the spatial arrangement of connected pores.

The observations by An et al., (2015) reinforce this notion, as a strong anisotropic effect on permeability was noted between pore network models with similar size and coordination number distributions but different pore orientations. Tortuosity has also been shown to decrease with increasing porosity and pore coordination number due to a smaller variance in path lengths (Provis et al., 2012; Xiong et al., 2022). On the other hand, compaction-induced porosity reduction was observed to increase the coordination number, even as denser packings exhibited higher tortuosity, as what Hamamoto et al., (2016) interpreted in terms of elongated pores at a reduced inactive porosity. In a statistical sense, connectivity is linked to the probability of finding a conductive pathway from one location to another, meaning that both coordination number and throat dimensions along a pathway are relevant to consider. Disentangling the effect of connectivity on permeability from size distributions thus becomes a complex task (Kai Xu et al., 2022).

2.3 Representative Elementary Volume

Because spatial dependencies are a ubiquitous phenomenon in most physical processes, understanding and confirming the existence of the Representative Elementary Volume (REV) is paramount in the study of flow and transport in porous media. The REV is thus critical to the Darcian framework by enabling the effective upscaling of flow performance in media that adhere to statistical homogeneity.

Though there are different definitions for REVs, each one rests on the keystone assumption that heterogeneities need to be delineated through a unique separation of scales. The most basic and critical requirement for defining the REV scale is that it acts as the lower and upper bound for the characteristic length of macroscopic heterogeneities and microscopic fluctuations, respectively. In inequality form

$$l_{microscopic} \leq l_{REV} \leq l_{macroscopic} \tag{3}$$

To ensure that this scale separation is feasible and for upscaling to be valid, the REV must be large enough to encompass a statistically representative number of microstructural features and flow mechanisms, allowing for Darcian effective moduli to be independent of the investigation scale. However, the REV should also be small enough to ensure that the moduli accurately characterize the macroscopic behavior of the medium without having reached macroscopic heterogeneities.

When the investigation scale is sized between $l_{microscopic}$ and $l_{macroscopic}$, the property is expected to have only minor fluctuations because it is structurally typical of the pore-scale heterogeneities. Within this plateau, measurements are scale-independent and consequently provide practical and consistent readings. These measurements can be used to reliably parametrize a continuum model, which supplants the pore-scale description (Baveye et al., 2002). Measurements taken at scales below $l_{microscopic}$ maybe susceptible to the disparate influence of pore-scale heterogeneities because only a spatially unrepresentative portion of the medium is captured. Similarly, measurements above $l_{macroscopic}$ may capture large-scale variability in the macroscopic structure due to spatial changes in mineralogy or texture in the sedimentary profile that cause deviations from a stabilized value.

Only practical and consistent measurements inside the REV range may reliably parametrize continuum models (Baveye et al., 2002). Since Darcian properties are upscaled entities, the presence of multi-scale heterogeneities with spatial correlation lengths that deny a meaningful delineation may make the identification of the upper and lower bounds difficult and invalidate the existence of an REV (Constanza-Robinson et al., 2011). These considerations lead to the most common definition of REV for a homogeneous medium: the range of lengths for which an averaged property converges to a constant value with incremental changes in the investigation scale (Bear, 1972). For some property $Y(\boldsymbol{x}, l)$ that is a function of location $\boldsymbol{x}$ and scale l this requires

$$\left.\frac{\partial Y(\boldsymbol{x}, l)}{\partial l}\right|_{l=l_{REV}} = 0 \tag{4}$$

The requirement for no change whatsoever in the studied property as a criterion for REV existence is too rigid, as it does not account for the presence of noise and fluctuations due to finite-sized samples that make it impossible to find more than two consequent points with the same property value. The condition is commonly relaxed in practice by introducing a pre-defined tolerance margin, which, despite its widespread use, lacks a rigorous scientific justification. It is also worth noting that the choice of threshold may significantly affect the resulting REV size estimate (Gerke & Karsanina, 2020; Rahman et al., 2020). The relaxed form of the convergence criterion:

$$\left.\frac{\partial Y(\boldsymbol{x}, l)}{\partial l}\right|_{l=l_{REV}} \approx 0 \tag{5}$$

Increasing the investigation scale should not lead to appreciable changes of Y as it parametrizes a model that represents the average constitutive response with sufficient accuracy. Properties that do not obey the relaxed criterion are considered not to have attained the REV and may require additional data analysis or may need to be excluded from the analysis altogether (Constanza-Robinson et al., 2011; Borges et al., 2018).

2.3.1 Analysis Methods

There are two principal ways to conduct a REV analysis depending on the characteristics of the medium and study requirements. The deterministic REV (d-REV) is found by repeatedly calculating a property in a sequence of expanding volumes anchored to a single point in the domain. The d-REV then corresponds to the volume over which fluctuations decay and the property converges with increasing window size. The d-REV approach makes up the traditional volume averaging procedure for REV determination in literature and typically involves the placement of a single point either through aleatory means or at the center of the domain (Al-Raoush & Papadopoulos, 2010; Borges et al., 2018).

To observe the spatial variability of a property, the statistical REV (s-REV) provides an alternative approach. The s-REV is obtained through a moving window approach that involves sampling properties across the medium. The medium is split into discrete volumes and a property is calculated on each placement for incremental window sizes. An s-REV is then defined as the window size beyond which both the mean and variance of the property become constant. Since a statistical analysis assesses the spatial dispersion of a property, the statistical significance of results depends on the number of independent windows, the relative precision in estimating the s-REV, and the degree to which windows overlap. Overlapping windows leads to an artificial reduction of variance, which places a natural upper bound on the investigation size (Brown et al., 2000). Though each property in the study of Koestel et al. (2020) meets the

lower-bound for d-REV, for connectivity measures based on percolation theory the lower-bound was found only in the scale range where the windows overlapped.

Though both approaches satisfy the definition of REV as presented earlier for the convergence of property values, the s-REV places an additional set of conditions by requiring the property to be treated as a stationary function in the medium for any $\boldsymbol{x}$

$$E[Y(\boldsymbol{x}, l_{REV})] \approx constant \tag{6}$$

and

$$Var[Y(\boldsymbol{x}, l_{REV})] \approx constant \tag{7}$$

where $E[Y(\boldsymbol{x}, l_{REV})$ and $Var[Y(\boldsymbol{x}, l_{REV})]$ are the mean and variance of Y within the REV range of scales, respectively. Estimating s-REV is the recommended approach due to its explicit consideration of medium-wide heterogeneity (Lake & Srinivasan, 2004; Ozelim & Cavalcante, 2018). A geostatistical approach that uses a measure of spatial dissimilarity in the form of semivariograms for REV determination is seeing increasing application in pore-scale analysis (Jackson et al., 2020).

2.3.2 Sampling Methods

The most common d-REV sampling technique used to average unique portions of a medium is the expanding prism method. This method involves continuously extending a rectangular prism and is classified according to the evolution of the volume centroid. In the point-centered sampling scheme, concentric volumes are centered on a point held constant in space. Alternatively, in the face-centered sampling scheme, successive volumes extend outward from the same boundary face or corner. Baveye et al. (2002) reported negligible differences between the two sampling techniques, albeit for an apparently homogeneous soil sample. This finding suggests that, under the conditions approaching statistical homogeneity, either technique may be suitable for obtaining averaged information about a medium.

However, in the context of analyzing heterogeneous media, the choice of sampling technique can significantly affect the accuracy of the estimated Darcian properties because a single window may fail to capture the spatial variability of the medium, leading to biased estimates. This is demonstrated in studies that constructed face-out windows from the corners of samples with varying degrees of heterogeneity, producing up to eight independent realizations with drifting window centers. Notably, the more heterogeneous samples (e.g., dolomitic cores with gypsum intrusions) showed considerably more variation among the individual curves for

calculated properties (Brown et al., 2000, Koestel et al., 2020, Peng-Fei et al., 2022). Such a face-out scheme might be useful for a preliminary evaluation of heterogeneity prior to the evaluation of a more comprehensive s-REV.

Window geometry may also exert a strong influence on REV assessment. An isotropically expanded cube is the most frequently used window geometry (Mu et al., 2016, Borges et al., 2018, etc.), although cylindrical volumes are also prevalent (Al-Raoush & Papadopoulos, 2010). It is nonetheless possible to adjust the aspect ratio of the window to better fit the geometry and approximate the heterogeneity of the medium, as in the study of Constanza-Robinson et al. (2011) where a core-centered window was accommodated to the height of the sample. The resulting d-REV estimate for porosity was lower than for the cubic geometry, attributed to averaging out the variation with height. This greater insensitivity to microscopic variation leads to smoother REV curves but makes facilitating comparison with literature difficult.

2.3.3 Estimation Methods

The most direct method to determine the d-REV range is through visual observation of the plateau. But in the absence of a quantitative analysis there is no clear indication whether a property has converged or is still a function of the window size. Qualitative criteria are therefore required to avoid ambiguity regarding the existence and location of the REV range. More accurate and reliable methods for testing the convergence of property descriptors can be derived from numerical approximations for a discrete set of investigated windows. A center-difference approximation of l_{min} leads to

$$\frac{Y_{l_{i+1}} - Y_{l_{i-1}}}{l_{i+1} - l_{i-1}} \approx 0 \tag{8}$$

where the subscript i refers to the window size. The approximation as estimated above depends on the property being investigated and on the system of units. A more standardized REV criterion that can be used comparatively across different properties and media is formulated by nondimensionalizing Eq (above) to express the relative error of a property as

$$\left\| \frac{Y_{l_{i+1}} - Y_{l_{i-1}}}{Y_{l_{i+1}} + Y_{l_{i-1}}} \right\| \approx 0 \tag{9}$$

representing the change in a property as a fraction of the sum of $Y_{l_{i+1}}$ and $Y_{l_{i-1}}$, circumventing the dependence on specific units and improving the consistency of results (Li et al. 2009). The lower bound of the REV range is then the minimum window scale l for which the relative change over the given size increment remains below an ad hoc threshold, frequently taken as 0.2 or 0.1. Further subjectivity is introduced by the choice of how many consecutive window sizes must sustain an acceptable relative deviation. Determining the preferred combination of threshold and number of successive points remains a challenge due to the lack of established objective criteria. It is also interesting to note that these criteria are usually used to investigate the potential existence of l_{min}, with only a few studies having attempted to disentangle the heterogeneity bounds and investigate the existence of l_{max}, to varying degrees of success.

For s-REV determination, the issue of spatial variability needs to be addressed. Since the REV might vary across a medium for each Darcian property of interest, the statistical profile of each property as a function of window size must be investigated. Simply ensuring that the mean of a property fulfills convergence criteria is not sufficient. The standard deviation, which measures the spread of the property around the mean, must also converge to a sufficiently small value with increasing window size. In other words, an approximately constant mean and low standard deviation are necessary conditions for the s-REV range existence.

A divergent statistic implies that due to unbounded heterogeneity in either the microscopic or macroscopic scale an s-REV range cannot be determined. The lower bound of the s-REV range is therefore, the scale below which the mean varies significantly, or the standard deviation is large enough so the domain cannot be treated as approximately homogeneous. It is practical to define a global convergence measure rather than evaluating the two variables separately. Such a measure should consider both the mean and the standard deviation to determine the s-REV range accurately. The coefficient of variation (CV) expresses the deviation of a variable relative to its mean and is defined as the ratio of the standard deviation to the mean

$$CV = \frac{\sigma}{\mu} \tag{10}$$

The CV can evaluate the convergence of both the mean and standard deviation, with an asymptotic limit indicating that an s-REV range may exist. Moreover, the CV is useful for comparing variability between different datasets. However, the choice of cut-off threshold for testing statistical homogeneity appears to be largely arbitrary in the literature. Some studies define a medium as heterogeneous if the CV is greater than 0.5 (Corbett & Jensen, 1992; Nordahl & Ringrose, 2008), while others propose much lower thresholds such as 0.2 or 0.1 to identify the lower s-REV scale (Zhang et al. 2000, Bruns et al. 2017, Singh et al., 2020). In particular, Rahman et al. (2020) opted for a threshold of 0.05 to be consistent with pycnometric

measurements and noted that under the assumption of similar sandstone samples, s-REV increased a hundred-fold compared to the estimation by Zhang et al. (2000). Because the level of accuracy exerts a strong control on the estimated s-REV range, the cut-off needs to be chosen with forethought for desired accuracy and compatibility with experimental results. As of writing the author is not aware of literature that systematically tests the dependence of s-REV estimation on threshold values. Therefore, further research is necessary to determine the most appropriate cut-off threshold for estimating s-REV ranges.

It is also possible to evaluate the conditions of statistical homogeneity through an appropriate statistical test. Statistical testing encompasses a diverse range of techniques for analyzing datasets that involve more than two treatments. The principle behind testing the null hypothesis of mean and standard deviation constancy across successive window sizes involves partitioning the total variation in the datasets into within-group and between-group variation. Brown et al. (2000) employed one-way Analysis of Variance (ANOVA) and Hartley's test to investigate mean and variance equivalence, respectively, of static properties with increasing volume in dolomitic cores. However, the limited sample size, consisting of only eight corner-out realizations for each investigation scale, raises concerns about the statistical power of their results. The interpretation of statistical differences strongly depends on sample size, which should be large enough to accurately represent the underlying distributions and allow for reliable inferences. It is therefore imperative to base any statistical tests on a domain-wide s-REV approach.

Another limitation to consider is potentially prohibitive assumptions behind procedures like ANOVA and Hartley's such as that data are normally distributed. In general, the evaluation of confidence intervals gives a clearer idea of how closely statistics estimate population parameters. Ozelim et al. (2018) used a bootstrap algorithm to test the null hypothesis that samples from consecutive window sizes stem from the same distributions for sandstone and claystone. Their study showed that more than one interval of statistical equivalence exists, highlighting the presence of heterogeneities at multiple scales. This also suggests that in natural media, finding a unique REV may not always be possible. As a workaround for this issue, Rahman et al. (2020) proposed a regression model that estimates the window size by extrapolating variance to zero. This method eliminates the need for a subjective threshold and arrives at a unique yet unphysical s-REV estimate.

Statistical models can also offer insights into the connection between the sampling method and the accuracy of the resulting estimations without requiring information on the pore-scale structure. Kanit et al. (2003) proposed a sampling theory-based model in a geostatistical context that provides a formula for the minimum window size required to achieve a specified

convergence threshold for a given integral range of spatial covariances. The model predicts that estimates of the s-REV display exponential-type variation as a function of the threshold value.

2.3.4 Applications

The dependence of the REV range on the specific property under investigation has been widely acknowledged in the scientific community. This dependence arises from the fact that the same averaged heterogeneities exert varying degrees and types of upscaling control, contingent upon the property being studied. Flow-based properties, such as permeability and saturation, that are intricately influenced by dynamic features that may vary with boundary conditions, in general, require a larger window size for representativity (Mostaghimi et al., 2012; Mu et al., 2016; Jackson et al., 2020). Conversely, purely geometric properties, such as porosity and specific surface area, which remain fixed within a given domain and are expressible through Minkowski functionals, typically exhibit a smaller REV. Studies have routinely demonstrated that when estimating the lower bounds for porosity and specific surface area, the investigated samples were usually significantly larger than the resulting REV values. The same cannot be said for properties such as permeability in highly heterogeneous media, where the sample might not be large enough to deliver a representative estimate (Mostaghimi et al., 2012).

This underscores two important observations about the REV in porous media. The first observation highlights that static properties possess a comparatively smaller spatial scale of correlated heterogeneities, necessitating a smaller REV for accurate representation. The second observation emphasizes that to avoid the misidentification of the REV, the REV of one property cannot be used as a reference to obtain representative measurements of other another. These observations have significant implications for the design and interpretation of experiments and simulations based on property-specific REV behavior. Failure to account for such heterogeneities may result in inaccurate representations of continuum models, leading to erroneous upscaling and suboptimal design decisions. It is therefore crucial to adopt a rigorous approach to determining the appropriate REV by using precise statistical methods.

In addition, the variability of REV with rock type is a well-established phenomenon that is important to consider. REV analyses have been conducted on various porous media, natural and artificial, revealing significant differences in estimated REV due to distinct pore-scale dimensions and degrees of structural homogeneity. For instance, Mostaghimi et al. (2012) and Rahman et al. (2020) examined the REV behavior in sand packs, sandstones, and carbonates. Costanza et al. (2010) analyzed glass beads and commercial silica sand, Ozelim et al. (2018) used a statistical approach to investigate the REV of glass spheres, sand, and clayey sandstone, and Peng-Fei et al. (2022) looked at numerous sand packs, both consolidated and unconsolidated, as well as sandstone samples with different grain shapes. These findings have

enriched our comprehension of how pore-scale heterogeneities vary among rock types and their connection to the REV. As a rule of thumb for similar pore size distributions, artificial media that lack structural biases due to depositional and diagenetic processes have lower REV estimates compared to natural media, in which carbonates typically exhibit larger REV sizes.

Practically all REV studies in recent years have investigated the REV of imaged porosity, reporting a variety of scales for various samples. Though an inter-study comparison is inadvisable due to dissimilar methodologies, a synthesis of findings illustrates typical scales for materials relevant to flow in porous media. For sand packs these ranged from approximately 0.50 mm (Mostaghimi et al., 2012) to larger than approximately 0.62 mm (Singh et al., 2020) and 1.71 mm (Zhang et al., 2000). Sandstones were ascribed REVs of approximately 0.43 mm (Mostaghimi et al., 2012), 1.1 mm (Singh et al., 2020), and 1.2 mm (Okabe & Oseto, 2006). REV values for permeability have been investigated in relatively fewer studies but are usually reported to be larger than those for porosity.

Referring to most of the same studies, Mostaghimi et al. (2012) estimated a REV of approximately 1.1 mm for sand packs and approximately 0.8 mm for sandstones, while Singh et al. (2020) found a REV of approximately 1.04 mm for sand packs. For carbonates with higher heterogeneity, REV values upwards of approximately 2.64 mm have been reported (Singh et al., 2020). Anisotropy has also been found to be an important factor in determining REV for tensorial properties. Thus, the estimation of the REV for porosity alone is inadequate to tolerably capture the variability in permeability. Moreover, Al Raoush & Papadopoulos (2010) demonstrated that the REV of other static properties, such as pore size distribution and coordination should not be determined based solely on the REV for porosity either, observing that the REV for pore size distribution was 2-3 larger than for porosity.

In contrast to the extensive body of research on porosity and permeability, investigations into the REVs of connectivity measures are scanter. Among the few studies investigating REVs of percolation quantities, Biswal et al. (1998) and Keller et al. (2013) utilized local porosity theory to estimate the REVs of percolation probability and percolation threshold. Borges et al. (2017) found that for soil samples the REV of tortuosity is higher than that of porosity. Wu et al. (2018) found the tortuosity REV up to 15 times larger than for porosity. Additionally, they reported that the Euler characteristic exhibited no trend towards an acceptable convergence, which is consistent with reports of very large REVs for this property (Peng-Fei et al., 2020; Vogel, 2002). Al-Raoush & Papadopoulos (2010) calculated the REV for the pore coordination number of sand packs and reported smaller scales for poorly graded packs.

At a conceptual level, the REVs of most properties depend on the separation distances between pore-scale features, which can be best quantified by grain-size distributions. Peng-Fei et al.

(2022) observed that property REVs become gradually smaller with decreasing grain size in otherwise identical sand packs. Notably, positive linear correlations were found between porosity REVs and grain diameters in several studies (Wang et al., 2013; Costanza-Robinson et al., 2011; Rahman et al., 2020). Even in cases where the pore size distribution in a medium appears to be uniform, the presence of large pores can lead to comparatively large REVs. A widely used strategy is to normalize the REV scales by a characteristic dimension of the grains or pores, typically the average diameter (Constanza-Robinson et al., 2010).

Peng-Fei et al. (2022) furthermore noted that wider distributions lead to larger heterogeneity scales for all the static properties that were investigated, a result consistent with the findings of Koestel et al. (2020) who observed a decreasing REV range for soil samples that had their pore distributions narrowed. One way to quantify the broadness of pore size distributions is to use a shape parameter such as the coefficient of uniformity. Studies have shown a positive relationship between the uniformity coefficient and the scaled porosity REV, as reported by Constanza-Robinson et al. (2010), and smaller REVs in well-grade systems, as observed by Al-Raoush & Papadopoulos (2010). This is explained by the fact that broadening a pore-size distribution results in increased heterogeneity in separation distances, thereby requiring a larger averaging scale.

Chapter 3

Methodology

3.1 Workflow

The workflow diagram in Figure 2 illustrates the methodological framework employed in this thesis to comprehensively evaluate the pore-to-Darcy upscaling footprint through a detailed structural characterization and statistical sampling analysis. It captures the steps undertaken from pore network generation to numerical simulations, focusing on the key aim of conducting a multi-property Representative Elementary Volume (REV) analysis.

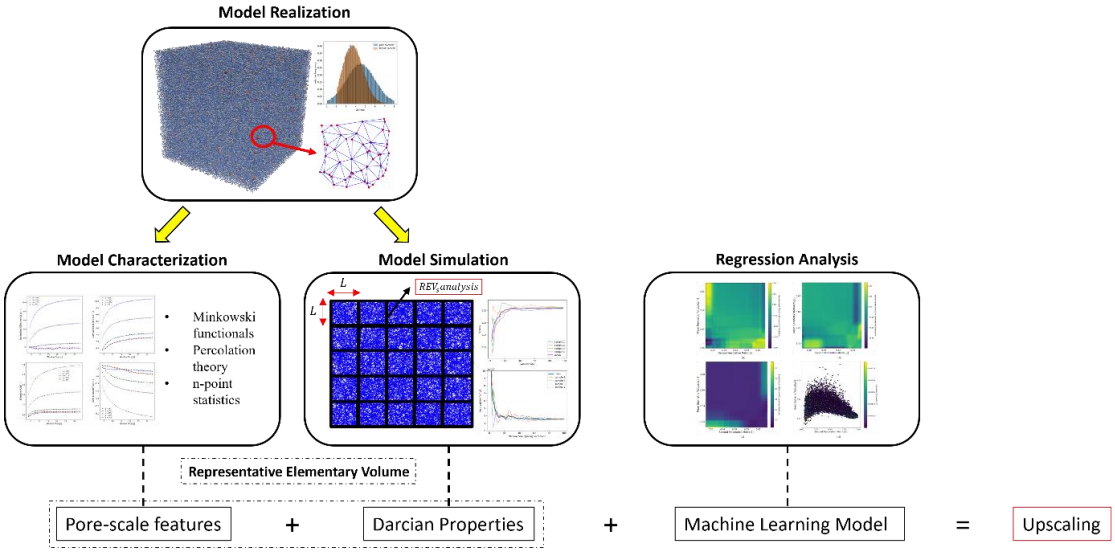

Figure 2 – Visual depiction of the stages of the framework, beginning with network model generation and statistical sampling. The central part of the workflow involves dynamic simulations for computing continuum flow properties and investigating scaling behaviors across multiple properties. The final stages encompass a machine learning analysis to discern the impact of pore-scale heterogeneities on macroscopic flow behaviors, completing the framework for a thorough multiscale upscaling study.

The workflow visually outlines the multi-stage process implemented to explore the upscaling footprint of pore-scale heterogeneities within porous media. The process begins with the generation of idealized pore network models using Delaunay triangulation. This geometric partitioning method is specifically chosen to construct networks devoid of macroscopic heterogeneities, ensuring the study focuses solely on isotropic pore-scale variations in terms of size and connectivity. Such a controlled setup allows for a precise exploration of scaling behavior within a homogeneous dataset, setting a benchmark for comparison against more complex heterogeneities encountered in natural systems. A sampling method is employed to assess spatial variability, and heterogeneity impacts on flow properties. These analyses are necessary for understanding the scaling behaviors of different properties and leveraging data-driven techniques to predict the influence of pore-scale characteristics on continuum-scale behavior.

3.1.1 Network Generation and Sampling

A reference pore network model is systematically constructed through the probabilistic technique of Delaunay triangulation. Base nodes, representing pore centres emerge as randomly assigned points within the network domain. By applying Delaunay tessellation – a geometric partitioning algorithm - the base points interconnect while adhering to the Delaunay criterion, forming a set of distinct non-overlapping simplices. The shared edges and vertices of these simplices, representing throats and pores respectively, can be ascribed relevant attributes like radii and occupation probabilities, that describe the physical properties of the network. Delaunay triangulation acts as a stochastic process that generates a homogeneous and isotropic network, while also providing control over the inherent variability in pore-scale properties. This approach enables the study of a more random network in comparison to a regular lattice characterized by a predefined connectivity. With a composition of one million pores, the resultant network model is populated probabilistically in the absence of macroscopic heterogeneities. This prerequisite is crucial for accurately determining REVs purely based on pore-scale inhomogeneities. Furthermore, because connectivity metrics utilized in this work involve probabilities, their interpretation is relatively straightforward for a random pore network model with a stochastic and stationary structure. It is important to note that given the nature of this upscaling study and the normalization of results, the specific choice of units is inconsequential to the analysis and can be adapted to convenience without affecting the results or conclusions drawn therefrom. Therefore, all lengths are expressed in units of a characteristic length scale of 1. The reference pore network is then a $100 \times 100 \times 100$ unit cube.

The following sampling procedure is employed to conduct a comprehensive sREV analysis into the representativeness of properties across different scales on a cubic pore network model. This

method involves systematically partitioning the pore network into equal-sized cubic sub-volumes and is a special case of the moving window approach that overcomes the limitation of an overlapping sub-volume arrangement. The known edge length of the parent pore network model is L_{edge} in all cardinal directions. For a chosen investigation scale l_{scale} from a range considered in the analysis, the maximal number of non-overlapping cubic sub-volumes that can fit within the parent network is given by

$$n_{sub} = floor\left(\frac{L_{edge}}{l_{scale}}\right)^{d} \tag{11}$$

where d is the network dimension. A more general formulation for an arbitrary sub-volume aspect ratio and moving step is given in Mu et al. (2016). Subsequently, the parent network is partitioned into n_{sub} sub-volumes under the constraint that coterminous sub-volumes must share common boundary faces. Within each sub-volume, the quantities of interest are evaluated, both pore-scale descriptors and continuum properties. Statistical analysis techniques are then applied to assess the heterogeneity of these properties across the sampled network domain. l_{scale} as the designated scale parameter for sub-volume sizing is incrementally increased to explore the effect of scale on the upscaling response. Half L_{edge} represents the scale beyond which sub-volumes would overlap. The analysis is conducted for an ensemble of sub-volumes in the range of 3 to 33 scale units, covering more than three orders of magnitude in investigation volume. As shown in Table 1, total n_{sub} for each scale represents the maximum number of sub-windows available, while active n_{sub} indicates the actual number of sub-volumes used in the analysis for static and dynamic properties. For scales 3 to 6, a representative sample of 4096 randomly selected sub-volumes is used to reduce computational load while maintaining acceptable standard error. It is important to acknowledge that due to the constraint of non-overlapping sub-volumes and equal sizes, there may be portions of the parent network that cannot accommodate a sub-volume. These uncovered portions are excluded from the statistical analysis. The location of each active sub-volume is determined randomly such that the borders of the partitioned network model are never violated. Each sub-volume is severed from the parent network so that it is self-contained, and fluxes are non-existent outside of the sub-volume. Boundary conditions are prescribed to the boundary pores in the plane perpendicular to the flow direction. The solid phase is considered impermeable. Pore-scale models that define the hydraulic and diffusive tortuosity of pore-throat sets are evaluated for an artificial fluid which percolates through the pore network. The estimation of permeability and diffusion coefficient is then done through a system of linear equations. Based on the pressure and concentration solutions, the permeability and diffusion coefficient can be determined by means of Darcy's Law and Fick's Law.

Table 1 – Sampling specifications of the subdivision of the network in terms of the total number of windows, the active number of windows included in the analysis for each investigation scale, and the percentage of the total volume covered by the discretization.

Investigation scale l_{scale}	Total n_{sub}	Active n_{sub} for analysis	Volume covered
3	35937	4096	97%
4	15625	4096	100%
5	8000	4096	100%
6	4096	4096	88%
7	2744	2744	94%
8	1728	1728	88%
9	1331	1331	97%
10	1000	1000	100%
11	729	729	97%
12	512	512	88%
13	343	343	75%
14	343	343	94%
15	216	216	73%
16	216	216	88%
17	125	125	61%
18	125	125	73%
19	125	125	85%
20	125	125	100%
21	64	64	59%
22	64	64	68%
23	64	64	77%
24	64	64	88%
25	64	64	100%
26	27	27	47%
27	27	27	53%
28	27	27	59%
29	27	27	65%
30	27	27	72%
31	27	27	80%
32	27	27	88%
33	27	27	97%

To comprehensively assess the upscaling footprint, a dual-pronged approach is undertaken, involving variations in both pore size distribution and pore coordination number within the reference pore network model, systematically increasing the pore-scale heterogeneity in terms of both size and connectivity.

The exploration of pore size distributions is initiated through a sensitivity analysis. Initially, each pore's maximal diameter is calculated as the largest diameter assignable without overlapping with neighboring features. Then, a random variable U is introduced, representing the multiplier applied to each pore's maximal diameter. U follows a continuous uniform distribution over the interval $[a, 1.0]$

$$U \sim Uniform(a, 1.0) \tag{12}$$

By incrementally decreasing the lower limit a of the uniform distribution, the resulting pore size distributions exhibit greater variability, resulting in a sequence of progressively more heterogeneous networks with equivalent topologies. A uniformity coefficient is calculated for the series of networks to parametrize the degree of pore size heterogeneity within a distribution. The coefficient captures the spread of the distribution in relation to its central value

$$UC = \frac{p_{90} - p_{10}}{p_{50}} \tag{13}$$

where p_{90}, p_{10}, and p_{50} are the 90^{th}, 10^{th}, and 50^{th} percentile, respectively. The uniformity coefficient serves as a more apt variable for subsequent analysis of how changes in the pore size distribution affect continuum phenomena.

The investigation into the influence of connectivity on the upscaling footprint consists of varying the occupation probability p for a given pore size distribution. p represents the likelihood of each throat in the network being active, thereby probabilistically determining which throats serve as conducting pathways. This describes the network's topology through its active throat connections. Networks are generated for occupation probabilities within the range $p_c \leq p \leq 1.0$, with the aim of isolating the upscaling effect rooted exclusively in connectivity on continuum behavior. p_c is the percolation threshold and is found by iteratively eroding the connectivity until the network-wide connection is lost. It was found that $p_c = 8.6032\%$. Connection quantification in this study incorporates the pore coordination number, the Euler characteristic, geometric and diffusive tortuosity, and metrics from percolation theory.

In summation, this methodology generates two sets of pore network realizations across the two variables under scrutiny: pore size and connectivity. By evaluating heterogeneity within sub-volumes at various investigation scales, insights are gained into how these properties change as the scale increases. The analysis provides information about the REV at different scales. The

method of statistical REV analysis on cubic pore network models offers a structured approach to assessing the impact of pore-scale heterogeneities on continuum properties across scales. By systematically analyzing nonoverlapping sub-volumes and evaluating properties within them, this method aids in characterizing porous media and supports the process of upscaling for a wide range of applications.

3.2 Pore-scale Characterization

3.2.1 Minkowski Functionals

3.2.1.1 Volume

The volumetric properties are quantified by computing the volumes corresponding to the bulk window, total pore space, and effective pore space within the network models. Specifically, the bulk volume (V_{sub}) is the volume of the cubic subwindow, the total pore volume (V_{tot}) the sum of non-overlapping pore and throat volumes comprising the network, and the refined effective pore volume (V_{eff}) consists only of the interconnected regions that contribute to flow.

From these volumetric measurements, two types of porosity ϕ are computed as derived quantities, defined by the ratio of the respective pore volume to the investigated window volume

$$\phi_{tot} = \frac{V_{tot}}{V_{sub}} \tag{14}$$

and

$$\phi_{eff} = \frac{V_{eff}}{V_{sub}} \tag{15}$$

Surface Area

Similarly, computation of total surface area A_{tot} and effective surface area A_{eff} provides a detailed measure of the interfacial characteristics. The specific surface areas are then derived by normalizing the surface areas by the corresponding pore volumes

$$\psi_{tot} = \frac{A_{tot}}{V_{sub}} \tag{16}$$

and

$$\psi_{eff} = \frac{A_{eff}}{V_{eff}} \tag{17}$$

3.2.1.2 reflecting the surface area available per unit volume of pore space. Euler Characteristic

In this thesis, the Euler characteristic χ is used to describe the connectivity properties of network models. According to Mecke and Stoyan (2001), the specific connectivity number for a stationary random network is given by

$$\chi = \lambda_0 - \lambda_1 \tag{19}$$

where λ_0 is the vertex intensity and λ_1 is the edge intensity, representing the total number of pore centers and throat connections per unit volume, respectively. These intensities are measured directly from the network structure and describe the connectivity in a density format that provides a scalable measure applicable to various sizes (Peng-Fei et al., 2022).

3.2.2 Geometric Tortuosity

The geometric tortuosity is calculated using Dijkstra's shortest path algorithm (Dijkstra, 1959). The application of Dijkstra's algorithm requires the identification of boundary pores located on opposing faces of a designated sub-volume of a pore network model. Establishing the most direct path between two boundary pores is done by minimizing the sum of straight-line distances between connected pores on the same cluster. A boundary pore is chosen at random and paired with a boundary pore chosen at random from the opposing face. Naturally, the geometric mean is defined only if both pores belong to the same cluster. Let $A = \{P_1, P_2, \dots, P_n\}$ and $B = \{Q_1, Q_2, \dots, Q_m\}$ be the two sets of boundary pores making up opposite faces of a sub-volume. The set of two-pore combinations is given by the Cartesian product of sets A and B

$$A \times B = \{(a, b) \mid a \in A, b \in B, |(a, b)| \leq 4000\} \tag{20}$$

(a, b) represents an ordered pair where a is a boundary pore from A and b is a boundary pore from B, representing the endpoints of the shortest path to be found. Subsequently, the shortest path between the selected pores is found by accounting for the intervening interior pores. The geometric tortuosity is then defined as the ratio between the shortest path and the boundary-to-boundary straight line

$$\tau_{geometric} = \frac{L_{path}}{L_{straight}} \tag{21}$$

To obtain a statistical description of the path distributions, the computation is performed across several boundary pore combinations. However, the number of combinations considered is limited to a maximum of 4000 for the analysis of a manageable set of unique pathways. Geometric tortuosity provides insights into the topological complexity of a porous medium.

3.2.3 Percolation Metrics

Two connectivity metrics based on the size of pore clusters are used: (1) the proportion of the pore volume contained in the largest cluster, and (2) the probability that two randomly chosen pores are connected within the investigation window. In this work, they are referred as the first and second percolation metrics, respectively.

3.2.4 Autocorrelation Function

The two-point correlation point is calculated by allocating line segments of correlation length r to the pore network and recording the fraction of times both endpoints of the segments fall in the pore space. The calculation is repeated for a succession of correlation lengths and the resulting function quantifies the probability of encountering two points within a given distance r of each other, both residing within the pore space. Because the set of pore network models investigated possess no directional bias, the correlation function depends on the magnitude of the correlation length r alone. An indicator function $I(\boldsymbol{x_i})$ is assigned to each point $\boldsymbol{x_i}$ and assumes a value of unity when $\boldsymbol{x_i}$ falls within the pore space and assumes a value of zero otherwise

$$I(\boldsymbol{x_i}) = \begin{cases} 1 \; if \; \boldsymbol{x_i} \in V_{pore} \\ 0 \; if \; \boldsymbol{x_i} \notin V_{pore} \end{cases} \tag{22}$$

The correlation function $\xi(r)$ for a given distribution of point pairs is then approximated as

$$\xi(r) = \frac{1}{M} \sum_{k=1}^{M} \prod_{i=1}^{n} I_k(\boldsymbol{x_i}) \tag{23}$$

where n equals 2 for two-point statistics and $M$is the total number of point pairs analysed for each length r in the investigated correlation range. Adding an additional condition that both endpoints must fall within the same cluster modifies the autocorrelation function to consider only the spatial correlation of the effective pore space. In this case, the correlation function is referred to as the cluster correlation function $\xi_c(r)$ and gives information on the spatial arrangement of connected clusters. The integrals of the autocorrelation functions, L_ξ and L_{ξ_c}, are a characteristic correlation scale of the microstructure and are used to quantify heterogeneity in the correlation functions

$$L_\xi = \int_0^r \xi(r), \qquad L_{\xi_c} = \int_0^r \xi_c(r) \tag{24}$$

Lastly, the lineal path function ξ_l is calculated concurrently and conveys the probability that the entire line segment of length r is accommodated within the pore space. The lineal path

function describes statistically the ability of the pore network model to facilitate flow along linear flow paths.

The proposed method for calculating the three correlation functions uses a distance-based criterion in conjunction with the geometric relationship of a point relative to neighboring pore elements. Barycentric coordinates enable precise evaluation of the indicator function based on the position of a point within a simplex anchored at the endpoints of a throat. Point coordinates are thus represented as a linear combination of throat vertices. The process starts with retrieving the locations and dimensions of all pores and throats in the immediate vicinity of a randomly placed point $\boldsymbol{p}_i$. To facilitate rapid data retrieval, a KD-tree algorithm (Cormen et al., 1990) is used to partition the network in terms of its pores; the search radius is taken as the length of the longest throat in the network. Firstly, the algorithm calculates the distance map of point $\boldsymbol{p}_i$ directed towards the centres of the indexed pores as a check for whether $\boldsymbol{p}_i$ resides within a pore. If the Euclidean distance to a nearby pore centre $\boldsymbol{P}_i$ is less than or equal to the radius of that pore

$$dist(\boldsymbol{p}_i, \boldsymbol{P}_i) \leq d_i \tag{25}$$

$\boldsymbol{p}_i$ is deemed to be situated in the pore space, and the corresponding indicator function is assigned. If none of the distances satisfies this condition, the algorithm checks for the point's inclusion within an indexed throat by calculating the Plücker coordinates of each throat. As an example, a throat is considered that connects two indexed pores, $\boldsymbol{p}_a$ and $\boldsymbol{p}_b$. Plücker coordinates are a representation of lines in $3D$ space and facilitate efficient line-line intersection tests. They consist of the line segment which encodes the direction of the throat

$$\boldsymbol{d} = \boldsymbol{p}_a - \boldsymbol{p}_b \tag{26}$$

and the moment vector, which encodes the position of the throat relative to the origin

$$\boldsymbol{m} = \boldsymbol{p}_a \times \boldsymbol{p}_b \tag{27}$$

$\boldsymbol{p}_i$ is then projected onto $\boldsymbol{d}$ to find $\boldsymbol{p}_i{}'$

$$\boldsymbol{p}_i{}' = \boldsymbol{p}_i + \frac{\boldsymbol{d} \times (\boldsymbol{m} + \boldsymbol{d} \times \boldsymbol{p}_i)}{\|\boldsymbol{d}\|^2} \tag{28}$$

wherefrom the local barycentric coordinates can be defined as

$$\boldsymbol{p}_i{}' = \omega_a \boldsymbol{p}_a + \omega_b \boldsymbol{p}_b \tag{29}$$

If the coefficients satisfy the endpoint condition of non-negativity and unity summation

$$0 \leq \omega_a \leq 1 \; and \; 0 \leq \omega_a \leq 1 \tag{30}$$

the point $\boldsymbol{p}_i$ lies between the point centres $\boldsymbol{p}_a$ and $\boldsymbol{p}_b$. For instance, if $\boldsymbol{p}_i$ is located at the midpoint of $\boldsymbol{d}$, the coefficients would be $(0.5, 0.5)$. Additionally, a distance map is calculated between $\boldsymbol{p}_i$ and $\boldsymbol{d}$. If the distance is smaller than a threshold value R_t that depends on the geometry of the throat

$$\frac{\|\boldsymbol{m} + \boldsymbol{d} \times \boldsymbol{p}_i\|}{\|\boldsymbol{d}\|} \leq R_t \tag{31}$$

and the endpoint condition is simultaneously met, the point is considered part of the pore space, and the corresponding indicator function is assigned. In the case of cylindrical throats, the distance-based criterion simplifies to a check against the throat radius.

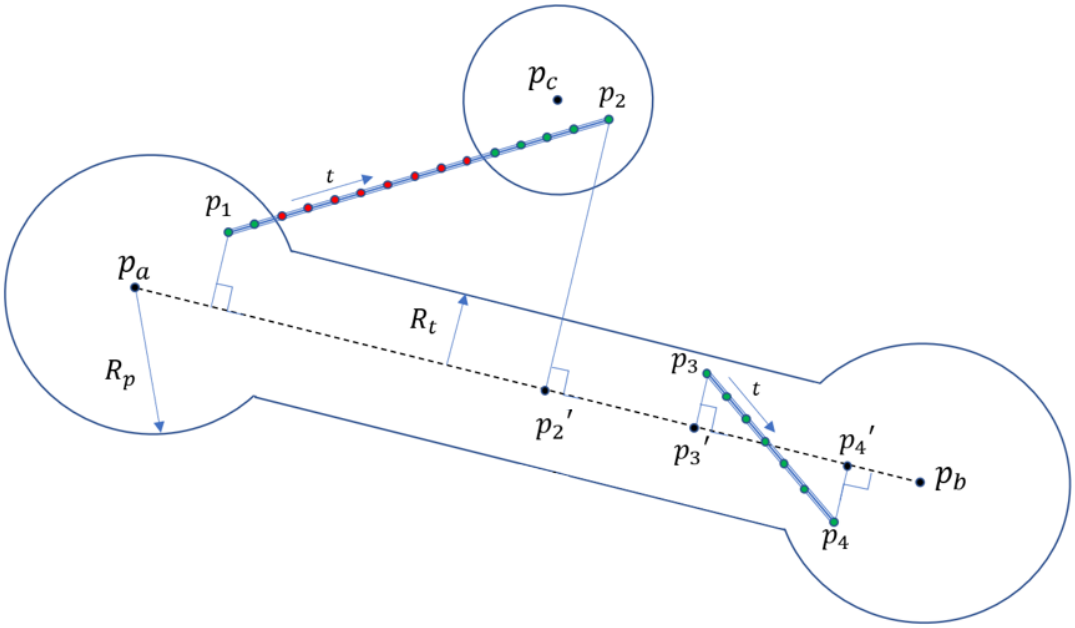

Figure 3: Schematic representation of the method for estimating the spatial correlation of idealized pores and throats in a pore network model.

3.3 Steady-State Simulation

3.3.1 Permeability

Pore network modelling discretizes continuous flow-field variables to a system of point values assigned to pore centers. As conservation relations are applied to each pore, the flow rate through a pore-throat conduit is proportional to the pressure difference between two directly connected pores. Mass conservation for steady-state, incompressible, and non-inertial flow for a Newtonian fluid in the $i-th$ interior pore is described by a linear response

$$q_i = \sum_{j=1}^{n} \frac{G_{ij}}{\mu} \cdot \left(P_j - P_i\right) = 0 \tag{32}$$

where q_i denotes the net volume rate through the $i-th$ pore, j indexes all connected neighbours, n is the pore coordination number of the $i-th$ pore, μ is the fluid viscosity, $P_j - P_i$ is the pressure differential driving the flow, and G_{ij} is the hydraulic size factor of the flow channel spanning the centres of pores i and j. The net volume rate for an incompressible fluid is zero for all except the boundary pores. G_{ij} contains purely geometrical information and is given under Stokes conditions for an arbitrarily shaped channel with cross-section $A(x)$ and length L by (Akbari et al., 2011)

$$G_{ij} = \left[16\pi^2 \int_0^L \frac{I_p}{A(x)^2}\, dx\right]^{-1} \tag{33}$$

where I_p is the polar moment of inertia which captures the distribution of channel space from the centreline. OpenPNM (Gostick et al., 2016) calculates the effective hydraulic size factor for each assembly of two pores R_1 and R_2 connected by a throat R as the length-weighted harmonic average along the pore centre-to-centre conduit length

$$\frac{1}{G_{12}} = \frac{1}{G_1} + \frac{1}{G_t} + \frac{1}{G_2} \tag{34}$$

Elements G_1 and G_2 are associated with each respective pore and G_t corresponds to the throat. The total conduit length for the series connection is

$$L_t = L_i + L_k + l_{ik} \tag{35}$$

where L_i and L_k are the centre-to-throat distances of R_i and R_k, respectively, and l_{ik} is the throat length, as depicted in Figure 4 below. For a cylindrical conduit, the expression above reduces to the Hagen-Poiseuille equation for a cylindrical channel

$$G_1 = \frac{\pi {d_i}^4}{128 L_i}, \qquad G_t = \frac{\pi {d_{ik}}^4}{128 l_{ik}}, \qquad G_2 = \frac{\pi {d_k}^4}{128 L_k} \tag{36}$$

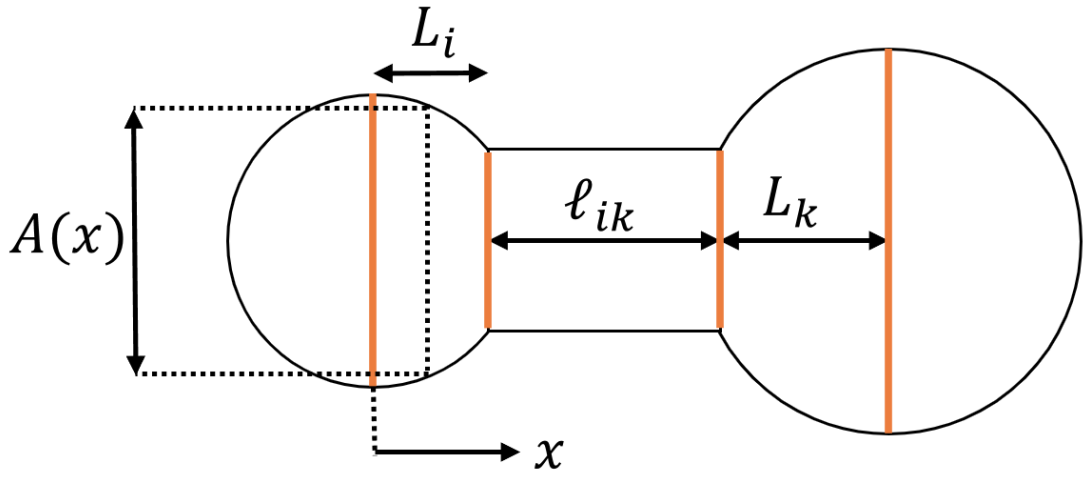

Figure 4: Schematic diagram of a pore pair coupled by a shared throat. Labelled are the effective lengths of each element contributing to the calculation of the effective conductance (Gostick et al., 2016).

Summing over all N pores in the network results in the incompressibility condition

$$Q_i = \sum_{i=1}^{N} \sum_{j=1}^{n} \frac{G_{ij}}{\mu} \cdot (P_j - P_i) = 0 \tag{37}$$

from which we can deduce that the inlet and outlet flow rates at steady state must be equivalent. The resulting system of N linear equations $\boldsymbol{Q} = \boldsymbol{G} \cdot \boldsymbol{P}$ consists of the flow rate vector $\boldsymbol{Q}$ that sums to zero, the pressure vector $\boldsymbol{P}$, and the sparse symmetric conductance matrix $\boldsymbol{G}$. Fixing the pressures at the boundary pores to solve the system for the pressure field permits the calculation of the flow rate $Q_{boundary}$. The permeability is then found through a simple application of Darcy's Law

$$K = \frac{Q_{boundary} \mu L_{network}}{A_{network} \Delta P_{network}} \tag{38}$$

where $L_{network}$, $A_{network}$, and $\Delta P_{network}$ are the Euclidean distance, cross-sectional area, and pressure difference across the network, respectively. This approach can be extended for the continuum prediction of multi-phase properties like relative permeability by using separate conductivity models for each phase (Bultreys et al., 2020).

3.3.2 Diffusion Coefficient

Calculation of the diffusion coefficient follows much the same methodology. Diffusive mass balance in interior pore i states that the mass rate m_i in accordance with Fick's Law is given by

$$m_i = \sum_{j=1}^{n} F_{ij} D \cdot \left(C_j - C_i\right) = 0 \tag{39}$$

where D is the fluid-dependent diffusivity, $(C_j - C_i)$ the concentration difference between pores i and j, and F_{ij} the diffusive size factor. For a series ensemble of two pores and an active throat connection, the overall diffusive size factor is

$$\frac{1}{F_{12}} = \frac{1}{F_1} + \frac{1}{F_t} + \frac{1}{F_2} \tag{40}$$

and for an element with an arbitrary cross-sectional area $A(x)$

$$F = \left[\int_0^L \frac{dx}{A(x)}\right]^{-1} \tag{41}$$

For a cylindrical channel with diameter d, the size factor simplifies to

$$F = \frac{\pi d^2}{4L} \tag{42}$$

In analogy to the pressure solution, the concentration field is solved from a system of linear equations with imposed boundary concentrations

$$M_i = \sum_{i=1}^{N} \sum_{j=1}^{n} F_{ij} D \cdot \left(C_j - C_i\right) = 0 \tag{43}$$

The overall diffusion coefficient follows suit from Fick's Law applied to the entire sample

$$D = \frac{M_{boundary} L_{network}}{A_{network} \Delta C_{network}} \tag{44}$$

with $\Delta C_{network}$ as the concentration difference between the boundaries and $M_{boundary}$ the boundary mass rate.

Chapter 4

Results and Discussion

4.1 Representative Elementary Volume Analysis

Accurately determining Representative Elementary Volumes (REVs) is essential for understanding the scale dependency and spatial variability of macroscopic properties in porous media. Many previous studies have been limited by insufficient sample sizes or too few samples, resulting in sparse data that inadequately captures the true existence and size of REVs. This thesis overcomes these limitations by employing a higher resolution and a broader range of REVs, providing a more robust foundation for understanding these key parameters.

This section systematically examines the scale dependency of spatial variability in a number of properties and quantifies the existence and size of statistical REVs. By utilizing an efficient pore network modelling approach, the study significantly reduces the computational burden associated with REV estimation, making the analysis reliable and reproducible within a reasonable timeframe. This optimized framework balances the need for accuracy with practical constraints, ensuring that the findings are both robust and applicable across different scales.

Figure 5 and Figure 6 present a construction of the coefficient of variation (CoV) for the suite of computed properties as a function of cube window size across different media for pore size uniformity coefficient and occupation probability, respectively. Each data point within this figure represents the CoV for a specific window size, offering a quantified measure of statistical dispersion within potential REVs, with the resulting curves encapsulating the scale-dependent variability inherent in the pore networks. As such, the CoV, calculated as the standard deviation of a property over its mean across sampling sizes, serves as the measure of choice for estimating the sREV, acknowledging that REVs may vary spatially across different locations within the network.

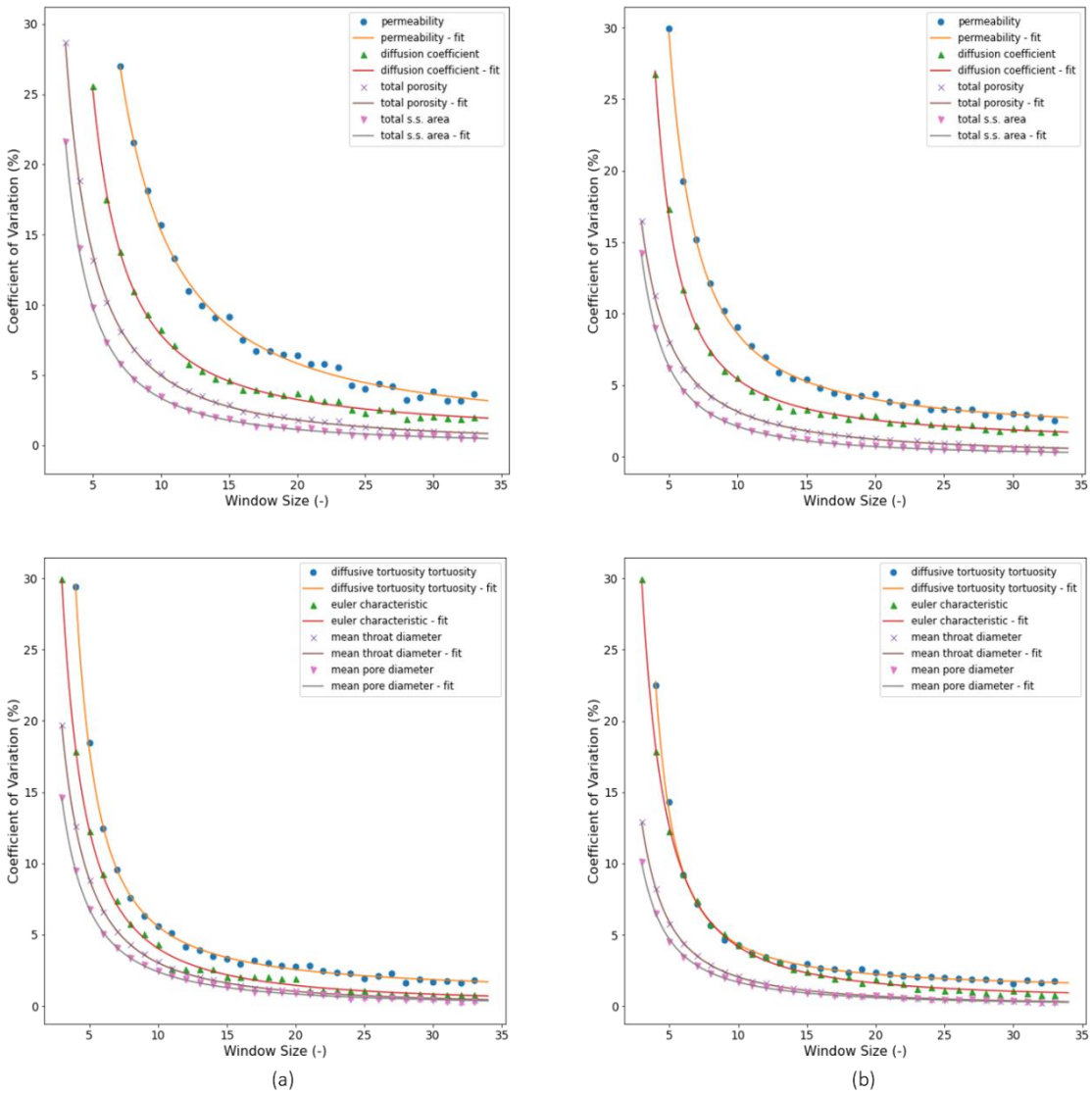

Figure 5: Coefficient of Variation (CoV) for multiple properties at lower limit α of 26% (a) and 76% (b), plotted against window size.

An advantage of using the CoV is that it facilitates direct comparisons due to its unitless nature, making it easier to compare datasets with different means and of different property classes, allowing for a consistent definition of sREV that is solely determined by the chosen error threshold. A lower CoV value indicates a more robust estimation of the REV, as it reduces variability among samples, thereby providing a more precise average REV scale. By using CoV as a global measure, this approach ensures that the resulting sREV is well-defined, avoiding the issue of non-unique REVs (Gerke & Karsanina, 2020). The sREV is thus defined as the scale below which the statistics of the property of interest exhibit statistically significant variability with scale.

Analysis of the CoV form unveils a systematic trend: the CoV declines exponentially with increasing window size; consequently, this decay pattern suggests a homogenization of the

measured properties towards a representative value. Such behavior is in line with the principle that broader sampling mitigates the heterogeneities of the network and aligns with the statistical theory that larger samples tend to approximate the true population average more closely (Kanit et al., 2003). At smaller window sizes, there is noticeable variability across the networks - these fluctuations highlight the significant impact of pore-scale heterogeneity, which are more pronounced at smaller scales. As the window size increases, the spatial variability diminishes, leading to a rapid decrease in variance. This trend indicates that an sREV can theoretically be established when the window size is sufficiently large, such that the CoV becomes diminishingly small. Additionally, the observed variance can act as a qualitative measure of the impact of rock heterogeneity on property-specific upscaling.

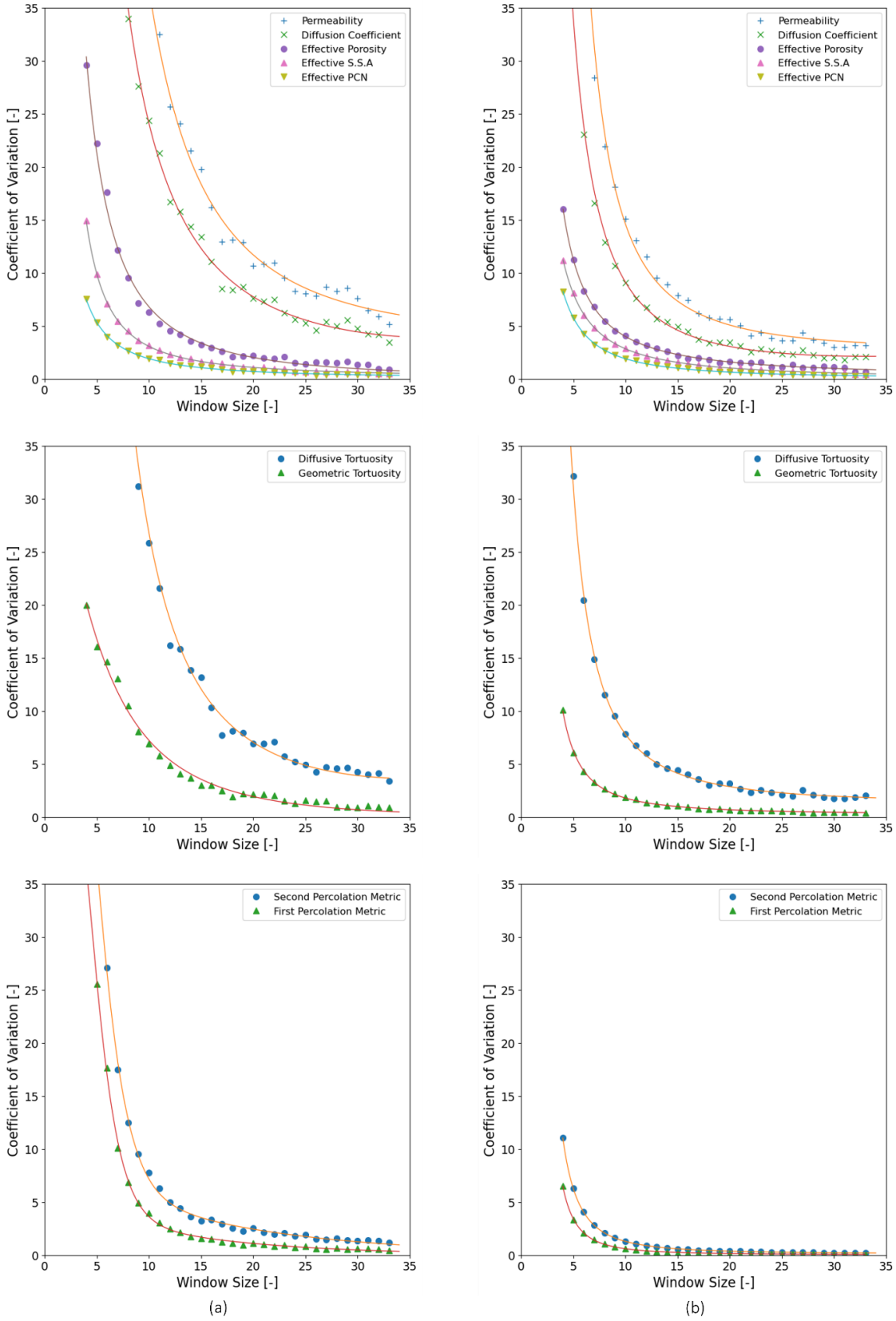

Figure 6: Coefficient of Variation (CoV) for multiple properties at occupation probabilities of 12% (a) and 30% (b), plotted against window size. The graphs represent the CoV for permeability, diffusion coefficient, effective porosity, effective specific surface area (S.S.A), effective pore coordination

number (PCN), diffusive tortuosity, geometric tortuosity, and percolation metrics. The data illustrates the exponential decay of CoV with increasing window size, indicating a trend towards homogenization and representative averaging of properties.

Measurements taken at scales of larger variability are inherently unreliable, as they are influenced by random heterogeneities in pore size and connectivity rather than representing true macroscopic properties. Achieving the sREV ensures that the measured property is stable and unaffected by these random variations, providing a statistically valid representation of the material. As the window sizes grow larger, the properties tend to converge toward homogeneity. This trend was consistently observed for all properties in the analysis, confirming that the sREV can be practically achieved for both static and dynamic properties in the networks examined in this study.

The exponential decrease in the CoV can be understood as a result of averaging over increasingly larger volumes, which progressively incorporate a broader range of heterogeneities. Smaller windows might capture localized features—such as a large pore or a sparse cluster of throats—that can skew property measurements. However, as the window size increases, these local anomalies are averaged out, leading to more representative measurements that reflect the medium's overall characteristics. This reduction in variability is a natural consequence of the system becoming more homogeneous at larger scales.

The dynamic continuum properties registered the highest CoV curves for both pore size and connectivity analyses, reflecting a stronger and more varied response to pore-scale heterogeneities because of the added mechanisms underpinning transport processes: they are influenced by the size, shape, and connectivity of pore elements. A single bottleneck can for instance significantly impede flow, causing high variability in permeability across different samples at no discernible change to the porosity. In the same vein, more tortuous paths can dramatically slow down diffusion though the pore sizes remain unchanged. CoV magnitude can thus directly quantify the extent to which heterogeneities scale a specific aspect of continuum behavior. Nonetheless, the observation of exponential behavior in the CoV for dynamic properties would seem to indicate that structural heterogeneities exert a similar scaling influence on both static attributes and transport mechanisms. The difference in sensitivity between permeability and diffusion coefficient is likely because permeability is a continuum manifestation of not only the pathways available but also on the specifics of viscous flow that impose an additional boundary condition at the fluid-solid interface.

Curve-fitting of an exponential-type relationship to the CoV values of each property was done using a generalized version of the exponential decline function

$$ax^b \cdot e^{-cx^d} \tag{45}$$

to allow for additional flexibility in accommodating the diverse decay rates and conformations present in the dataset. The optimal fit for each property's CoV was determined by minimizing the root mean square error (RMSE) while ensuring that the curve adheres globally to the downward trend. The exponential curves fitted to these points serve not only as descriptive tools but also as predictive models for the network's behavior at REV thresholds beyond the range of the empirical data. In general, smaller decay rates are observed in networks with larger p because more densely connected networks yield a more homogeneous distribution of connectivity. Sparsely connected networks on the other hand reveal greater heterogeneity and, consequently, a higher CoV for a given window size.

Because the rate of convergence to the true population means is inherently exponential, further increases in the spatial scale are met with a diminishing reduction in the error. This suggests that the benefits of increasing the sample size come at a greater computational cost or experimental expediency. An optimal sREV size must, therefore, be chosen judiciously to strike a balance between these competing demands.

sREV estimation can be conducted using various criteria, though the impact of these thresholds on REV identification can be ambiguous because they are based on subjective assessments of acceptable property variability (Constanza-Robinson et al., 2011; Keller et al., 2018; Rahman et al., 2020). In this study, the REV was defined as the minimum window length at which the coefficient of variation (CoV) for the measured property remained below 5%. This threshold ensures that the statistical variability, relative to the mean, is sufficiently small. The 5% criterion is well below thresholds commonly suggested in the literature for homogeneous samples and typically represents reasonable balance between sensitivity and specificity in data analysis. While the choice of this criterion depends on the system and desired accuracy, it offers a reliable standard for ensuring acceptable error across the domain.

However, it is important to note that such criteria are based on subjective assessments of acceptable property variability. To validate the prudence of this threshold, we compared it with visual assessments of plateau regions in the mean data (shown in the following section) and found it to align well with similar literature standards. Thus, the sREV estimated using this method represents the lower bound of a scale range within which property variability is minimal, with the upper bound defined by the linear extent of the domain.

When fitting exponential curves to the CoV values, an initial exponential decay ae^{-bx} is observed, followed by a shift to a sub-exponential rate at larger scales (Figure 7). This transition reflects that, beyond a certain point, the decrease in variability is no longer due to averaging out pore-scale heterogeneities, but rather because the system approaches an inherent limit of error reduction. As window sizes increase, the CoV decline slows, indicating that the variability

is reaching a minimal threshold determined by the fundamental measurement limits rather than structural heterogeneities. The 5% CoV threshold captures this shift effectively, marking a scale well beyond the point where the reduction in statistical error offers diminishing returns. This threshold represents a balance between sensitivity and specificity, ensuring that the window size encompasses a statistically adequate range of features. Thus, the choice of this threshold is crucial for defining the REV, accounting for both the inherent error limits of the measurement and the need for representativity across different scales.

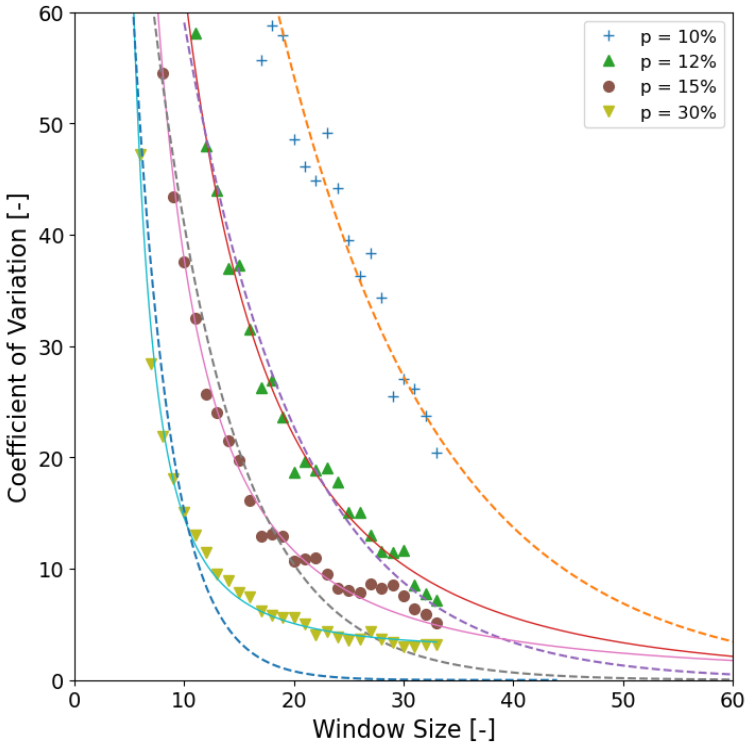

Figure 7: Permeability CoV values for different values of the occupation probability, plotted along with the best-fit curves as well as dashed lines representing the exponential function. Notably, at a 10% occupation probability, closely adjacent to the percolation threshold, the exponential model remains the closest fit, potentially because the window sizes have not yet reached the scale where the CoV's decline rate would noticeably slow down.

Figure 8, capturing the CoV at an occupation probability of 9%, near the percolation threshold, reveals a breakdown of scaling behavior where no singular scale can confidently yield representative continuum behavior. The CoV curves for dynamic properties exhibit significant variability that does not conform to recognizable exponential decay, which challenges the determination of an accurate REV. In contrast, the specific surface area (SSA) demonstrates a more consistent exponential decay, suggesting that as a static property, it remains less perturbed by connectivity fluctuations that heavily influence dynamic mechanisms as a network nears the threshold. The total porosity presents relatively more stability compared to effective porosity,

pointing to the impact of connectivity on effective transport pathways. Notably, both the geometric tortuosity and the second percolation metric exhibit a near-constant CoV. This plateau may suggest that these properties are less sensitive to the scale at which they are measured in highly fragmented systems. The absence of a stabilizing CoV illustrates the difficulties of upscaling in networks where traditional concepts of structure become erratic and non-representative of bulk behavior. This instability precludes the determination of a reliable REV, and as such, the results at $p = 9\%$ are omitted from further consideration. Lastly, the fluctuations in the Euler characteristic draw attention to a drawback of the Coefficient of Variation as a metric; in networks with poor connectivity, the mean Euler characteristic undergoes a sign change with increasing window size. This transition from positive to negative values results in an inflated CoV.

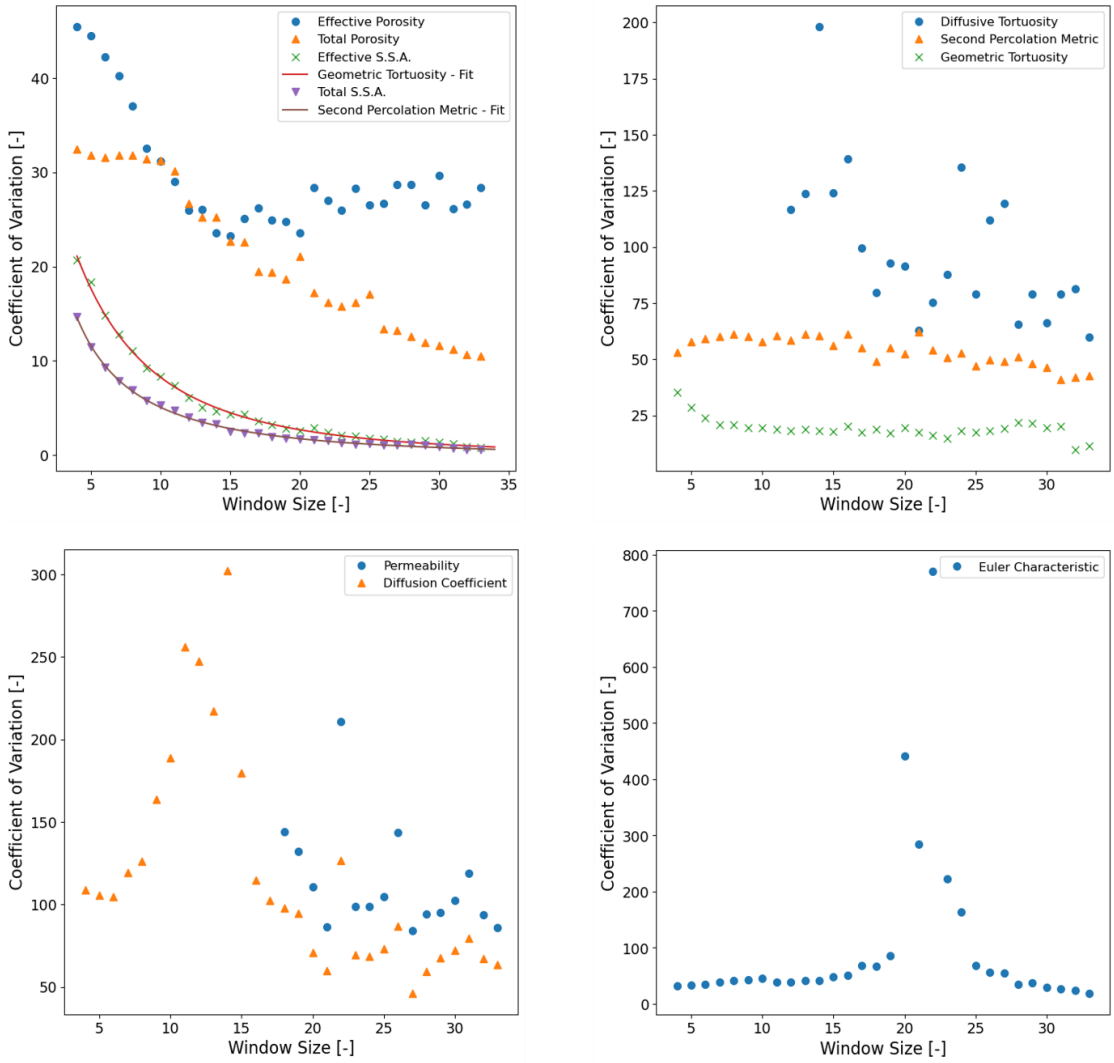

Figure 8: Coefficient of Variation (CoV) for multiple properties at a 9% occupation probability, depicting the challenge of defining a Representative Elementary Volume (REV) near the percolation

threshold. These curves collectively underscore the complexities in networks below the correlation length.

The analysis of the representative elementary volumes (REVs) presented in Figure 9 reveals a critical transition at approximately 30% connection probability, beyond which a power-law relationship emerges. This shift aligns with the onset of clustering within the network and mirrors the behavior of the correlation length near the percolation threshold. As the connection probability decreases toward this threshold, the correlation length diverges, leading to increasingly larger scales over which network properties must be averaged to achieve representativity. Below the clustering onset, the network's inherent redundancy of pathways preserves connectivity despite throat removals, maintaining relatively stable REV values that do not exhibit significant fractal influence.

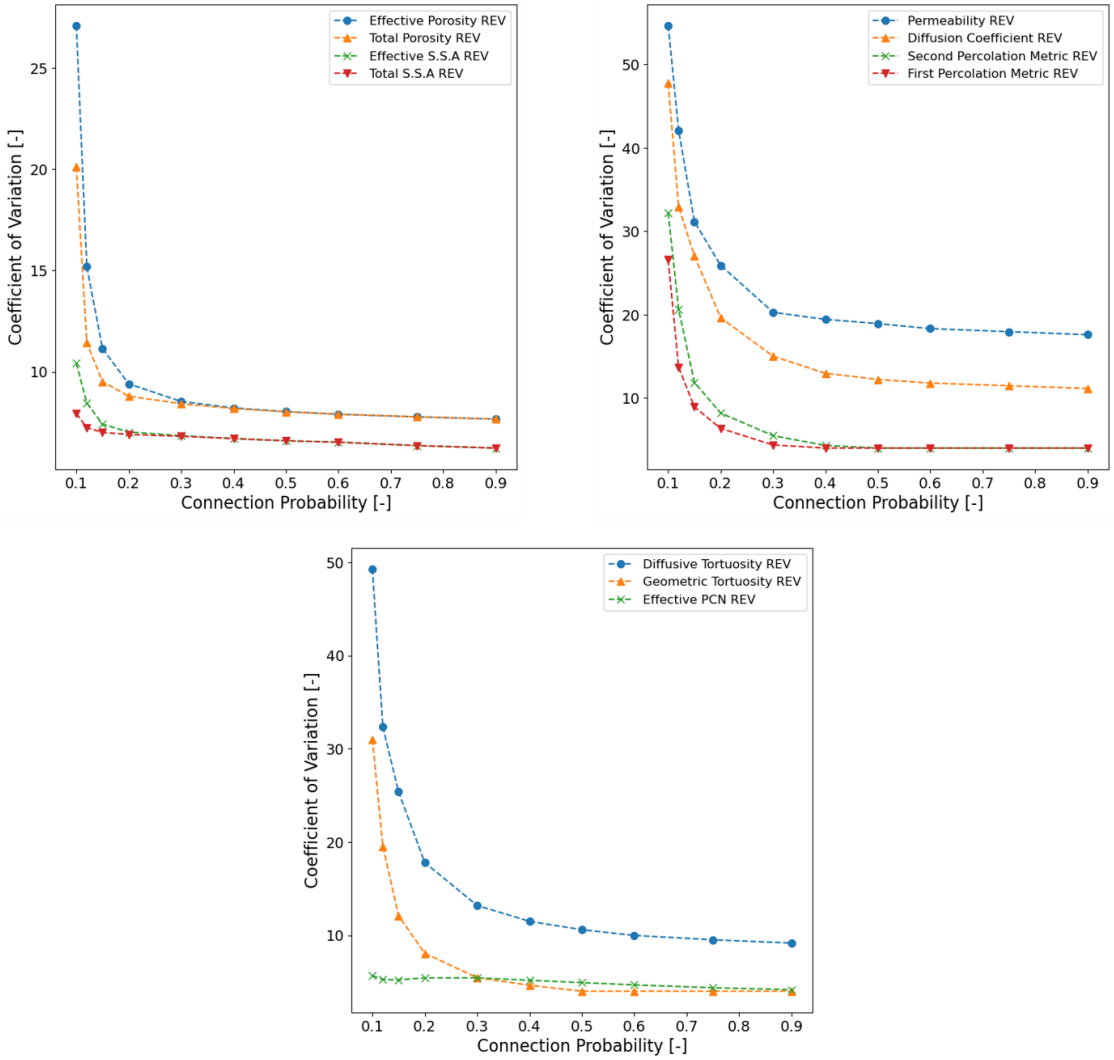

Figure 9: Variation in the Coefficient of Variation (CoV) for key properties against occupation probability (p), illustrating the critical transition in network clustering at p=30%. The graphs capture the REV for effective and total porosity and specific surface area (S.S.A), permeability, diffusion

coefficient, percolation metrics, and different tortuosity measures, each exhibiting a distinct power-law rise beyond p=30%.

In other words, the redundancy of pathways ensures a negligible effect on the correlation length, which translates to a comparatively insensitive representativity. A relationship between the correlation length and REV is expected because both are measures of scale: the correlation length describes the extent of fractal influence within the network, while the REV defines the scale at which the network's properties become statistically representative of the whole.

The correlation length basically bifurcates the network into two domains: below this critical scale, the network exhibits fractal characteristics. As percolation theory suggests, near the percolation threshold, universal aspects dominate, and the fractal nature of clusters introduces a strong dependence of transport properties on network connectivity. The CoV curves for permeability, presented in Figure 10, illustrate the interplay between REV and the correlation length. For occupation probabilities of 15%, 12%, and 10%, we observe that the CoV decreases in a non-monotonic and erratic fashion at smaller window sizes, indicating that no single window size within this range can effectively capture the network's heterogeneity. This fractal nature arises due to being below the correlation length scale. Within this regime, the network retains complex, approximately self-similar patterns that defy averaging. The expected exponential decay in CoV, which would suggest the approach of a stable REV, is only observed once the analysis transcends the bounds of the correlation length. For the networks under consideration, this transition to exponential behavior begins at window sizes of approximately 8, 10, and 17 units for the 15%, 12%, and 10% occupation probabilities, respectively.

In stark contrast, the 9% occupation probability network presents a consistently erratic CoV across all investigated window sizes, implying that the entire window size range falls below the correlation length. Here, the fractal nature characterizes every size examined, prohibiting the identification of a representative REV in a scale-invariant regime. Intuitively, this fractal nature means that the pore space, when sampled below the REV, retains a complexity that does not average out. Above the clustering threshold, however, where the correlation length falls below the smallest window size considered, the system has transitioned away from its fractal character and into a more homogeneous state where REV can be effectively determined. Consequently, the power-law increase in REV predictions as we approach the percolation threshold mirrors the divergence of the correlation length, such that there is a rapidly expanding scale for representativity.

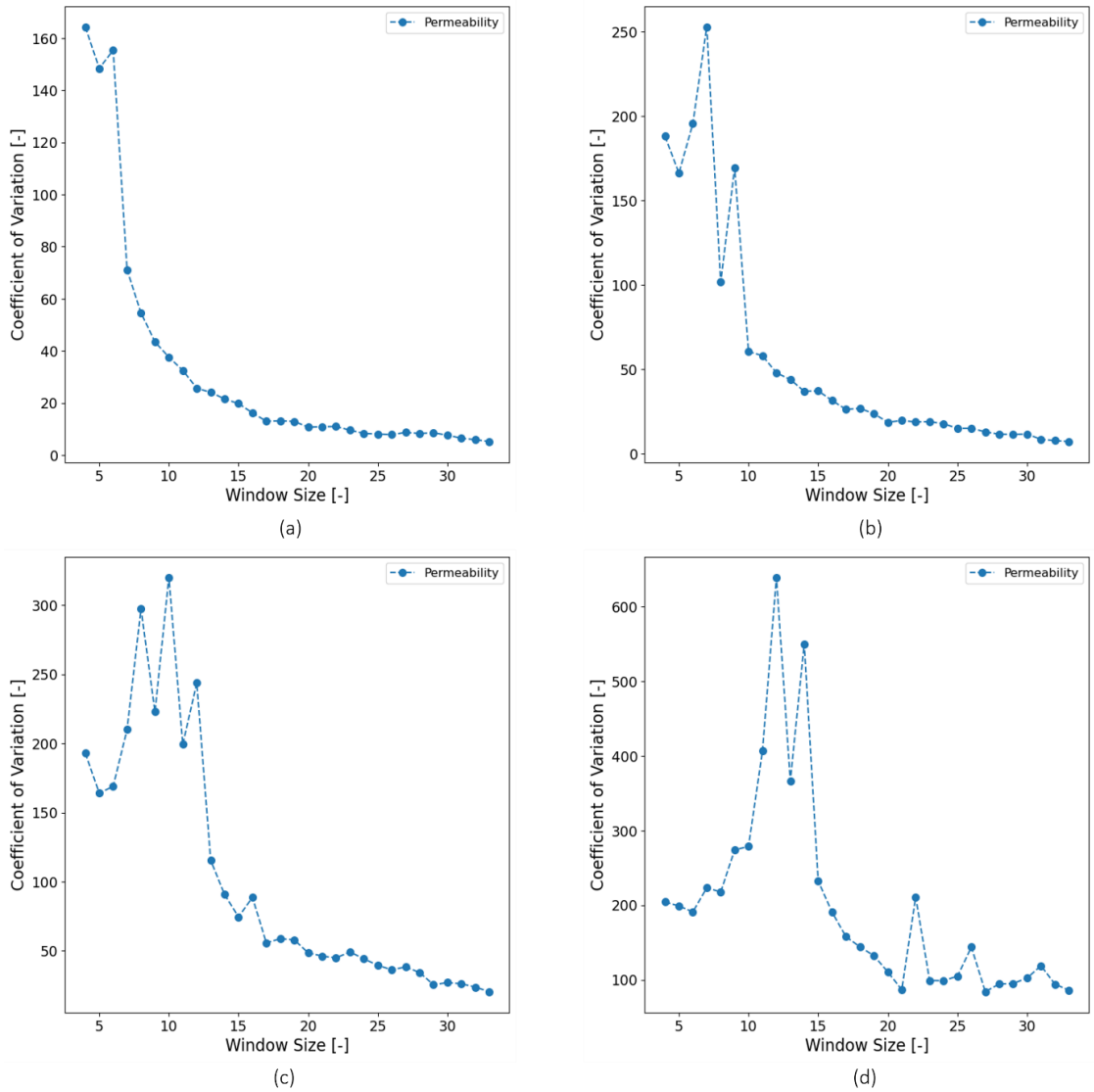

Figure 10: Coefficient of Variation (CoV) for permeability across different occupation probabilities within a network, showcasing the relationship between REV and correlation length. Subfigures (a), (b), (c), and (d) correspond to occupation probabilities of 15%, 12%, 10%, and 9%, respectively.

The graphical representation in Figure 11 offers a comprehensive view of the scale dependency of various properties, showing the requisite investigation sizes to achieve representativity at 5% precision. There is a uniformity in scale representation across the networks, which do not exhibit any clustering (from $p = 90\%$ to $p = 30\%$) and thus, there is minimal change in the functional form of the relationship curve due to the approximately linear variation with connectivity. However, as clustering commences the relationship undergoes a transformation. The hierarchy of property-specific REVs diverges, signifying a shift in how each property's spatial variability responds to the network's heterogeneity.

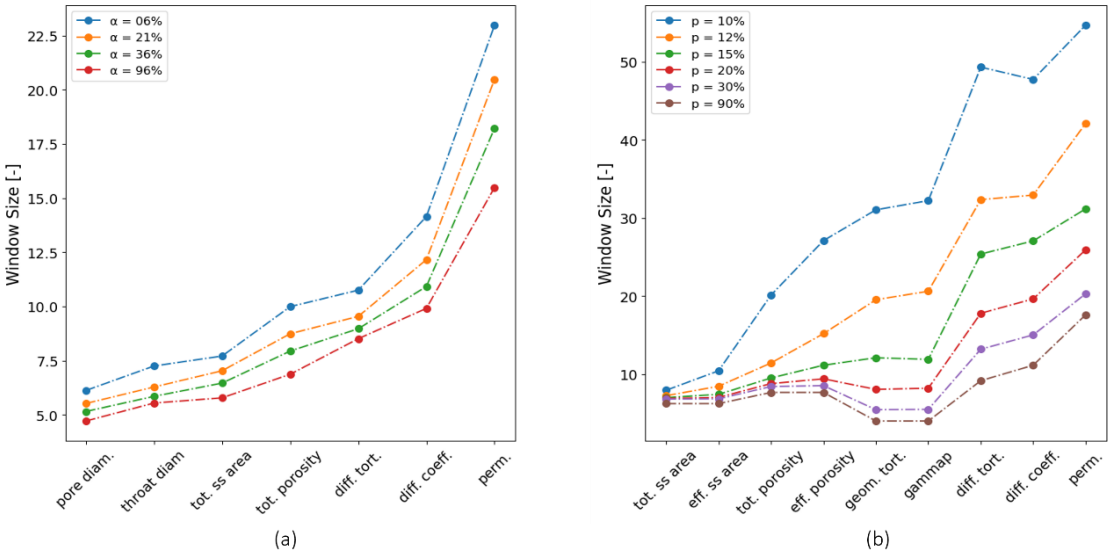

Figure 11: Scale dependence of Representative Elementary Volume (REV) sizes across occupation probability and uniformity coefficient. This graph illustrates the required window sizes to achieve a 5% coefficient of variation (CoV) for different properties within porous networks. The curves exhibit a distinct transition at p=30%, where clustering begins, and demonstrate the varying scale sensitivities of properties.

The analysis of the linear relationships between the predicted 5% CoV threshold REVs and the variables that capture network heterogeneity reveals critical insights into the behavior of porous media under different connectivity and size conditions. Figure 12 and Figure 13 reveal a linear relationship when the predicted 5% CoV threshold is plotted against the uniformity coefficient and mean geometric tortuosity for each network, respectively. The fact that there is a proportional increase in the size of the REV suggests that geometric tortuosity encapsulates the complexity of available flow paths within the network in a manner that scales proportionally with the window size needed to achieve a representative average. This consistency in how it evolves allows geometric tortuosity to serve as an accurate representation of network heterogeneity in the case of the connectivity analysis.

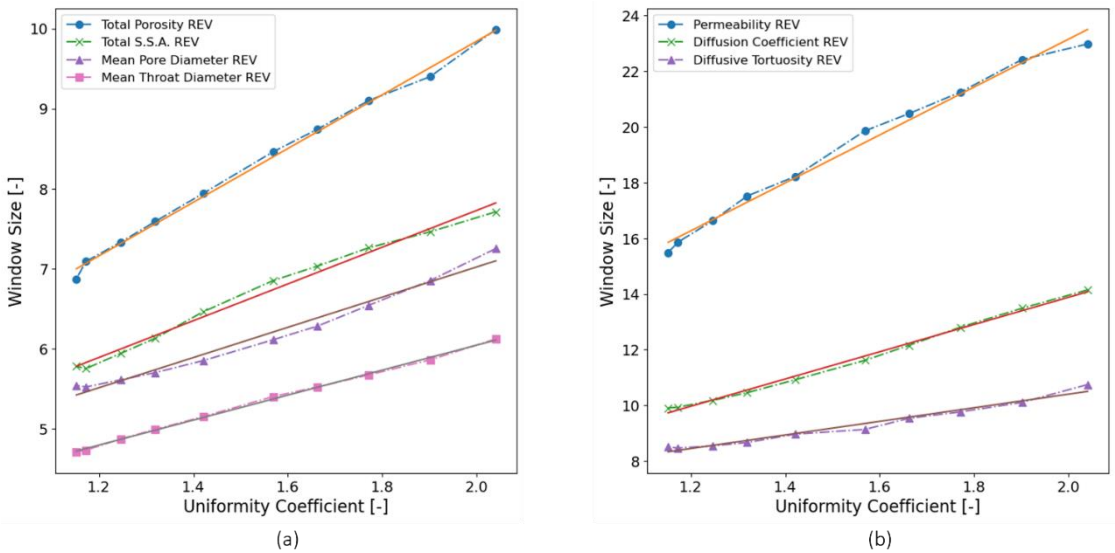

Figure 12: Representative Elementary Volume (REV) size scaling with uniformity coefficient across different rock properties. The top left graph correlates porosity, specific surface area, and sizes. The right graph shows the relationships with permeability, diffusion coefficient, and diffusive tortuosity.

Interestingly, both permeability and diffusion coefficient REVs demonstrate nearly identical slopes for the connectivity analysis. Despite the different physical phenomena governing the effective coefficients, the REVs required to describe both properties seem to be equally influenced by the network's connectivity constraints as captured by the geometric tortuosity. The observed linear trends suggest that geometric tortuosity is a robust predictor of the REV size across different transport mechanisms. In contrast, effective porosity and SSA deviate from the linear trend. Overestimation by the linear fit could indicate that these properties are less sensitive to changes in tortuosity or affected by additional factors not captured by geometric tortuosity alone. This could serve as a valuable insight for modeling as it indicates a clear linkage between the microstructural complexity and the scale at which continuum assumptions become valid. The results confirm the intricate property-specific dependence of REV on the structural attributes of the pore networks.

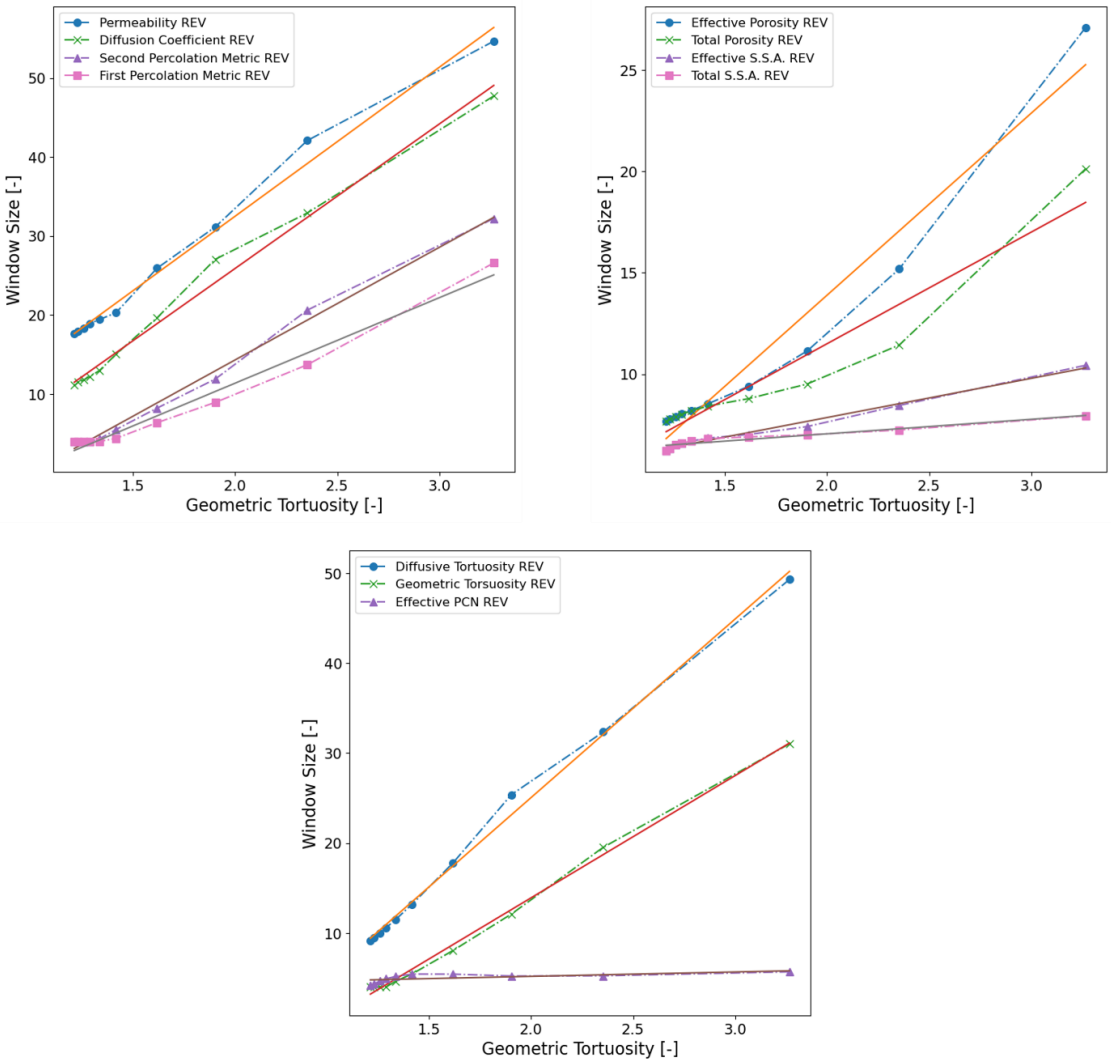

Figure 13: Representative Elementary Volume (REV) size scaling with geometric tortuosity across different rock properties. The top left graph correlates permeability, diffusion coefficient, and two percolation metrics with geometric tortuosity. The top right graph shows the relationship of effective porosity, total porosity, effective specific surface area (S.S.A.), and total S.S.A. The bottom graph compares diffusive tortuosity, geometric tortuosity, and effective pore coordination number (PCN).

Table 2 provides a summary of the linear regression parameters for sREV fits across both size and connectivity analyses, showing the slopes, extrapolated sREV sizes under homogeneity conditions, and coefficients of determination. The homogeneity conditions are defined as scenarios where the uniformity coefficient approaches zero and the geometric tortuosity equals unity, representing idealized conditions of perfectly uniform pore sizes and entirely straight flow paths. This conceptual framework allows us to interpret the influence of microstructural variations on the required scale of representativity. In the connectivity analysis, the homogeneity condition for geometric tortuosity—where all paths are ideally straight—results in larger sREV's compared to the uniformity coefficient's homogeneity condition due to the

fixed size distribution of pores, which introduces residual complexity even when paths are straight.

Table 2: Linear regression parameters for all sREV linear fits in the size and connectivity analysis , including the slope, the coefficient of determination, and the extrapolated sREV size at homogeneous conditions.

	Fit Parameters - Size			Fit Parameters - Connectivity		
Property	Slope	Homo.	Coeff.	Slope	Homo.	Coeff.
Effective P.C.N	-	-	-	0.49	4.0	0.44
Total S.S.A	2.3	2.9	0.99	1.0	5.5	0.94
Effective S.S.A	-	-	-	2.2	5.5	0.99
Total Porosity	3.4	3.1	1.0	11	7	0.86
Effective Porosity	-	-	-	15	7	0.91
Geom. Tortuosity	-	-	-	14	0.0	1.0
Diff. Tortuosity	2.4	5.3	0.97	20	4.3	1.0
Diff. Coefficient	4.9	3.9	0.99	18	6.9	0.99
Permeability	8.6	6.0	0.99	19	14	0.99

4.2 Property Scaling Analysis

Figure 14 and Figure 15 plot the average values of the computed properties at the final window size against the uniformity coefficient and the occupation probability, respectively, furnishing valuable insights into the upscaling of these properties in relation to network heterogeneity. The figures reveal the differing impacts of pore-size variations on viscous-driven versus diffusion-driven flow in porous media. Both permeability and diffusion coefficient decrease with increasing uniformity coefficient, but the decline in permeability is more pronounced due to its greater sensitivity to pore size heterogeneity. Hydraulic conductivity, governed by Hagen-Poiseuille's law, scales with the fourth power of the radius in cylindrical channels, making it highly dependent on the size of the largest pores and throats that dominate fluid flow. In heterogeneous networks, changes in the most conductive pathways significantly reduce permeability. In contrast, the diffusive conductivity, described by Fick's law, scales with the square of the diameter and is influenced by overall accessible pore space and tortuosity rather than just the largest pores. This allows diffusion to occur through a broader range of pathways, including smaller pores, making it less sensitive to heterogeneity.

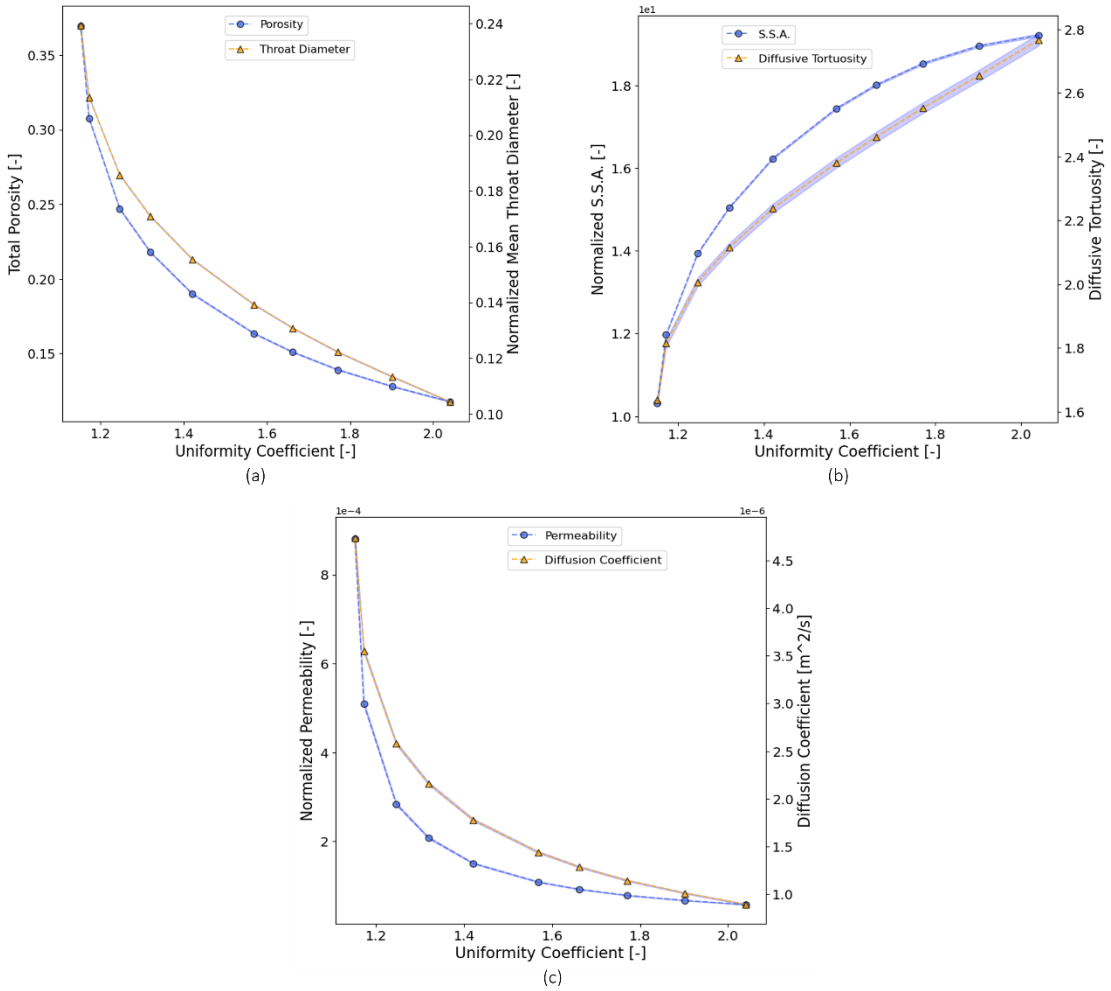

Figure 14: Scaling behavior of average properties across the range of investigated uniformity coefficients.

The figures show that both mean throat diameter and porosity decrease with uniformity coefficient. In more heterogeneous media, the presence of smaller pores reduces the overall average throat diameter, which directly diminishes the network's porosity. This reduction occurs because heterogeneous distributions tend to include narrower channels and void spaces, limiting the accessible pore volume. This relationship reveals how increasing pore size variability directly impacts the structural openness and overall capacity of the medium to store and transmit fluids, making these properties fundamental indicators of the influence of size heterogeneity.

Conversely, both specific surface area (SSA) and diffusive tortuosity increase with rising heterogeneity. Smaller pores contribute disproportionately to the total surface area. Simultaneously, diffusive tortuosity, which measures the complexity of pathways for diffusive transport, also rises due to the more convoluted routes created by heterogeneous pore distributions. This sheds light on how heterogeneity affects the interaction between fluid and

solid phases while complicating transport pathways, affecting the efficiency of diffusive processes in porous media.

Furthermore, the rate of change decreases the broader the pore size distribution becomes. Initially, increasing heterogeneity sharply reduces these properties due to the addition of smaller, restrictive pores. However, as heterogeneity continues to rise, the system reaches a saturation point where the structure is already dominated by restrictive features, and further increases in uniformity coefficient have a progressively smaller impact. The most accessible spaces are already minimized, resulting in only marginal further reductions.

The first and second percolation metrics in Figure 15 illustrate the critical sensitivity of the pore network to connectivity loss as the connection probability decreases. The first metric, which measures the percentage of pore volume within the largest cluster, sharply declines with reduced connectivity because the single dominant cluster fragments into smaller, isolated clusters. The second metric, representing the probability that two randomly selected pores belong to the same cluster, shows a similar but slightly steeper decline. Together, these metrics provide a concise yet comprehensive view of the breakdown in connectivity.

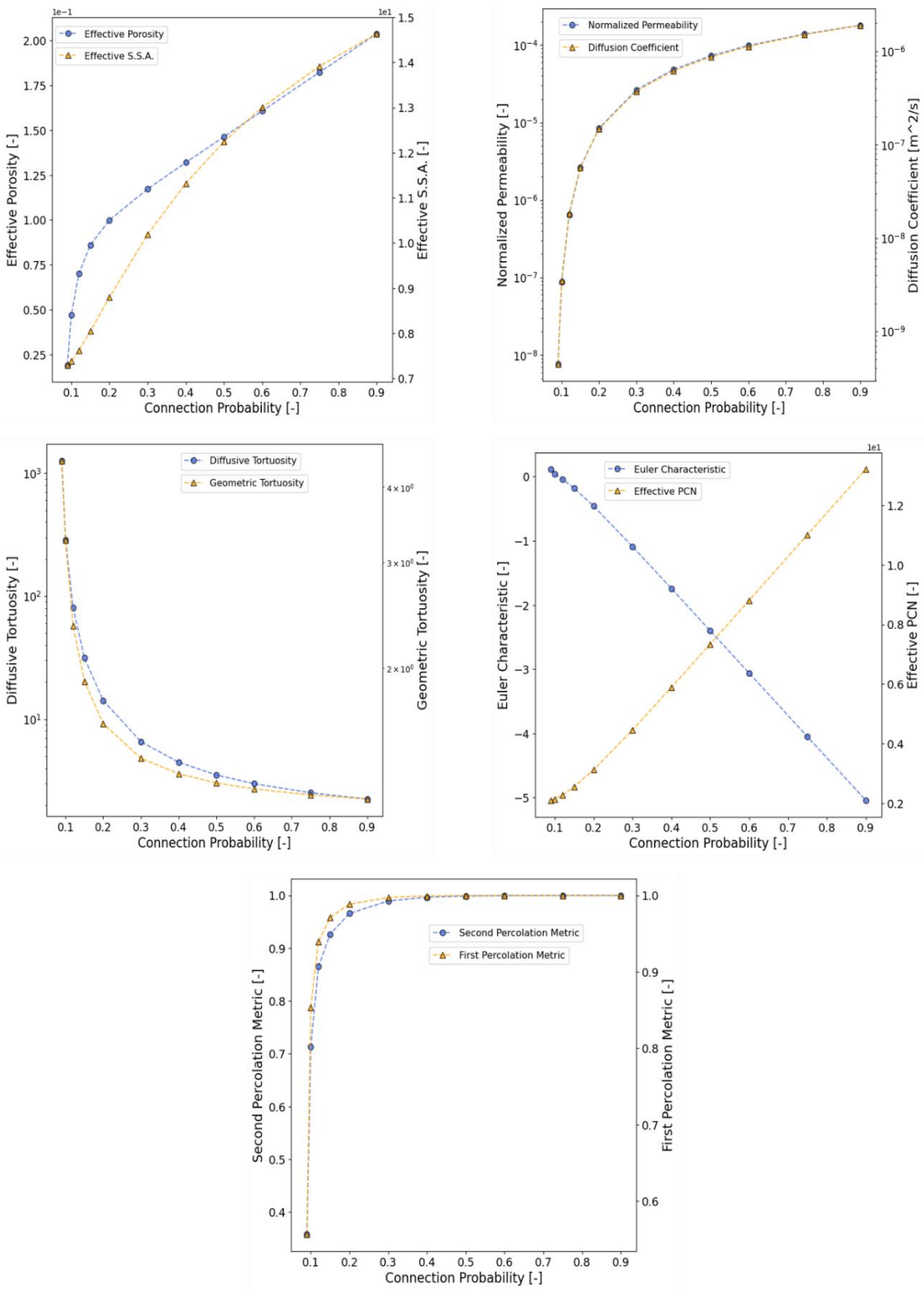

Figure 15: Relationship between occupation connectivity and various transport properties in a porous medium. The graphs illustrate the effects of decreasing occupation probability on various properties. The decline in permeability and diffusion coefficient on a semi-log scale highlights the sensitivity of these properties to changes in connectivity.

Permeability and diffusion coefficient exhibit a nearly identical functional shape on a semi-log scale, which is in contrast with the effect of pore size distribution, where permeability is more sensitive due to its dependence on larger flow channels, highlighting that connectivity proportionally disrupts both flow and diffusion mechanisms. Above a connection probability of 30%, where the network remains well-connected with excess throats, both properties decrease linearly. Because throat removal minimally impacts overall flow paths and percolation metrics, the linear decline matches the behavior observed in sREV. However, as connectivity nears the critical threshold, the decline becomes exponential, with even small reductions in connection probability causing dramatic drops that span several orders of magnitude.

The Euler characteristic and effective pore coordination number's linear variation with occupation probability align with the expectation for a pore network where throats are randomly removed. However, these linear metrics are insufficient to capture the nonlinear impact of connectivity changes on continuum properties. They do not account for the complex interplay between pore geometry and transport pathways. Therefore, while useful in describing topological features of the network, the Euler characteristic and pore coordination number alone do not provide a complete description of connectivity impact.

Instead, geometric tortuosity, with its non-linear variation, better reflects these dynamics by accounting for the increased complexity of paths. Unlike the linear expectations, geometric tortuosity shows how random throat deactivation elongates or blocks paths in a non-uniform manner across the network, highlighting disproportionate impacts on transport routes depending on their specific configurations. While both diffusive and geometric tortuosity increase as connectivity falls, diffusive tortuosity changes far more drastically—often to the thousands— due to its consideration of porosity. Thus, in ramified networks where the non-linear effects are critical to understanding the scaling of continuum properties, geometric tortuosity offers a more reliable description.

The evolution of effective porosity and specific surface area (SSA) shows distinct phases in response to connectivity changes. Initially, effective porosity decreases linearly, correlating with the reduction in active throats. However, beyond the clustering point, the decline steepens as isolated clusters form, contributing to pore space but not transport. This results in larger disconnected regions, significantly reducing the volume that supports effective flow, while SSA may increase due to the increased surface complexity of disconnected clusters.

The evolution of effective porosity and specific surface area (SSA) indicates distinct phases of behavior in response to connectivity changes. Initially, the reduction in effective porosity appears linear, reflecting a direct correspondence between the number of active throats and the volume available for flow. However, the decline intensifies past the clustering point. This suggests that the impact of disconnection becomes magnified due to the formation of isolated clusters that contribute to the pore space but do not facilitate transport. Increasingly larger portions of the pore space become disconnected from the main channels, disproportionately reducing the volume that contributes to effective porosity.

In order to investigate property evolution and the unfolding of the upscaling process, Figure 16 and Figure 17 depict the mean property values over the spatial range and across occupation probabilities, with 95% confidence intervals. A commonality among all properties is the gradual stabilization of the mean with increasing window size, which is an explicit condition for the determination of sREV using the CoV. However, especially at low occupation probabilities, significant variability and broader confidence intervals indicate that stabilized means may still inadequately represent effective transport behavior. This is particularly evident at 9% occupation probability, where fractal characteristics dominate, causing an unabating decline in permeability and diffusion. Below the correlation length, the system's scale invariance challenges traditional upscaling, with no clear transition to homogeneity. This section focuses on these transitions, emphasizing the critical role of scale in capturing the true transport properties of heterogeneous networks.

This sensitivity to the investigation scale below the correlation length is observed in other topology-dependent properties as well. As window size increases, geometric tortuosity rises sharply due to the need to navigate increasingly convoluted pathways. The observed peak occurs at the intersection where the sampling scale captures maximum irregularity. The continued increase in tortuosity up to the correlation length indicates that sampling still only includes fragmented paths rather than routes that can be averaged to something representative. Once window sizes exceed the correlation length, tortuosity begins to stabilize because the averaging process is able to diminish the impact of localized complexities.

The effective porosity graph shows higher values at smaller scales, decreasing with increasing window size, particularly in the 9% occupation network. This is because smaller sampling windows are more likely to capture segments of the percolating cluster in a way that maximizes the observed pore space. As the window size grows, the scale begins to capture the larger, interconnected structure, including the interstitial empty spaces or “holes” of the ramified cluster. For 10% and 12% occupation probabilities, a local minimum appears, followed by a rebound as the sampling window exceeds the correlation length and accommodates a higher proportion of connected pore space. This reflects the transition to sampling scales that more accurately represent the full spatial extent of the percolating cluster, which is underrepresented at smaller scales.

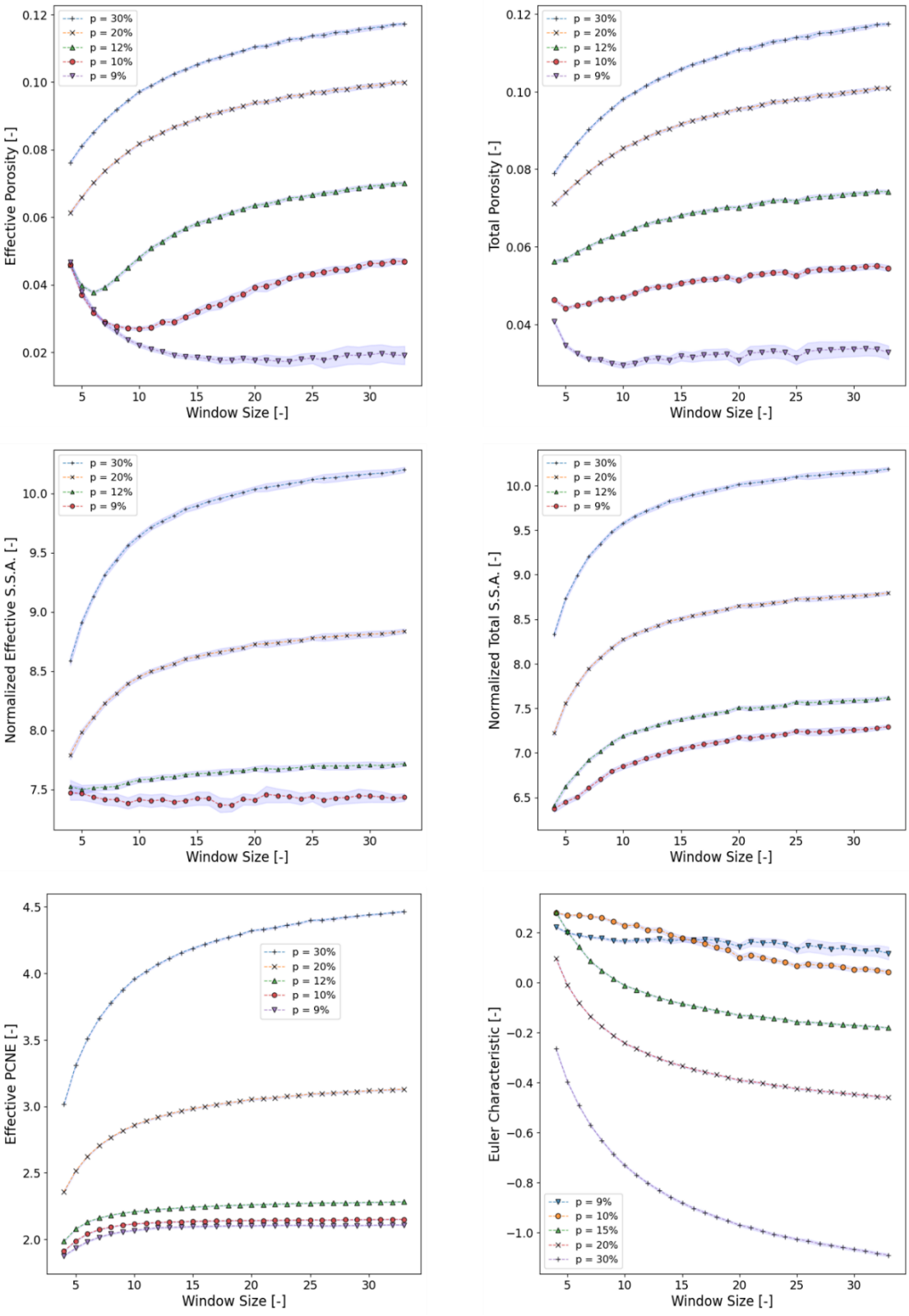

Figure 16: This graph illustrates the scaling behavior of effective porosity, specific surface area, effective coordination number, and Euler characteristic with increasing window size across different occupation probabilities (p = 9% to 30%).

As a result, in clustered networks below the correlation length, transport coefficients initially appear higher for lower occupation probabilities due to the structural simplicity of the percolating cluster near the percolation threshold. At these scales, the lower occupation networks exhibit less tortuous pathways because the percolating cluster forms through the merging of smaller, less convoluted clusters—favoring the least tortuous connections necessary to span the observation scale. This results in lower mean geometric tortuosity at smaller window sizes. However, as the observation scale expands, the inherent complexity of the fractal network emerges, revealing more circuitous pathways. Thus, initially, straighter paths at smaller scales transition into more complex routes at larger scales that cannot be described by a representative value, diminishing the permeability and diffusion coefficients due to the increasing fractal influence of the network's sparse connectivity.

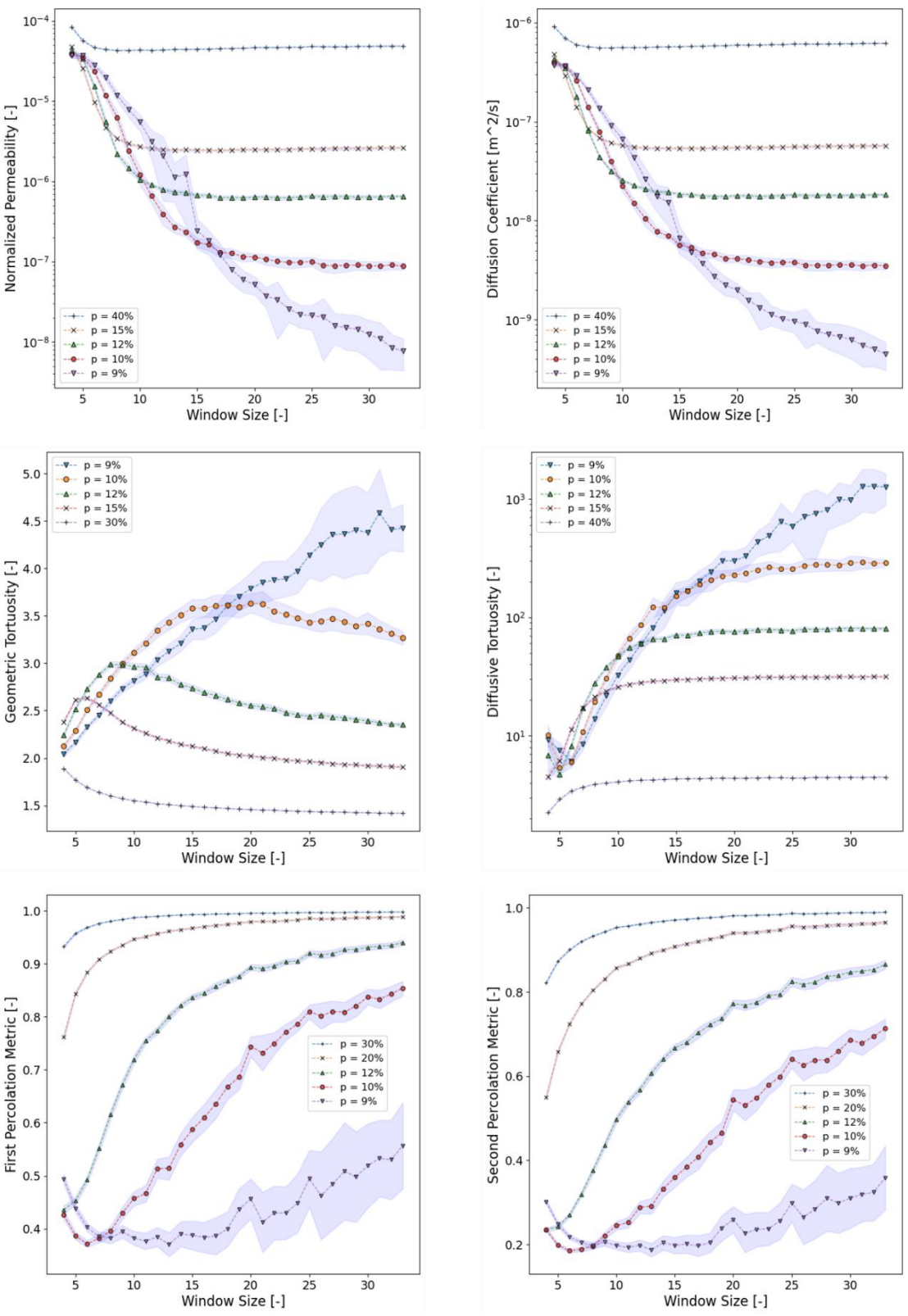

Figure 17: Depicting the evolution of normalized permeability, diffusion coefficient, tortuosity, and percolation metrics with window size for different occupation probabilities (p = 9% to 40%). The curves demonstrate how lower occupation probabilities result in higher initial tortuosity and slower stabilization of transport properties.

For networks where the correlation length is smaller than the smallest window size, property behaviors lack fractal influences. In porosity curves above 15% occupation, initially lower values stabilize after a monotonic increase due to smaller windows being more sensitive to local porosity variations and often biased toward regions of lower porosity. The increasing negativity in the Euler characteristic suggests that the number of throats grows faster than the number of pores, indicating enhanced connectivity and a rise in the number of loops relative to volume. This reflects the ability of larger windows to capture more of the network's topological features that smaller scales fail to adequately represent.

Finally, Figure 18 illustrates the evolution of geometric tortuosity distributions with increasing window size. As the window size grows, the interquartile range (IQR) narrows, reflecting a homogenization of available pathways. The shift towards a more platykurtic distribution shows that extreme values of tortuosity become less frequent, reducing the dominance of either highly tortuous or highly straightforward paths. Similarly, higher skewness in smaller windows reflects the presence of disproportionately high tortuosity, but an increasing window size symmetrizes the distribution. This statistical homogenization explains why, at higher occupation probabilities, mean tortuosity decreases with window size: larger windows better capture a representative sample of the network, including a greater number of more direct pathways that dominate flow. For these well-connected, even small windows capture a dense array of paths, resulting in elevated permeability and diffusion coefficients at smaller scales. This highlights the critical role of conductive pathways in transport characterization, where the variability in tortuosity is offset by the volume of direct paths, ensuring stable continuum behaviour even in the presence of tortuosity extremes at smaller scales.

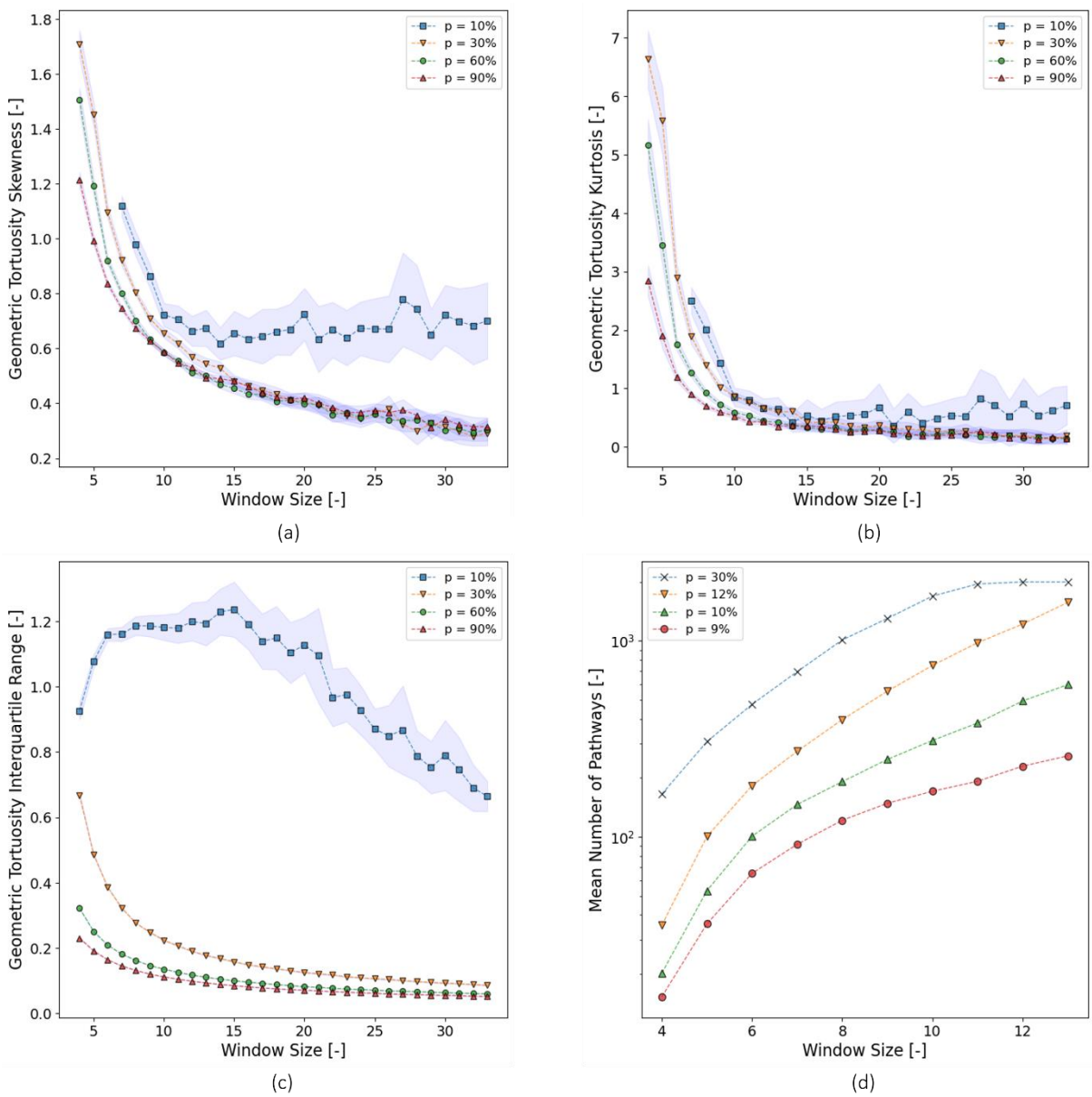

Figure 18: Scaling behavior of statistical properties of the geometric tortuosity distributions.

4.3 Regression Analysis

In this section, Accumulated Local Effects (ALE) plots are utilized to delve into the individual contributions of predictor variables to the permeability response across various window sizes, using a Random Forest Regressor model. Unlike traditional global interpretation methods that focus on average scaling behaviour, ALE plots allow for a nuanced examination of how each variable locally impacts the model's predictions by capturing the change in the predicted response as each predictor varies, while accounting for interactions with other features. This local interpretability provides a more accurate reflection of the relationship between predictor

variables and the permeability response, especially in complex, non-linear models like Random Forests, where interactions and dependencies between variables can obscure individual effects in average analyses.

ALE plots are constructed for the most significant features identified by the Random Forest model, which include mean geometric tortuosity, minimum geometric tortuosity, mean pore diameter, and the second percolation metric. These plots provide insights into the marginal effects of each feature on permeability by accumulating the localized changes in the model's response across the predictor's range, averaged over conditional distributions of the other features to provide a more reliable understanding of predictor influence on permeability. This approach allows us to refine our understanding of the complex interplay between network structure and transport properties, moving beyond average scaling to focus on the granular, local effects that drive the observed behaviours in permeability across scales.

The feature importance shown in Figure 19 illustrates how the relative significance of the predictors within the model evolves with increasing window size. In unclustered networks, mean geometric tortuosity consistently holds the highest importance across all window sizes, indicating that the overall tortuosity of paths plays a dominant role in modelling permeability when the network is intact. This suggests that the flow efficiency in well-connected networks is primarily governed by the complexity of hydraulic paths. The geometric tortuosity uniformity coefficient and the second percolation metric also maintain steady importance, reflecting the significant role of the distribution of tortuous paths and the extent of percolating clusters, even if it's unity throughout. The relatively stable feature importance across increasing window sizes for these variables implies that at, these properties consistently impact the permeability predictions.

In contrast, fragmented networks show more erratic shifts in feature importance at smaller scales. As the window size increases, the importance of the geometric tortuosity uniformity coefficient rises. This rising trend highlights how, in fragmented networks, the variability in tortuosity has a pronounced effect on permeability. The second percolation metric also shows increasing importance. These graphs indicate that the importance of predictor variables for permeability is scale-dependent and varies significantly with the underlying network connectivity.

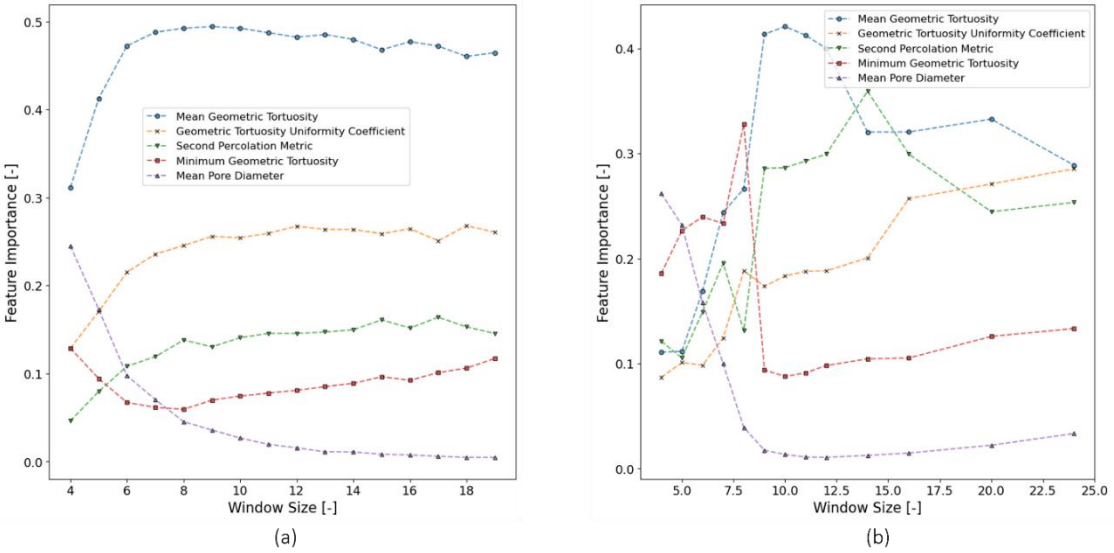

Figure 19: Feature importances for unfragmented (a) and fragmented (b) networks as a function of window size for the trained Random Forest Model.

It is interesting to note that the feature importance of mean pore diameter is notably higher at smaller window sizes and therefore seems to play a more significant role in model prediction at smaller scales. Physically, this could be attributed to individual pores and their sizes having a more pronounced impact on fluid flow in smaller scales because these windows capture less of the overall network's connectivity.

The ALE plots in Figure 20 illustrate the impact of mean geometric tortuosity on permeability predictions for unfragmented networks (left column, $p > 30\%$) and fragmented networks (right column, $p \leq 30\%$) across window sizes 6, 9, and 14. In both network types, a pronounced decline in the standardized effect on permeability by transforming it to have a mean of zero and a standard deviation of one to reduce the multicollinearity and improve interpretability, with increasing tortuosity is observed, such that even slight changes in mean tortuosity significantly reduce permeability, especially close to unity. The effect is most pronounced at smaller window sizes.

For unfragmented networks, the ALE plots reveal a plateau effect where further increases in tortuosity beyond a threshold do not significantly alter permeability. The surplus of throats within the percolating cluster provides a buffering capacity that maintains overall flow continuity despite local variations. This plateau indicates that, in well-connected systems, permeability is less sensitive to changes in tortuosity because redundant pathways mitigate the effect of greater tortuosity. In contrast, for fragmented networks, the influence of tortuosity on permeability remains strong and continuous across all scales. Here, even minor increases in tortuosity significantly impact the prediction, due to the presence of isolated clusters and dead-

end paths. The larger range of tortuosity values in fragmented networks causes overlap among different network configurations.

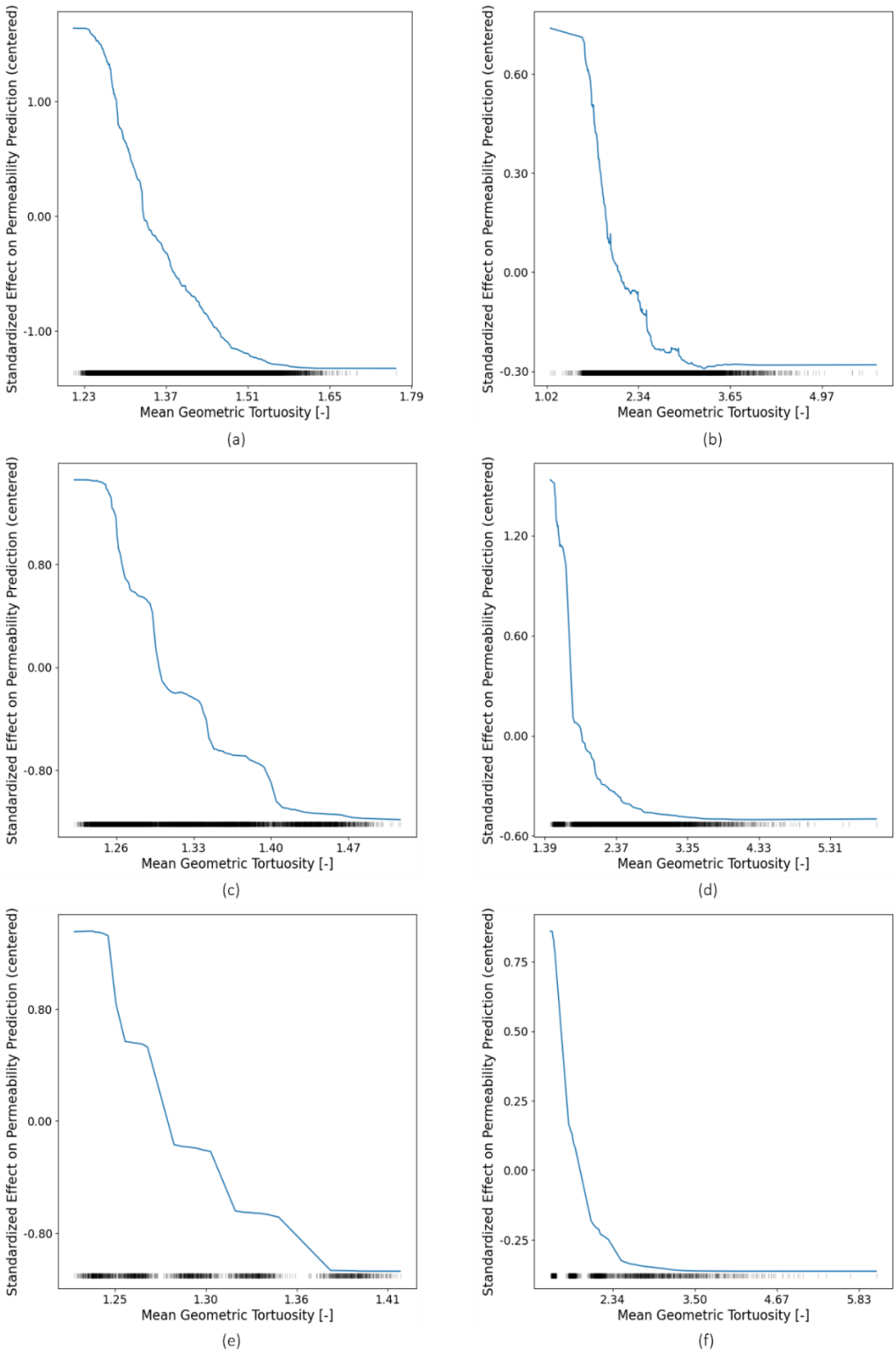

Figure 20: Series of 1D Accumulated Local Effects (ALE) plots illustrating the impact of mean geometric tortuosity on permeability predictions in porous networks. The left column (a, c, e) represents unclustered networks. The right column (b, d, f) depicts clustered networks, characterized

by fragmented percolation clusters that introduce significant heterogeneity. Figures (a) and (b) correspond to subwindows with a unit size of 6, (c) and (d) to a unit size of 9, and (e) and (f) to a unit size of 14. The horizontal color bar at the bottom represents the data point density.

Figure 21 reveals a steep initial decline in the ALE plots of minimum geometric tortuosity, showing that increases in the smallest available tortuosity significantly reduce permeability by adding resistance to the most conductive pathways. This effect quickly plateaus, suggesting that once a critical level of tortuosity is reached, further increases add little additional resistance as the network. As window size increases, the standardized effect on the permeability prediction diminishes due to the transition from localized flow resistance to more aggregated flow characteristics. This reflects that while minimum tortuosity critically affects permeability in smaller, localized regions, its impact fades as broader spatial extents are considered, with mean tortuosity emerging as a more dominant factor. The correlation between increasing minimum tortuosity and mean tortuosity suggests a uniform rise in complexity across the network rather than isolated spikes, such that that changes in minimum tortuosity are indicative of broader structural shifts.

The ALE plots for the tortuosity uniformity coefficient in Figure 22 show diverse trends. The uniformity coefficient, which measures the spread of the middle 80% of tortuosity values scaled by the median, captures how broader distributions affect permeability. At smaller scales, higher uniformity coefficients generally enhance permeability by facilitating a mix of pathways that includes efficient, less tortuous routes. However, as scale increases, this heterogeneity begins to hinder flow by reducing the overall pathway efficiency, as the impact of highly conductive pathways diminishes when spread across a broader, more heterogeneous network. At the largest scale (window size 14), a broader distribution of tortuosity uniformly decreases permeability predictions for both clustered and unclustered networks, indicating that even the presence of less tortuous pathways cannot compensate for the increased resistance from the overall network structure. The scale-dependent nature of tortuosity effects, where a broad distribution can either support or impede flow depending on the balance of pathway efficiency versus resistance.

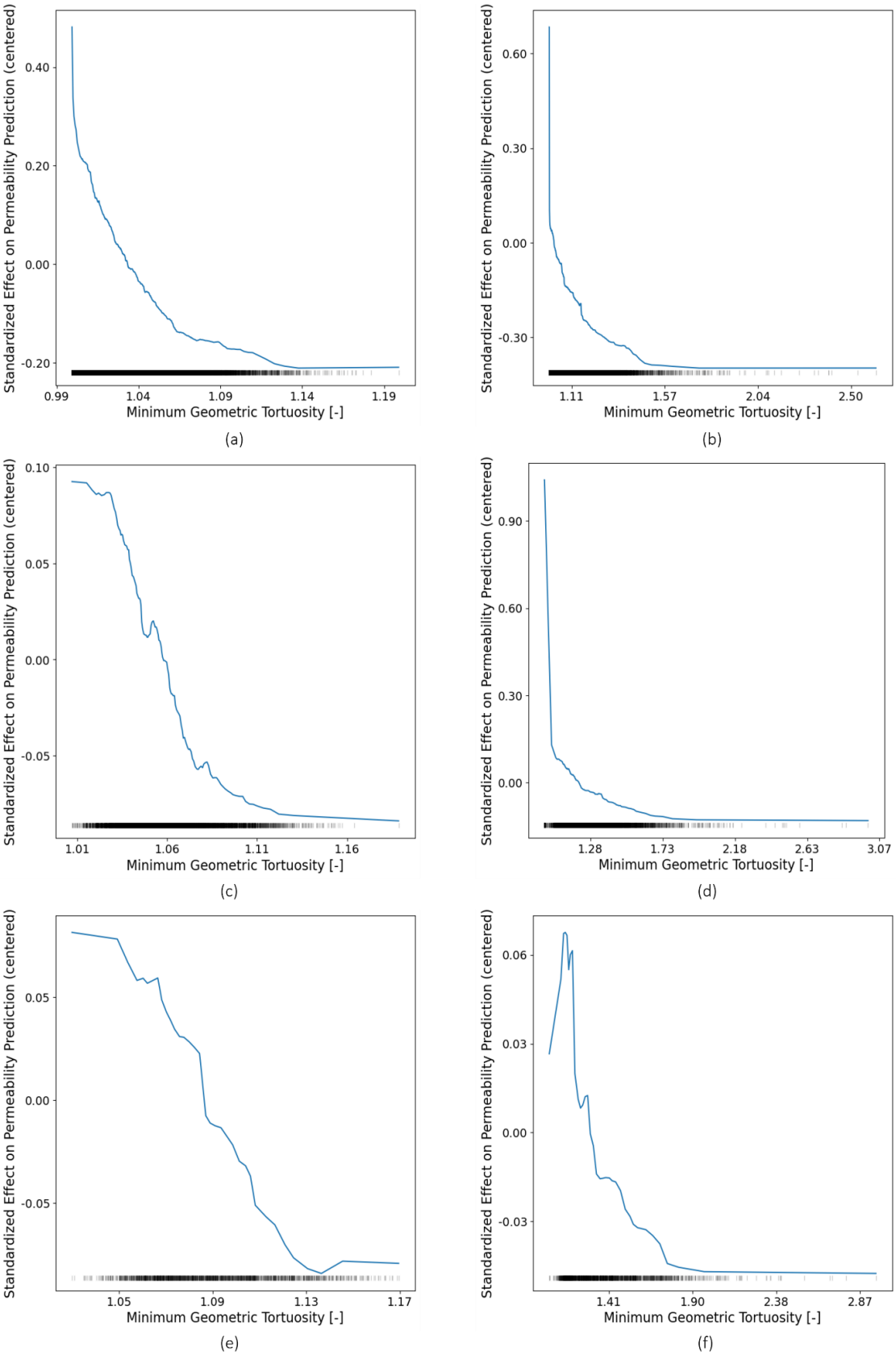

Figure 21: Series of 1D Accumulated Local Effects (ALE) plots illustrating the impact of minimum geometric tortuosity on permeability predictions in porous networks.

The ALE plots for mean pore diameter (Figure 23) consistently show a monotonic increase, indicating that larger mean pore diameters positively impact permeability, which aligns with physical expectations. The approximately linear effect implies that the impact of mean pore diameter on permeability remains stable across different network configurations. Since the networks were generated through random throat removal without directly altering pore sizes, the mean diameter stays relatively constant despite variations in occupation probability. The uniformity of mean pore diameters across the analyzed networks implies that the observed linear relationship reflects the functional capacity of the connected pores—those significantly contributing to flow—rather than changes in pore size itself.

For size 6 and 9, as the second percolation metric increases, indicating higher probabilities of intra-cluster connectivity, the ALE plots initially show a decrease in the standardized effect on permeability prediction, which then transitions to an increase, particularly notable at higher values of the metric (Figure 24). The magnitude of the change in the ALE values and the turning point of the curve (or lack thereof) depends on the scale. The plot for size 14, for example, shows a monotonic relationship. The semi-log cross-plot in fig. of permeability versus the second percolation metric color-coded by the occupation probability offers an explanation by way of how permeability behaves under extensive fragmentation in a pore network. At very low values of the second percolation metric corresponding to $p = 10\%$ as denoted by the square markers, there is a tremendous amount of variance in the encountered permeability values because of the presence of a relatively small number of pathways that dominate the flow in a very strong manner. As discussed in the previous section, the network is below the correlation length and therefore exhibits fractal behavior where even a window size of 9 units is insufficient to capture a representative sample of the network behavior. However, for larger values of occupation probability a better connectivity emerges that leads to a bounded, more consistent trend as more paths become part of a connected cluster that does not have a fractal character. The network's behavior becomes more predictable and less sensitive to changes in structure. Additionally, the second percolation metric, along with the mean tortuosity, retains significant ALE values at the largest investigated window size.

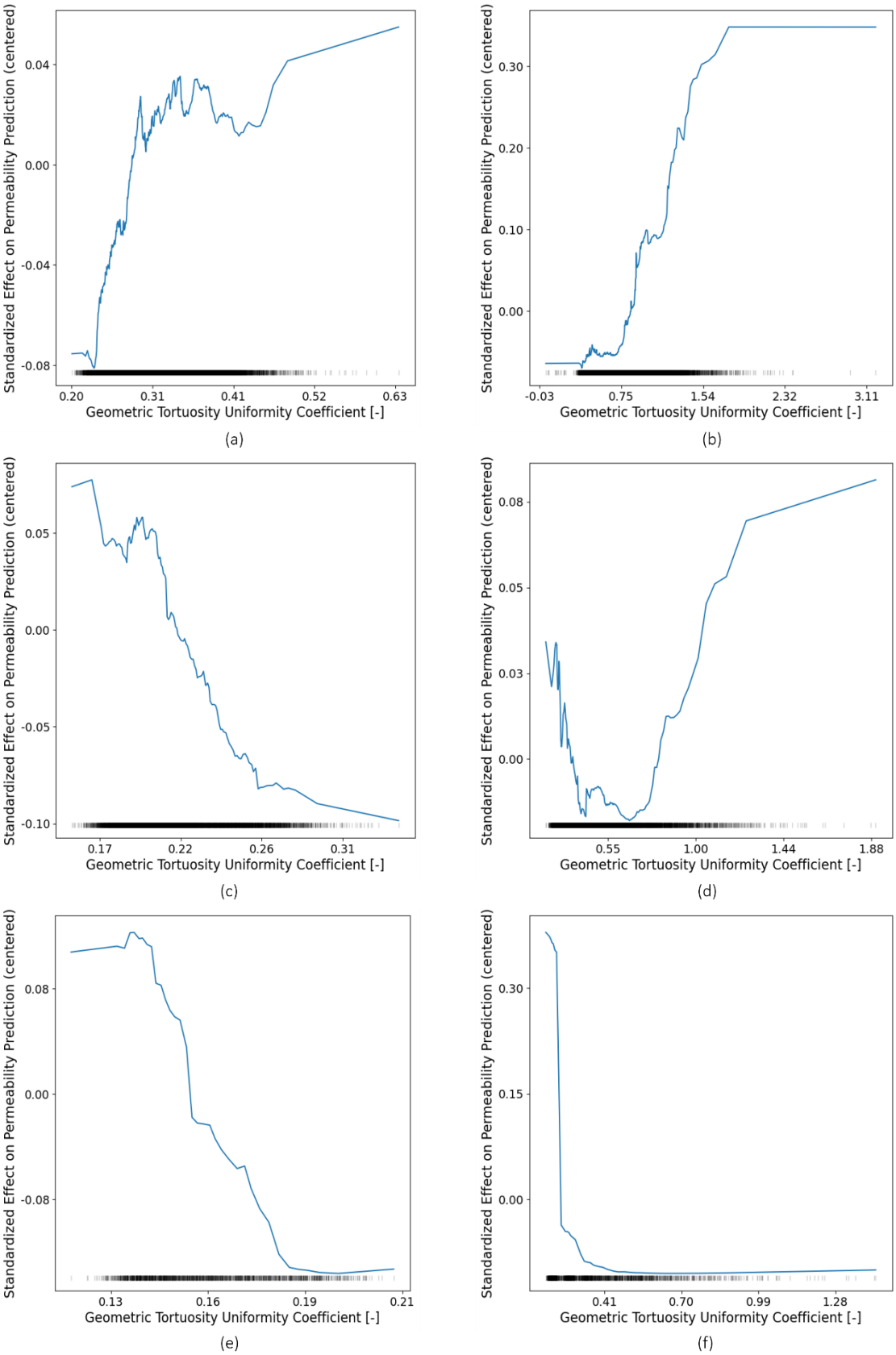

Figure 22: Series of 1D Accumulated Local Effects (ALE) plots illustrating the impact of geometric tortuosity uniformity coefficient on permeability predictions in porous network.

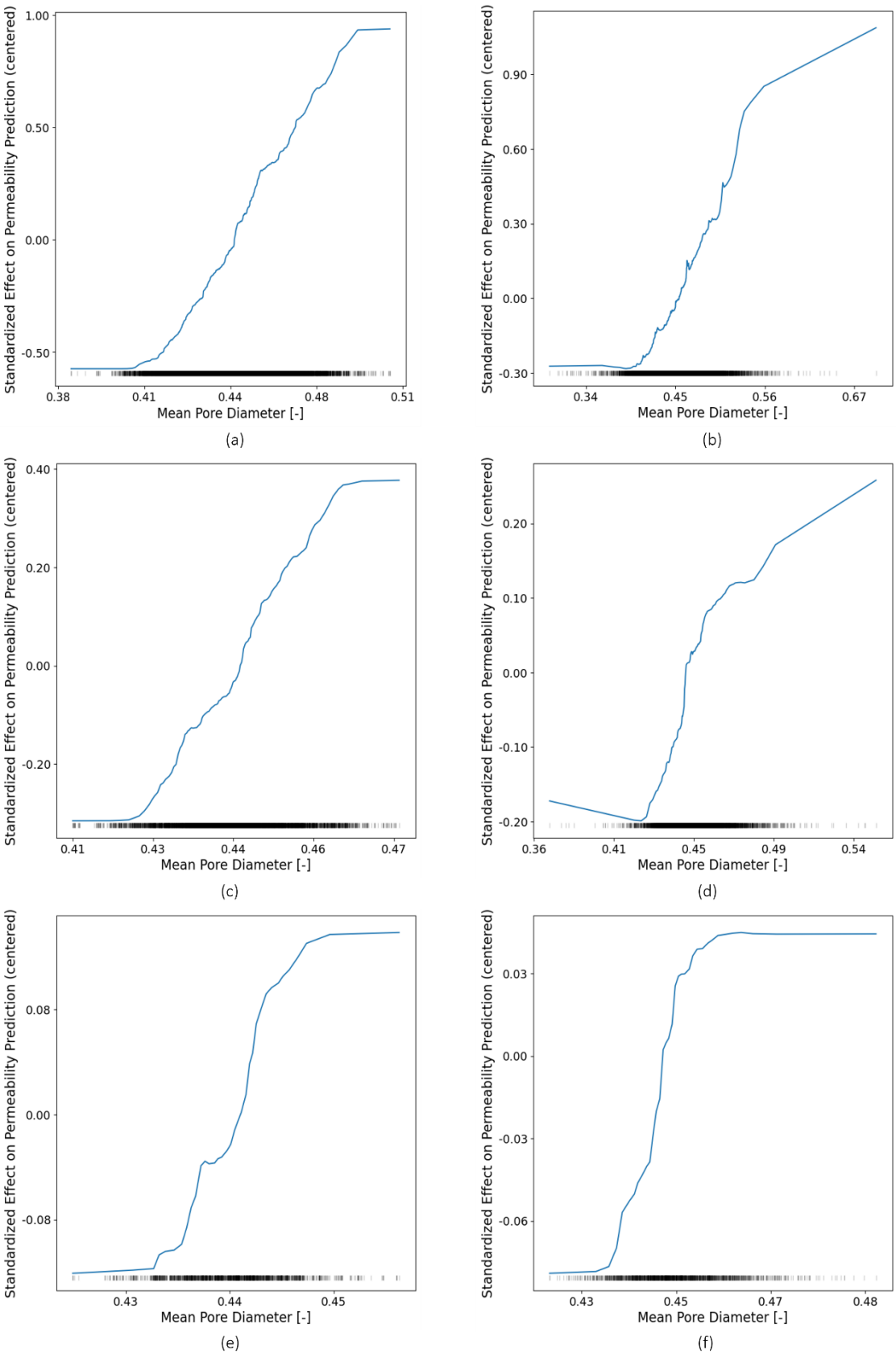

Figure 23: Series of 1D Accumulated Local Effects (ALE) plots illustrating the impact of mean pore diameter on permeability predictions in porous networks.

The cross plot of permeability versus the second percolation metric, color-coded by network occupation probability, supports the ALE findings. For lower occupation probabilities (e.g., $p = 10\%$, shown by squares), there is significant spread in permeability values, which aligns with the initial decrease in the ALE plots where improvements in connectivity have limited impact. As occupation probability increases (e.g., $p = 20\%$ and $p = 30\%$, shown by circles and triangles), data points shift upward and rightward, indicating a consistent and substantial increase in permeability with less fragmentation. This supports the ALE findings.

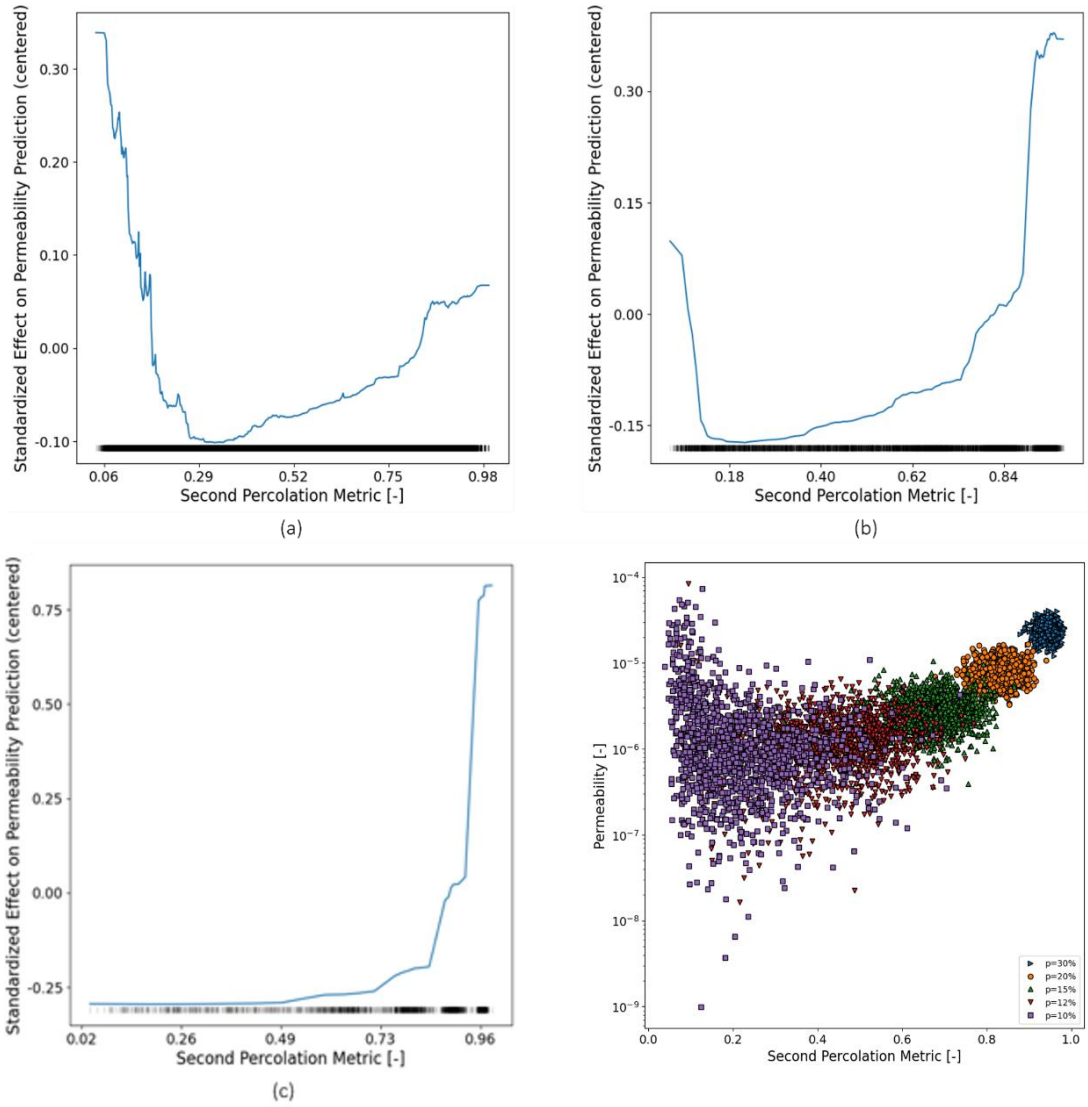

Figure 24: Series of 1D Accumulated Local Effects (ALE) plots illustrating the impact of the second percolation metric on permeability predictions in porous networks.

2D Accumulated Local Effects (ALE) plots extend the capabilities of 1D ALE plots by capturing interaction effects between pairs of features, providing insights into how these interactions impact model predictions beyond the isolated influence of each feature. While 1D ALE plots are effective in revealing the main effects of individual features, they fail to account for how features may interact with each other to influence the prediction. 2D ALE plots address this by partitioning the feature space into a grid, computing localized effects within each grid cell, and calculating second-order differences that isolate the purely interaction-driven effects. This method subtracts the main effects of the features, allowing the visualization of the residual impact that arises purely from their combined variation. The utility of 2D ALE plots lies in their ability to reveal whether the simultaneous changes in two features produce synergistic, antagonistic, or neutral effects on the model's predictions—effects that are not evident when considering features independently. By exploring these complex dependencies, 2D ALE plots provide a more nuanced understanding of the interdependencies within the model.

The 2D ALE plots of mean geometric tortuosity versus mean pore diameter in Figure 25 for unfragmented networks reveal distinct interaction effects, especially at smaller window sizes. Positive interaction effects occur where tortuosity is low and pore diameters are large, as well as in the opposite configuration of high tortuosity and small pore diameters. The combination of low tortuosity and large pore diameters facilitates efficient fluid flow, enhancing permeability. Conversely, negative interaction effects are seen when both tortuosity and pore diameter are either low or high. Small pore diameters with low tortuosity create uniformly restrictive paths, while large pore diameters with high tortuosity introduce flow inefficiencies due to convoluted routes, even with ample pore space. As window size increases from 6 to 14 units, these interaction effects diminish, indicating that the interaction effects of specific configurations weaken with scale.

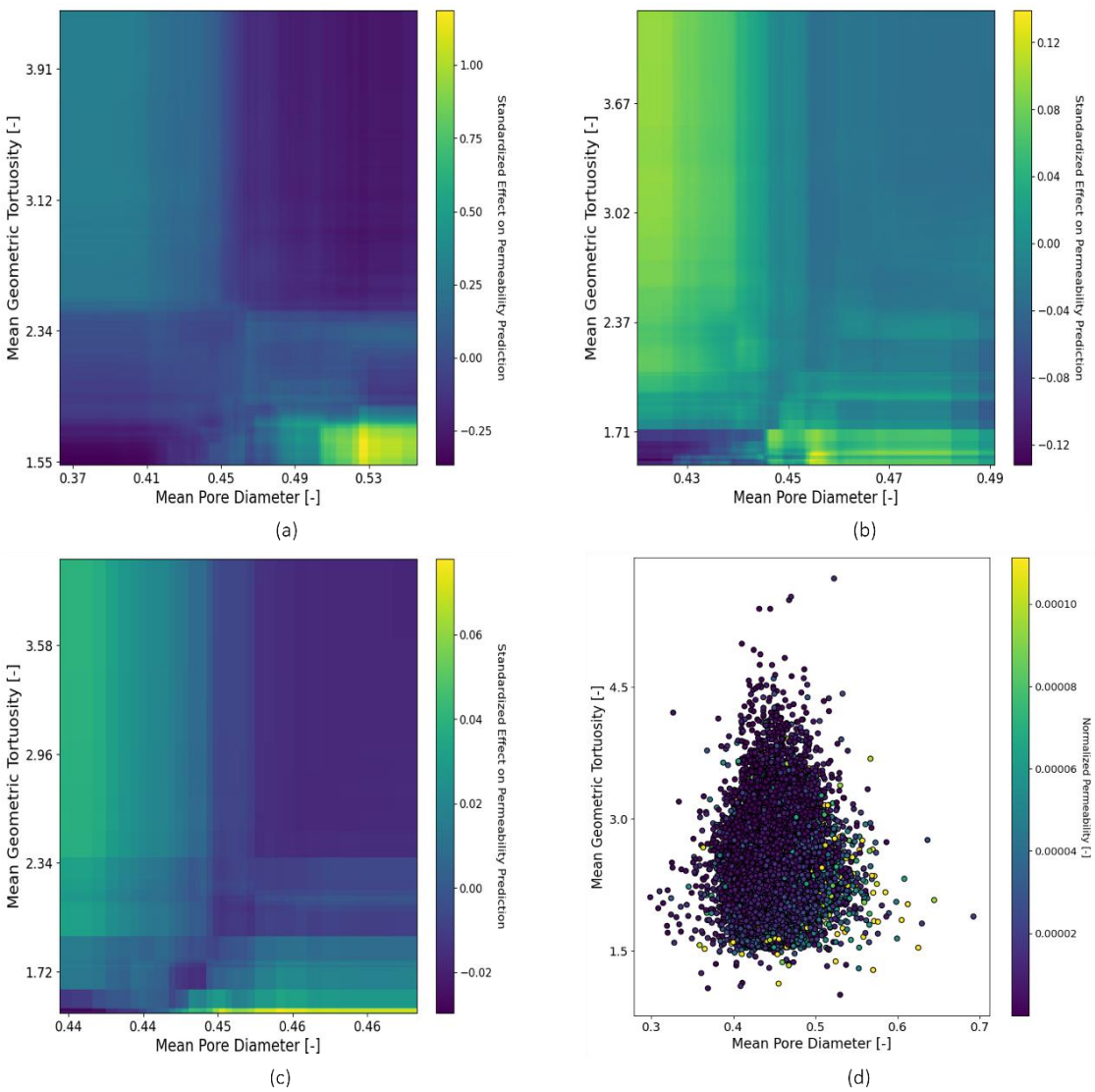

Figure 25: Series of 2D Accumulated Local Effects (ALE) plots illustrating the impact of mean geometric tortuosity interacting with mean pore diameter on permeability predictions in unfragmented porous networks.

There are both parallels and distinctions in the ALE plots for fragmented networks in Figure 26 (below 30% occupation probability). In fragmented networks, interaction effects between mean geometric tortuosity and mean pore diameter follow familiar patterns, such as larger pores enhancing flow and higher tortuosity impeding it, indicating that fundamental flow dynamics persist despite fragmentation. However, these effects are generally weaker and more dispersed. The reduced clarity and strength of interactions suggest that connectivity loss, characteristic of these fragmented networks, imposes a dominant influence that can overshadow the subtler interplay of pore structure and tortuosity. Regions with extreme combinations of tortuosity and pore diameter, indicated by areas of low data density, are particularly prone to variability and less reliable model predictions.

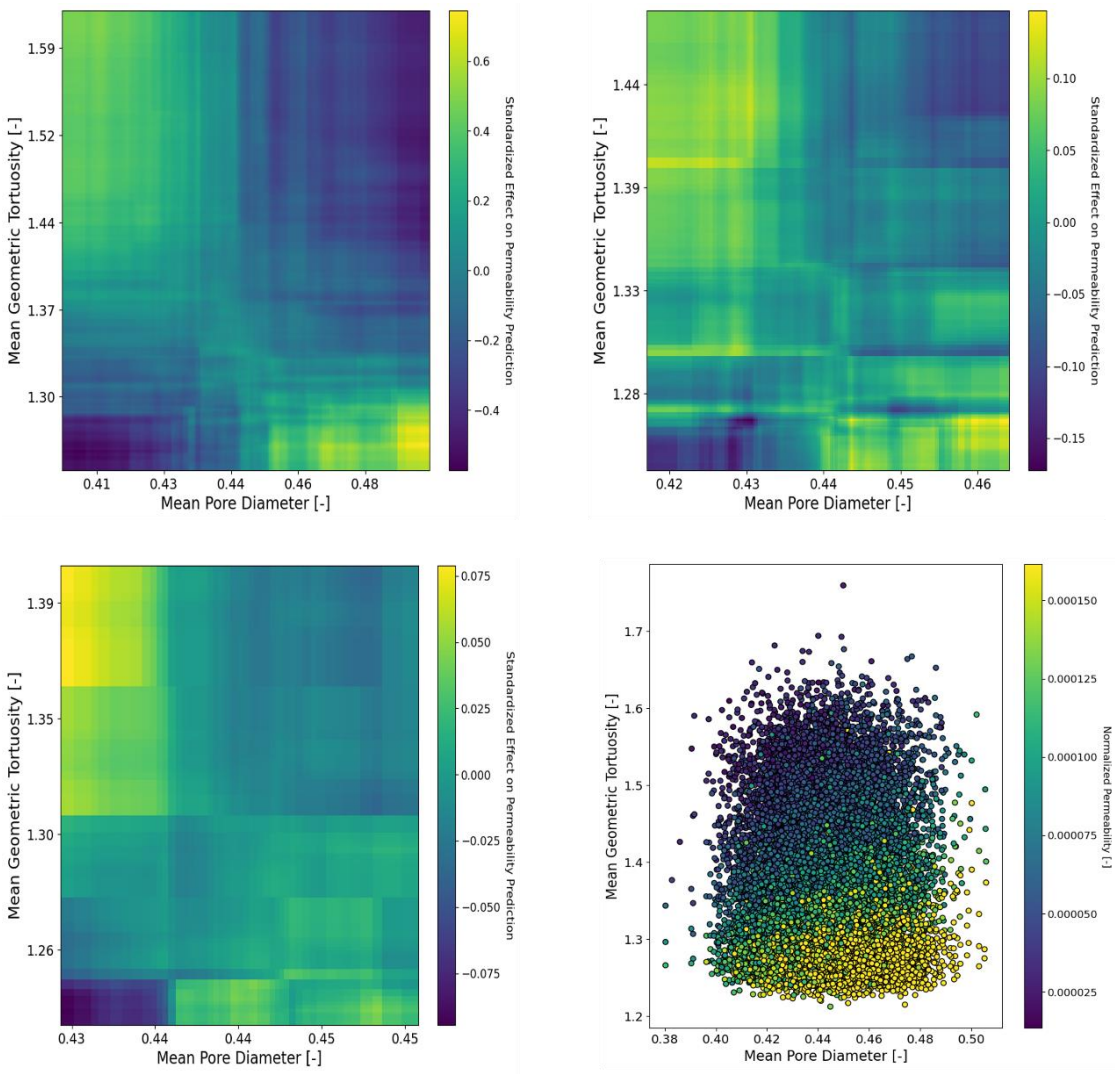

Figure 26: Series of 2D Accumulated Local Effects (ALE) plots illustrating the impact of mean geometric tortuosity interacting with mean pore diameter on permeability predictions in fragmented porous networks.

Figure 27 provides a perspective on how variations within tortuosity metrics interact to influence the prediction. Areas with significant positive interaction effects are seen to occur where the mean and minimum tortuosity converge. Regions with pronounced negative effects are observed where both mean and minimum tortuosity align either at higher or lower ends of the feature space, with combinations of low mean tortuosity and high minimum tortuosity, and high mean tortuosity and low minimum tortuosity. For the clustered network group in Figure 28, the interaction effects are considerably less pronounced and largely absent across the majority of the feature space. The majority of the feature space in the 2D ALE plots shows very minimal to zero interaction effects between mean and minimum geometric tortuosity. The interaction effects that do appear are localized in regions far removed from the main concentration of data points, indicating that these are not representative of the typical network

conditions. The absence of strong multiplicative interactions across most of the feature space implies that the model primarily responds to other factors or individual effects of these features rather than their combined influence.

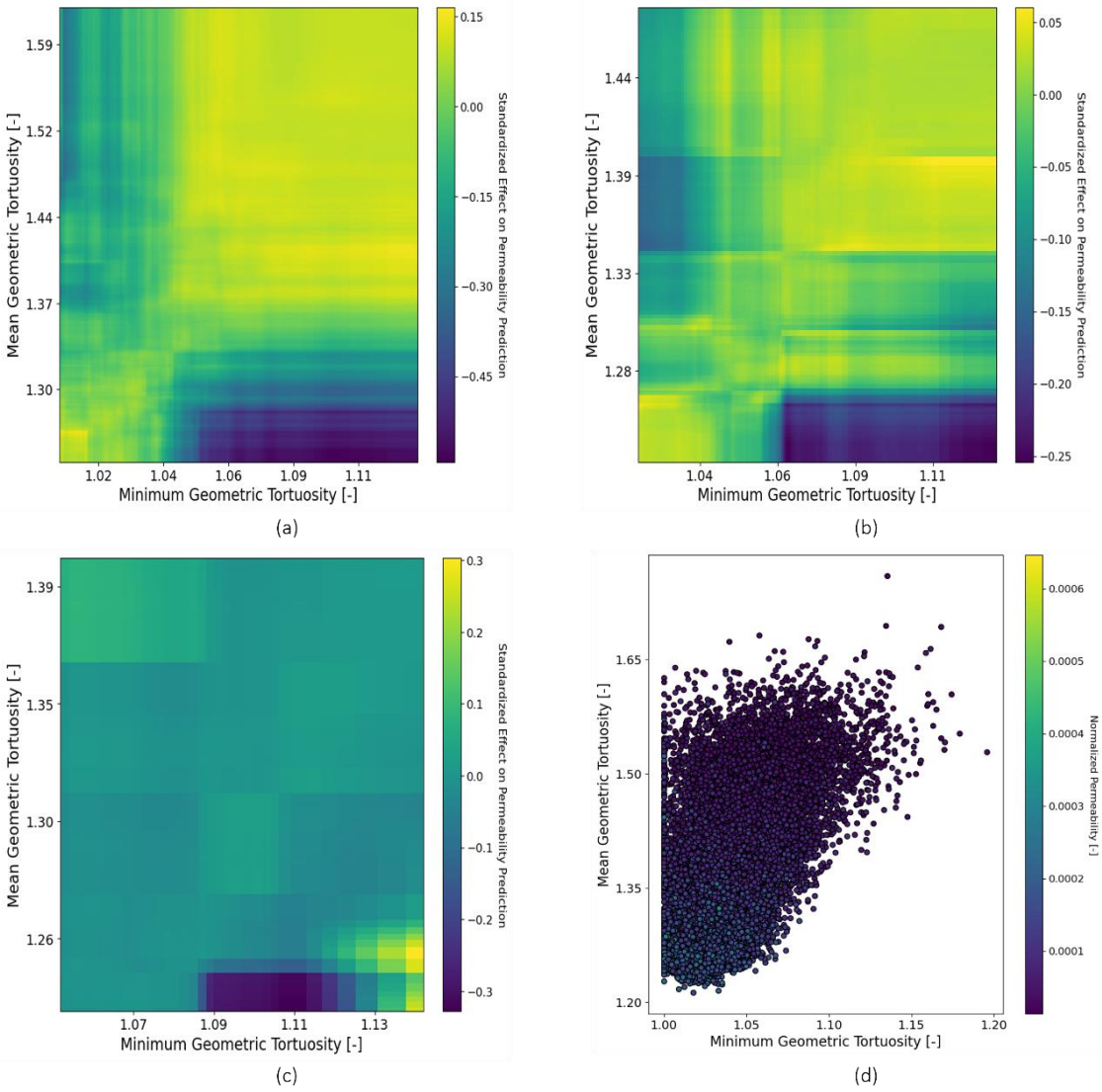

Figure 27: Series of 2D Accumulated Local Effects (ALE) plots illustrating the impact of mean geometric tortuosity interacting with minimum geometric tortuosity on permeability predictions in unfragmented porous networks.

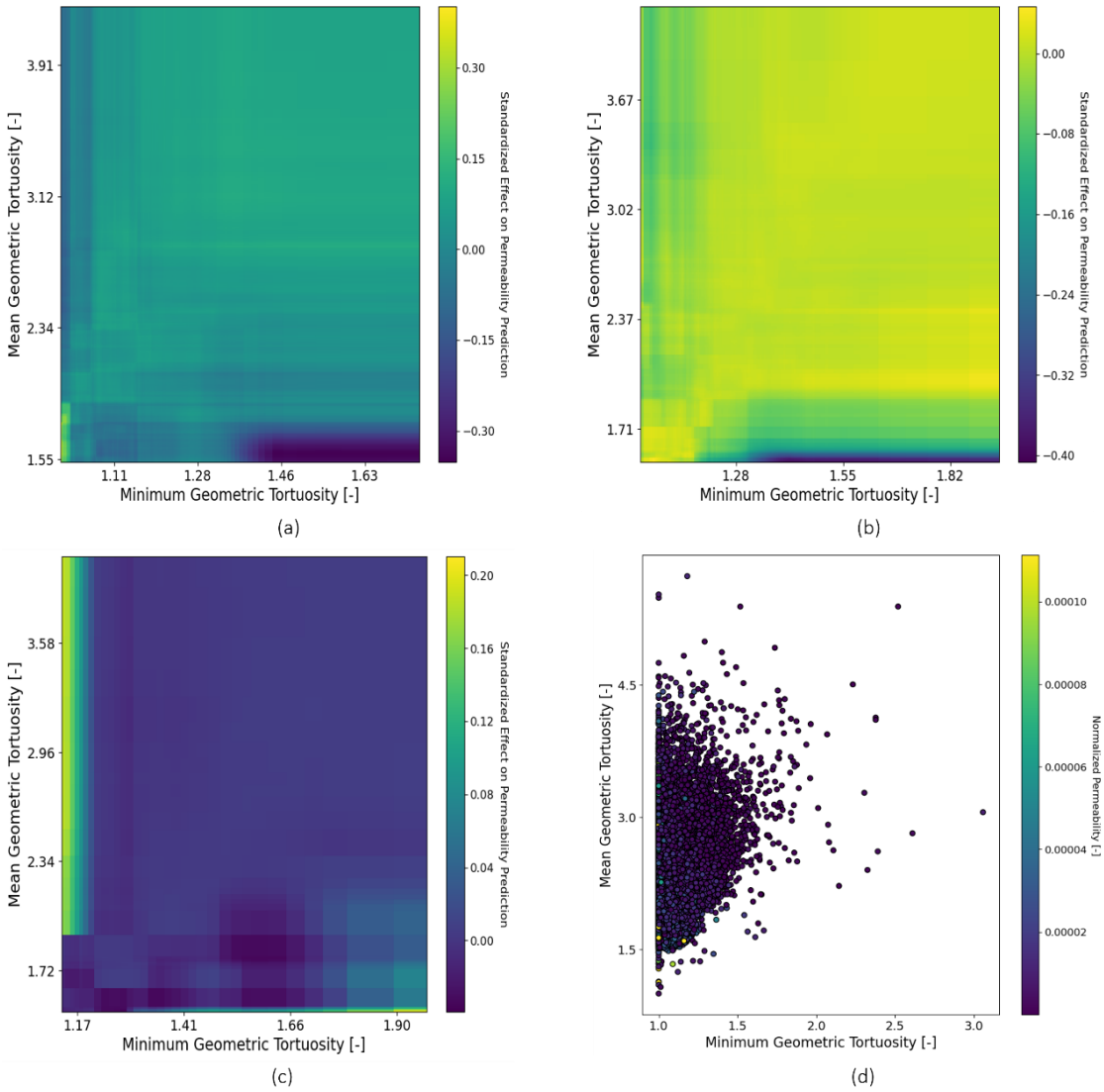

Figure 28: Series of 2D Accumulated Local Effects (ALE) plots illustrating the impact of mean geometric tortuosity interacting with mean pore diameter on permeability predictions in fragmented porous networks.

Across the various plots, interaction effects manifest consistently irrespective of window size, although the intensity and clarity of these interactions tend to fluctuate. Notably, in larger analysis windows, there is a noticeable decrease in the magnitude of these interaction effects. This trend stems from the averaging processes inherent in larger window analyses, which tend to mitigate not only the effects of individual features but also the second-order interaction effects.

Chapter 5

Conclusion

This thesis has comprehensively examined the complexities of upscaling from pore to Darcy scale through evaluations of the Representative Elementary Volume (REV), property scaling behaviors, and regression analysis using a domain-wide statistical sampling approach for homogeneous and isotropic pore network models.

The REV analysis effectively illustrated the scale-dependent variability in pore networks, as demonstrated by the exponential decay of the Coefficient of Variation (CoV) with increasing window sizes. This decline is indicative of a homogenization process, where larger sampling volumes average out the microstructural heterogeneities. The fitted exponential decay functions for the CoV across different properties underscore a systematic approach to determining REV thresholds and quantifying the impact of network connectivity on statistical dispersion. It was found that properties displayed unique REV scales, which varied uniquely depending on the underlying microstructural heterogeneity, and were intimately tied to the existence of the correlation length.

The property scaling analysis provided a nuanced view of property averages across varying scales and occupation probabilities. Distinct property-specific trends were observed across scales straddling the identified correlation lengths. For scales below the REV, properties exhibited significant fluctuations influenced by local heterogeneities. These sub-REV behaviors provide crucial insights into the microscale interactions and their impact on flow and transport phenomena. As the scale approached and exceeded the REV, a transition to a more homogeneous and predictable behavior was noted, affirming the continuum hypothesis. However, at occupation probabilities near the percolation threshold, the scaling behavior breaks down, indicating no singular scale can yield representative continuum behavior due to the emergence of fractal behavior. This finding suggests a need for a more adaptive approach to handling near-threshold phenomena.

Accumulated Local Effects (ALE) plots provided model-derived insights into the relationships between pore-scale properties and permeability. These plots highlighted how changes in properties like geometric tortuosity and pore diameter significantly affect permeability, especially in smaller window sizes where the network's microstructure has a more pronounced impact on flow properties. The ALE analysis showed that mean geometric tortuosity is a consistent predictor of permeability across various scales, underscoring its importance in capturing the network's overall resistance to flow, and illuminated interaction effects between features.

The integration of REV analysis, property scaling, and regression insights paints a clearer picture of the upscaling process from pore to continuum scales. The findings demonstrate that while upscaling can homogenize certain properties, critical thresholds like the percolation point introduce significant challenges that require careful consideration and possibly novel modeling approaches to accurately predict and manage.

Recommendations for further work include incorporating more realistic pore architecture from extracted models to capture a wider range of different heterogeneities and explore the upscaling footprint on more complex structures in more granular detail. Furthermore, designing targeted experiments to validate the scaling relationships derived in this study and enhance the empirical foundations of upscaling methodologies.

References

Akbari, M., Sinton, D., & Bahrami, M. (2011). Viscous flow in variable cross-section microchannels of arbitrary shapes. *International Journal of Heat and Mass Transfer, 54*(17-18), 3970-3978. https://doi.org/10.1016/j.ijheatmasstransfer.2011.04.004

Al-Raoush, R., & Papadopoulos, A. (2010, June). Representative elementary volume analysis of porous media using X-ray computed tomography. *Powder Technology*, *200*(1–2), 69–77. https://doi.org/10.1016/j.powtec.2010.02.011

An, S., Hasan, S., Erfani, H., Babaei, M., & Niasar, V. (2020, August). Unravelling Effects of the Pore-Size Correlation Length on the Two-Phase Flow and Solute Transport Properties: GPU-based Pore-Network Modeling. *Water Resources Research*, *56*(8). https://doi.org/10.1029/2020wr027403

An, S., Yao, J., Yang, Y., Zhang, L., Zhao, J., & Gao, Y. (2016, April). Influence of pore structure parameters on flow characteristics based on a digital rock and the pore network model. *Journal of Natural Gas Science and Engineering*, *31*, 156–163. https://doi.org/10.1016/j.jngse.2016.03.009

Armstrong, R. T., McClure, J. E., Robins, V., Liu, Z., Arns, C. H., Schlüter, S., & Berg, S. (2019). Porous media characterization using Minkowski functionals: Theories, applications, and future directions. *Transport in Porous Media, 130*(1), 305–335. https://doi.org/10.1007/s11242-018-1201-4

Babaei, M., & Joekar-Niasar, V. (2016, June). A transport phase diagram for pore-level correlated porous media. *Advances in Water Resources*, *92*, 23–29. https://doi.org/10.1016/j.advwatres.2016.03.014

Banavar, J. R., & Schwartz, L. M. (1987). Magnetic resonance as a probe of permeability in porous media. *Physical Review Letters, 58*(14), 1411–1414. https://doi.org/10.1103/PhysRevLett.58.1411

Baveye, P., Rogasik, H., Wendroth, O., Onasch, I., & Crawford, J. W. (2002, April 18). Effect of sampling volume on the measurement of soil physical properties: simulation with x-ray tomography data. *Measurement Science and Technology*, *13*(5), 775–784. https://doi.org/10.1088/0957-0233/13/5/316

Bear, J. (1972). *Dynamics of fluids in porous media*. American Elsevier Publishing Company.

Berg, R. R. (1970). Method for determining permeability from reservoir rock properties. *Journal of Petroleum Technology, 22*(8), 915–920.

Berg, C. F. (2014, April 4). Permeability Description by Characteristic Length, Tortuosity, Constriction and Porosity. *Transport in Porous Media*, *103*(3), 381–400. https://doi.org/10.1007/s11242-014-0307-6

Biswal, B., Manwart, C., & Hilfer, R. (1998, July). Three-dimensional local porosity analysis of porous media. *Physica A: Statistical Mechanics and Its Applications*, *255*(3–4), 221–241. https://doi.org/10.1016/s0378-4371(98)00111-3

Blunt, M. J. (1997, March 1). Effects of Heterogeneity and Wetting on Relative Permeability Using Pore Level Modeling. *SPE Journal*, *2*(01), 70–87. https://doi.org/10.2118/36762-pa

Bo-Ming, Y. (2004, December 23). Fractal Character for Tortuous Streamtubes in Porous Media. *Chinese Physics Letters*, *22*(1), 158–160. https://doi.org/10.1088/0256-307x/22/1/045

Borges, J. A., Pires, L. F., Cássaro, F. A., Roque, W. L., Heck, R. J., Rosa, J. A., & Wolf, F. G. (2018, October). X-ray microtomography analysis of representative elementary volume (REV) of soil morphological and geometrical properties. *Soil and Tillage Research*, *182*, 112–122. https://doi.org/10.1016/j.still.2018.05.004

Brown, G. O., Hsieh, H. T., & Lucero, D. A. (2000, May). Evaluation of laboratory dolomite core sample size using representative elementary volume concepts. *Water Resources Research*, *36*(5), 1199–1207. https://doi.org/10.1029/2000wr900017

Bruns, S., Stipp, S., & Sørensen, H. (2017, September). Statistical representative elementary volumes of porous media determined using greyscale analysis of 3D tomograms. *Advances in Water Resources*, *107*, 32–42. https://doi.org/10.1016/j.advwatres.2017.06.002

Bultreys, T., Singh, K., Raeini, A. Q., Ruspini, L. C., Øren, P., Berg, S., Rücker, M., Bijeljic, B., & Blunt, M. J. (2020, June). Verifying Pore Network Models of Imbibition in Rocks Using Time-Resolved Synchrotron Imaging. *Water Resources Research*, *56*(6). https://doi.org/10.1029/2019wr026587

Cormen, T. H., Leiserson, C. E., & Rivest, R. L. (1990). *Introduction to algorithms*. MIT Press; McGraw-Hill.

Corbett, P., & Jensen, J. L. (1992). Estimating the mean permeability: How many measurements do you need? *First Break, 10*(3), 89–94. https://doi.org/10.3997/1365-2397.1992006

Costanza-Robinson, M. S., Estabrook, B. D., & Fouhey, D. F. (2011, July). Representative elementary volume estimation for porosity, moisture saturation, and air-water interfacial areas in unsaturated porous media: Data quality implications. *Water Resources Research*, *47*(7). https://doi.org/10.1029/2010wr009655

Dijkstra, E. W**.** (1959). A note on two problems in connexion with graphs. *Numerische Mathematik*, *1*(1), 269-271. https://doi.org/10.1145/3544585.3544600

Ewing, R. P., Hu, Q., & Liu, C. (2010, June). Scale dependence of intragranular porosity, tortuosity, and diffusivity. *Water Resources Research*, *46*(6). https://doi.org/10.1029/2009wr008183

Ferrand, L. A., & Celia, M. A. (1992, March). The effect of heterogeneity on the drainage capillary pressure-saturation relation. *Water Resources Research*, *28*(3), 859–870. https://doi.org/10.1029/91wr02679

Gerke, K. M., Karsanina, M. V., & Katsman, R. (2019, November 20). Calculation of tensorial flow properties on pore level: Exploring the influence of boundary conditions on the permeability of three-dimensional stochastic reconstructions. *Physical Review E*, *100*(5). https://doi.org/10.1103/physreve.100.053312

Gerke, K. M., & Karsanina, M. V. (2020, October 14). How pore structure non-stationarity compromises flow properties representativity (REV) for soil samples: Pore-scale modelling and stationarity analysis. *European Journal of Soil Science*, *72*(2), 527–545. https://doi.org/10.1111/ejss.13055

Ghanbarian, B., Hunt, A. G., Ewing, R. P., & Sahimi, M. (2013, September). Tortuosity in Porous Media: A Critical Review. *Soil Science Society of America Journal*, *77*(5), 1461–1477. https://doi.org/10.2136/sssaj2012.0435

Ghanbarian, B., Torres-Verdín, C., & Skaggs, T. H. (2016, June). Quantifying tight-gas sandstone permeability via critical path analysis. *Advances in Water Resources*, *92*, 316–322. https://doi.org/10.1016/j.advwatres.2016.04.015

Gitman, I., Askes, H., & Sluys, L. (2007, November). Representative volume: Existence and size determination. *Engineering Fracture Mechanics*, *74*(16), 2518–2534. https://doi.org/10.1016/j.engfracmech.2006.12.021

Gostick J, Aghighi M, Hinebaugh J, Tranter T, Hoeh MA, Day H, Spellacy B, Sharqawy MH, Bazylak A, Burns A, Lehnert W. **OpenPNM: a pore network modeling package**. *Computing in Science & Engineering*. 2016 May 25;18(4):60-74. doi:10.1109/MCSE.2016.49.

Hamamoto, S., Moldrup, P., Kawamoto, K., Sakaki, T., Nishimura, T., & Komatsu, T. (2016, August). Pore network structure linked by X-ray CT to particle characteristics and transport parameters. *Soils and Foundations*, *56*(4), 676–690. https://doi.org/10.1016/j.sandf.2016.07.008

Hilfer, R. Review on Scale Dependent Characterization of the Microstructure of Porous Media. Transport in Porous Media 46, 373–390 (2002).

Hilfer, R., & Hauskrecht, J. (2022, August 29). Percolativity of Porous Media. *Transport in Porous Media*, *145*(1), 1–12. https://doi.org/10.1007/s11242-021-01735-7

Hilfer, R., & Lemmer, A. (2015, July 7). Differential porosimetry and permeametry for random porous media. *Physical Review E*, *92*(1). https://doi.org/10.1103/physreve.92.013305

Hommel, J., Coltman, E., & Class, H. (2018, May 25). Porosity–Permeability Relations for Evolving Pore Space: A Review with a Focus on (Bio-)geochemically Altered Porous Media. *Transport in Porous Media*, *124*(2), 589–629. https://doi.org/10.1007/s11242-018-1086-2

Hunt, A. G. (2004, October). Continuum percolation theory and Archie's law. *Geophysical Research Letters*, *31*(19). https://doi.org/10.1029/2004gl020817

Hunt, A., & Ewing, R. (2009, January 1). *Percolation Theory for Flow in Porous Media*. http://books.google.ie/books?id=-C7hzwEACAAJ&dq=Percolation+Theory+for+Porous+Media&hl=&cd=1&source=gbs_api

Ioannidis, M. A., Kwiecien, M. J., & Chatzis, I. (1996). Statistical analysis of the porous microstructure as a method for estimating reservoir permeability. *Journal of Petroleum Science and Engineering, 16*(4), 251–261. https://doi.org/10.1016/S0920-4105(96)00044-7

Jackson, S. J., Lin, Q., & Krevor, S. (2020, May 30). Representative Elementary Volumes, Hysteresis, and Heterogeneity in Multiphase Flow From the Pore to Continuum Scale. *Water Resources Research*, *56*(6). https://doi.org/10.1029/2019wr026396

Jiang, L., Liu, Y., Teng, Y., Zhao, J., Zhang, Y., Yang, M., & Song, Y. (2016, March 18). Permeability estimation of porous media by using an improved capillary bundle model based on micro-CT derived pore geometries. *Heat and Mass Transfer*, *53*(1), 49–58. https://doi.org/10.1007/s00231-016-1795-4

Ju, Y., Gong, W., & Zheng, J. (2022, July). Effects of pore topology on immiscible fluid displacement: Pore-scale lattice Boltzmann modelling and experiments using transparent 3D printed models.

International Journal of Multiphase Flow, *152*, 104085. https://doi.org/10.1016/j.ijmultiphaseflow.2022.104085

Katagiri, J., Saomoto, H., & Utsuno, M. (2015, February). Quantitative Evaluation of the Effect of Grain Aspect Ratio on Permeability. *Vadose Zone Journal*, *14*(2), 1–9. https://doi.org/10.2136/vzj2014.10.0138

Keller, L. M., Holzer, L., Schuetz, P., & Gasser, P. (2013, June). Pore space relevant for gas permeability in Opalinus clay: Statistical analysis of homogeneity, percolation, and representative volume element. *Journal of Geophysical Research: Solid Earth*, *118*(6), 2799–2812. https://doi.org/10.1002/jgrb.50228

Koestel, J., Larsbo, M., & Jarvis, N. (2020, May). Scale and REV analyses for porosity and pore connectivity measures in undisturbed soil. *Geoderma*, *366*, 114206. https://doi.org/10.1016/j.geoderma.2020.114206

Krause, M., Krevor, S., & Benson, S. M. (2013, May 8). A Procedure for the Accurate Determination of Sub-Core Scale Permeability Distributions with Error Quantification. *Transport in Porous Media*, *98*(3), 565–588. https://doi.org/10.1007/s11242-013-0161-y

Kuhlman, K. L., & Matteo, E. N. (2017, November 1). *Porosity and permeability: Literature review and summary*.

Latour, L., Kleinberg, R., Mitra, P., & Sotak, C. (1995, January). Pore-Size Distributions and Tortuosity in Heterogeneous Porous Media. *Journal of Magnetic Resonance, Series A*, *112*(1), 83–91. https://doi.org/10.1006/jmra.1995.1012

Levitz, P. (1999). Off-lattice reconstruction of porous media: Critical evaluation, geometrical confinement, and molecular transport. *Advances in Colloid and Interface Science, 76–77*, 71–106. https://doi.org/10.1016/S0001-8686(98)00042-6

LI, T., LI, M., JING, X., XIAO, W., & CUI, Q. (2019, June). Influence mechanism of pore-scale anisotropy and pore distribution heterogeneity on permeability of porous media. *Petroleum Exploration and Development*, *46*(3), 594–604. https://doi.org/10.1016/s1876-3804(19)60039-x

Liu, J., & Regenauer-Lieb, K. (2011, January 18). Application of percolation theory to microtomography of structured media: Percolation threshold, critical exponents, and upscaling. *Physical Review E*, *83*(1). https://doi.org/10.1103/physreve.83.016106

Lv, P. F., Liu, Y., Liu, F., Yang, W. Z., Liu, H. T., Zhang, B., & Song, Y. C. (2022, August). Pore-based architecture and representative element volume evaluation in artificial sand packs and natural rock cores. *Petroleum Science*, *19*(4), 1473–1482. https://doi.org/10.1016/j.petsci.2022.03.002

Martínez-Mendoza, L. C., Sánchez-Silva, F., Martínez-Mendoza, E. F., & Cruz-Maya, J. A. (2020, December 14). Numerical study of fluid flow at pore scale in packed bed of spheres and grains to obtain the REV. *Comptes Rendus. Mécanique*, *348*(8–9), 769–779. https://doi.org/10.5802/crmeca.62

Mecke, J., & Stoyan, D. (2001, September). The specific connectivity number of random networks. *Advances in Applied Probability*, *33*(03), 576–583. https://doi.org/10.1017/s0001867800011009

Menke, H. P., Bijeljic, B., Andrew, M. G., & Blunt, M. J. (2015, March 23). Dynamic Three-Dimensional Pore-Scale Imaging of Reaction in a Carbonate at Reservoir Conditions. *Environmental Science & Technology*, *49*(7), 4407–4414. https://doi.org/10.1021/es505789f

Mostaghimi, P., Blunt, M., & Bijeljic, B. (2012). Computations of absolute permeability on micro-CT images. *Mathematical Geosciences, 44*(6), 651–666. https://doi.org/10.1007/s11004-012-9431-4

Mu, Y., Sungkorn, R., & Toelke, J. (2016, September). Identifying the representative flow unit for capillary dominated two-phase flow in porous media using morphology-based pore-scale modeling. *Advances in Water Resources*, *95*, 16–28. https://doi.org/10.1016/j.advwatres.2016.02.004

Nelson, P. H. (2009). Pore-throat sizes in sandstones, tight sandstones, and shales. *AAPG Bulletin, 93*(3), 329-340. https://doi.org/10.1306/10240808059

Nordahl, K., & Ringrose, P. (2008). Identifying the representative elementary volume for permeability in heterolithic deposits using numerical rock models. *Mathematical Geosciences, 40*(7), 753–771. https://doi.org/10.1007/s11004-008-9182-4

Okabe, H., & Oseto, K. (2006). Pore-scale heterogeneity assessed by the lattice-Boltzmann method. In *Proceedings of the International Symposium of the Society of Core Analysts* (SCA 2006-44). Trondheim, Norway.

Ozelim, L. C. D. S. M., & Cavalcante, A. L. B. (2018, February). Representative Elementary Volume Determination for Permeability and Porosity Using Numerical Three-Dimensional Experiments in Microtomography Data. *International Journal of Geomechanics*, *18*(2). https://doi.org/10.1061/(asce)gm.1943-5622.0001060

Palombo, M., Gabrielli, A., Servedio, V. D. P., Ruocco, G., & Capuani, S. (2013, September 11). Structural disorder and anomalous diffusion in random packing of spheres. *Scientific Reports*, *3*(1). https://doi.org/10.1038/srep02631

Pereira Nunes, J. P., Blunt, M. J., & Bijeljic, B. (2016, February). Pore-scale simulation of carbonate dissolution in micro-CT images. *Journal of Geophysical Research: Solid Earth*, *121*(2), 558–576. https://doi.org/10.1002/2015jb012117

Piovesan, A., Achille, C., Ameloot, R., Nicolai, B., & Verboven, P. (2019, March 7). Pore network model for permeability characterization of three-dimensionally-printed porous materials for passive microfluidics. *Physical Review E*, *99*(3). https://doi.org/10.1103/physreve.99.033107

Pringle, D. J., Miner, J. E., Eicken, H., & Golden, K. M. (2009, December). Pore space percolation in sea ice single crystals. *Journal of Geophysical Research: Oceans*, *114*(C12). https://doi.org/10.1029/2008jc005145

Provis, J. L., Myers, R. J., White, C. E., Rose, V., & van Deventer, J. S. (2012, June). X-ray microtomography shows pore structure and tortuosity in alkali-activated binders. *Cement and Concrete Research*, *42*(6), 855–864. https://doi.org/10.1016/j.cemconres.2012.03.004

Rahman, T., Ramandi, H. L., Roshan, H., & Iglauer, S. (2020, September 1). Representative Elementary Volume of Rock Using X-Ray Microcomputed Tomography: A New Statistical Approach. *Geofluids*, *2020*, 1–13. https://doi.org/10.1155/2020/8866486

Renard, P., & Allard, D. (2013, January). Connectivity metrics for subsurface flow and transport. *Advances in Water Resources*, *51*, 168–196. https://doi.org/10.1016/j.advwatres.2011.12.001

Rezaei Niya, S. M., & Selvadurai, A. P. S. (2017, March 1). The estimation of permeability of a porous medium with a generalized pore structure by geometry identification. *Physics of Fluids*, *29*(3). https://doi.org/10.1063/1.4977444

Rozenbaum, O. (2011, April). 3-D characterization of weathered building limestones by high resolution synchrotron X-ray microtomography. *Science of the Total Environment*, *409*(10), 1959–1966. https://doi.org/10.1016/j.scitotenv.2011.02.014

Rozenbaum, O., & du Roscoat, S. R. (2014, May 13). Representative elementary volume assessment of three-dimensional x-ray microtomography images of heterogeneous materials: Application to limestones. *Physical Review E*, *89*(5). https://doi.org/10.1103/physreve.89.053304

Rubinstein, J., & Torquato, S. (1989, September). Flow in random porous media: mathematical formulation, variational principles, and rigorous bounds. *Journal of Fluid Mechanics*, *206*, 25–46. https://doi.org/10.1017/s0022112089002211

Singh, A., Regenauer-Lieb, K., Walsh, S. D. C., Armstrong, R. T., van Griethuysen, J. J. M., & Mostaghimi, P. (2020, August 7). On Representative Elementary Volumes of Grayscale Micro-CT Images of Porous Media. *Geophysical Research Letters*, *47*(15). https://doi.org/10.1029/2020gl088594

Skaggs, T. H. (2011, October). Assessment of critical path analyses of the relationship between permeability and electrical conductivity of pore networks. *Advances in Water Resources*, *34*(10), 1335–1342. https://doi.org/10.1016/j.advwatres.2011.06.010

Torquato, S. (2005, October 25). *Random Heterogeneous Materials*. Springer Science & Business Media. http://books.google.ie/books?id=PhG_X4-8DPAC&printsec=frontcover&dq=Random+Hetero+Materials:+Microstructure+and+Macroscopic+Properties&hl=&cd=1&source=gbs_api

Vanson, J. M., Boutin, A., Klotz, M., & Coudert, F. X. (2017). Transport and adsorption under liquid flow: the role of pore geometry. *Soft Matter*, *13*(4), 875–885. https://doi.org/10.1039/c6sm02414a

Vogel, H. (2019, January). Scale Issues in Soil Hydrology. *Vadose Zone Journal*, *18*(1), 1–10. https://doi.org/10.2136/vzj2019.01.0001

Wang, D. Y., Xu, H. S., & Ma, X. J. (2013, December). Computed Tomography Analysis of Representative Elementary Volume (REV) of Porous Medium. *Advanced Materials Research*, *868*, 234–237. https://doi.org/10.4028/www.scientific.net/amr.868.234

Wu, M., Wu, J., Wu, J., & Hu, B. X. (2020, December 15). A new criterion for determining the representative elementary volume of translucent porous media and inner contaminant. *Hydrology and Earth System Sciences*, *24*(12), 5903–5917. https://doi.org/10.5194/hess-24-5903-2020

Wu, M., Wu, J., Wu, J., & Hu, B. X. (2018). A three-dimensional model for quantification of the representative elementary volume of tortuosity in granular porous media. *Journal of Hydrology, 555*, 35–48. https://doi.org/10.1016/j.jhydrol.2017.12.030

XIA, Y., CAI, J., WEI, W., HU, X., WANG, X., & GE, X. (2018, February). A NEW METHOD FOR CALCULATING FRACTAL DIMENSIONS OF POROUS MEDIA BASED ON PORE SIZE DISTRIBUTION. *Fractals*, *26*(01), 1850006. https://doi.org/10.1142/s0218348x18500068

Xiong, Y. (2015). *Development of a compositional model fully coupled with geomechanics and its application to tight oil reservoir simulation* (Doctoral dissertation). Colorado School of Mines.

Xiong, Y., Dong, L., Long, X., Chen, M., & Huang, G. (2021, November 11). Pore-network model to quantify internal structure and hydraulic characteristics of randomly packed grains with different morphologies. *Granular Matter*, *24*(1). https://doi.org/10.1007/s10035-021-01174-7

Xu, K., Wei, W., Chen, Y., Tian, H., Xu, S., & Cai, J. (2022, January 3). A Pore Network Approach to Study Throat Size Effect on the Permeability of Reconstructed Porous Media. *Water*, *14*(1), 77. https://doi.org/10.3390/w14010077

Yu, B., & Liu, W. (2004, January). Fractal analysis of permeabilities for porous media. *AIChE Journal*, *50*(1), 46–57. https://doi.org/10.1002/aic.10004

Zhang, H., Ait Abderrahmane, H., Arif, M., Al Kobaisi, M., & Sassi, M. (2022, February 25). Influence of Heterogeneity on Carbonate Permeability Upscaling: A Renormalization Approach Coupled with the Pore Network Model. *Energy & Fuels*, *36*(6), 3003–3015. https://doi.org/10.1021/acs.energyfuels.1c04010

List of Figures

List of Tables